

Static and Ultrafast Optical Properties of Nanolayered Composites.

Gold Nanoparticles Embedded in Polyelectrolytes

DISSERTATION

Zur Erlangung des akademischen Grades

“doctor rerum naturalium”

(Dr. rer. nat.)

in der Wissenschaftsdisziplin: “Experimentalphysik”

eingereicht an der

Mathematisch-Naturwissenschaftlichen Fakultät

der Universität Potsdam

von

Mareike Kiel

geboren am 29.03.1980 in Oldenburg (Oldb.)

Gutachter:

1. Prof. Dr. Matias Bargheer
2. Prof. Dr. Andreas Fery
3. Prof. Dr. Natalia Del Fatti

eingereicht am: 02. Mai 2012

Tag der mündlichen Prüfung: 16. August 2012

Published online at the
Institutional Repository of the University of Potsdam:
URL <http://opus.kobv.de/ubp/volltexte/2012/6182/>
URN [urn:nbn:de:kobv:517-opus-61823](http://nbn-resolving.org/urn:nbn:de:kobv:517-opus-61823)
<http://nbn-resolving.de/urn:nbn:de:kobv:517-opus-61823>

Betreuer:

1. Prof. Dr. Matias Bargheer
2. Prof. Dr. Helmuth Möhwald

Abstract

In the course of this thesis gold nanoparticle/polyelectrolyte multilayer structures were prepared, characterized, and investigated according to their static and ultrafast optical properties. Using the dip-coating or spin-coating layer-by-layer deposition method, gold-nanoparticle layers were embedded in a polyelectrolyte environment with high structural perfection. Typical structures exhibit four repetition units, each consisting of one gold-particle layer and ten double layers of polyelectrolyte (cationic+anionic polyelectrolyte).

The structures were characterized by X-ray reflectivity measurements, which reveal Bragg peaks up to the seventh order, evidencing the high stratification of the particle layers. In the same measurements pronounced Kiessig fringes were observed, which indicate a low global roughness of the samples. Atomic force microscopy (AFM) images verified this low roughness, which results from the high smoothing capabilities of polyelectrolyte layers. This smoothing effect facilitates the fabrication of stratified nanoparticle/polyelectrolyte multilayer structures, which were nicely illustrated in a transmission electron microscopy image.

The samples' optical properties were investigated by static spectroscopic measurements in the visible and UV range. The measurements revealed a frequency shift of the reflectance and of the plasmon absorption band, depending on the thickness of the polyelectrolyte layers that cover a nanoparticle layer. When the covering layer becomes thicker than the particle interaction range, the absorption spectrum becomes independent of the polymer thickness. However, the reflectance spectrum continues shifting to lower frequencies (even for large thicknesses). The range of plasmon interaction was determined to be in the order of the particle diameter for 10 nm, 20 nm, and 150 nm particles.

The transient broadband complex dielectric function of a multilayer structure was determined experimentally by ultrafast pump-probe spectroscopy. This was achieved by simultaneous measurements of the changes in the reflectance and transmittance of the excited sample over a broad spectral range. The changes in the real and imaginary parts of the dielectric function were directly deduced from the measured data by using a recursive formalism based on the Fresnel equations. This method can be applied to a broad range of nanoparticle systems where experimental data on the transient dielectric response are rare. This complete experimental approach serves as a test ground for modeling the dielectric function of a nanoparticle compound structure upon laser excitation.

Zusammenfassung

Im Rahmen dieser Arbeit wurden Gold-Nanopartikel/Polyelektrolyt Multischichtstrukturen hergestellt, strukturell charakterisiert und bezüglich ihrer optischen Eigenschaften sowohl statisch als auch zeitaufgelöst analysiert. Die Strukturen wurden mithilfe der Dip-coating oder der Spin-coating Methode hergestellt. Beide Methoden ermöglichen das Einbetten einzelner Partikellagen in eine Polyelektrolytumgebung. Typische Strukturen in dieser Arbeit bestehen aus vier Wiederholeinheiten, wobei jede aus einer Nanopartikelschicht und zehn Polyelektrolyt-Doppellagen (kationisches und anionisches Polyelektrolyt) zusammengesetzt ist.

Die Stratifizierung der Gold-Nanopartikellagen wurde mittels Röntgenreflektometrie-Messungen im Kleinwinkelbereich nachgewiesen, welche Bragg Reflexionen bis zur siebten Ordnung aufzeigen. Das ausgeprägte Kiessig Interferenzmuster dieser Messungen weist zudem auf eine geringe globale Rauheit hin, die durch Oberflächenanalysen mit einem Rasterkraftmikroskop bestätigt werden konnte. Diese geringe Rauheit resultiert aus den glättenden Eigenschaften der Polyelektrolyte, die die Herstellung von Multilagensystemen mit mehreren Partikellagen erst ermöglichen. Die Aufnahme eines Transmissionselektronenmikroskops veranschaulicht eindrucksvoll die Anordnung der Partikel in einzelne Schichten.

Durch photospektroskopische Messungen wurden die optischen Eigenschaften der Strukturen im UV- und sichtbaren Bereich untersucht. Beispielsweise wird eine Verschiebung und Verstärkung der Plasmonenresonanz beobachtet, wenn eine Goldnanopartikellage mit transparenten Polyelektrolyten beschichtet wird. Erst wenn die bedeckende Schicht dicker als die Reichweite der Plasmonen wird, bleibt die Absorption konstant. Die spektrale Reflektivität jedoch ändert sich auch mit jeder weiteren adsorbierten Polyelektrolytschicht. Die Reichweite der Plasmonenresonanz konnte auf diese Art für Partikel der Größe 10 nm, 20 nm und 150 nm bestimmt werden. Die Ergebnisse wurden im Kontext einer Effektiven Mediums Theorie diskutiert.

Die komplexe dielektrische Funktion einer Multilagenstruktur wurde zeitabhängig nach Laserpulsanregung für einen breiten spektralen Bereich bestimmt. Dazu wurden zuerst die Änderungen der Reflektivität und Transmittivität simultan mittels der Pump-Probe (Anrege-Abtast) Spektroskopie gemessen. Anschließend wurden aus diesen Daten, mithilfe eines Formalismus, der auf den Fresnelschen Formeln basiert, die Änderungen im Real- und Imaginärteil der dielektrischen Funktion ermittelt. Diese Methode eignet sich zur Bestimmung der transienten dielektrischen Funktion einer Vielzahl von Nanopartikelsystemen. Der rein experimentelle Ansatz ermöglicht es, effektive Medien Theorien und Simulationen der dielektrischen Funktion nach Laserpulsanregung zu überprüfen.

Contents

Abstract	v
Zusammenfassung	vii
1 Introduction	1
2 Theoretical Background	5
2.1 Complex Dielectric Function	5
2.2 Reflectances and Transmittances	11
2.3 Ultrafast Electron and Phonon Dynamics	14
3 Experimental Methods I: Sample Preparation and Characterization	19
3.1 Polyelectrolyte Multilayers with Embedded Nanoparticles	19
3.2 Materials	22
3.2.1 Polyelectrolytes	22
3.2.2 Gold Nanoparticles	23
3.2.3 Substrates	24
3.3 Sample Preparation	24
3.3.1 Chemical Cleaning	24
3.3.2 Dip Coating	25
3.3.3 Spin Coating	26
3.3.4 Dipping vs. Spinning	27
3.4 Sample Characterization Methods	27
3.4.1 UV-Vis Spectroscopy	28
3.4.2 X-Ray Reflectometry	28
3.4.3 Atomic Force Microscopy	30
3.4.4 Angular-Dependent Reflectance and Transmittance	30
4 Experimental Methods II: Ultrafast Pump-Probe Spectroscopy	33
4.1 Experimental Setup for Pump-Probe Spectroscopy	33
4.1.1 Ti:Sapphire Laser System	33
4.1.2 Noncollinear Optical Parametric Amplifier	34
4.1.3 White-Light Continuum Generation and Frequency Resolved Optical Gating	38
4.1.4 Ultrafast Pump-Probe Spectroscopy	40

5	Highly Stratified Gold-Nanoparticle Layers in Polyelectrolyte Matrices and Their Optical Characteristics	43
5.1	Sample Structure	44
5.1.1	Layering Investigation	44
5.1.2	In-Plane Particle Distribution	49
5.1.3	Surface and Interface Roughness	50
5.2	Optical Characterization by Steady-State Spectroscopy	51
5.2.1	Concentration Dependence of LSPR	52
5.2.2	Peak Position and Integrated Intensity as Functions of the Polyelectrolyte Cover Layer Thickness	54
5.2.3	Two Interacting Particle Layers	58
5.2.4	Anisotropy of Multilayer Films	60
5.2.5	Static Dielectric Function of Multilayer Films	63
6	Time-Resolved Ultrafast Optical Spectroscopy	65
6.1	Transient Reflectance and Transmittance	66
6.2	Transient Dielectric Function	73
6.3	Excited Vibrational Modes in 10 nm and 20 nm Gold Particles	78
6.4	Monitoring the Propagating Strain Pulse in the Substrate	82
7	Summary	87

1 Introduction

Composite materials with incorporated metal nanoparticles have been in the focus of ongoing scientific work for many years. Natural and medical scientists and engineers are equally interested in studying such structures in order to understand fundamental processes which determine the material properties and may lead to future applications. This effort is reflected in the broad spectrum of applications which make use of the unique properties of nanosized objects. Hence, the literature to the subject has been growing extensively such that the articles mentioned in the following represent only a small selection of literature that is available today.

The popularity of hybrid materials with nanoparticles is caused by the size- and shape-dependent properties that originate from the mesoscopic size of the incorporated objects. The most prominent feature of the optical response of such structures is the localized surface plasmon resonance (LSPR), which for gold nanoparticles is located in the visible spectrum. This feature is exploited in a variety of devices such as sensors, amplifiers, coatings, solar cells, etc.[1–3] One significant characteristic of the LSPR is that its exact spectral position can be tuned by changing the size and shape of the nanoparticles or by modifying the environmental conditions. Via this tunable, strong, and narrow absorption band nanoparticles can be selectively excited or heated, which is particularly useful for the treatment of cancer cells [4–6], for drug delivery purposes [7] and for medical imaging techniques [4, 8, 9]. The field enhancement effect of the electromagnetic field near nanoparticles is frequently utilized for the detection of molecular Raman signals and for enhancing or quenching fluorescences.[10–12]

Due to their mesoscopic size, nanosized objects are characterized by a large surface to volume ratio, which is especially useful, for example, for catalytic purposes [2, 13, 14] or in water purification processes [15, 16], as the reactivity of the particles is linked to the available surface area. Biological applications benefit from the large surface as well, as they bear the possibility of linking particles with molecules or labeling them with biomolecular systems. In combination with noble-metal nanoparticles, this is particularly interesting for applications in the human body due to the high biocompatibility of gold and silver with human tissue. The small size of nanoparticles facilitates their incorporation into any small organic tissue.

This thesis was developed within the scope of a cooperation of the *Max Planck Institute of Colloids and Interfaces* and the *Ultrafast Dynamics in Condensed Matter* group at the *University of Potsdam*. The motivation of this interdisciplinary work is to combine the expertise knowledge of the groups on polyelectrolyte/nanoparticle

compound matter and ultrafast investigation methods, respectively, in order to study processes in the nanocomposites that happen on the femto- to nanosecond time scale. The idea is to gain information on the structural and electronic changes upon laser irradiation by ultrafast X-ray diffraction (XRD) and optical pump-probe spectroscopy. While XRD allows for directly measuring structural changes, optical pump-probe spectroscopy gives an insight into the electronic dynamics in a system. Both methods, which work with a time resolution that is defined by the pulse length (typically ~ 100 fs), have rarely been applied to soft matter/nanoparticle hybrid materials. Such experiments can, for example, deliver information on heat transport in nanoparticles and in the environment. The knowledge of heat diffusion plays a major role in drug delivery as it is a crucial factor in controlling the release of treatment agents at a defined place and time.

Monitoring and modeling the ultrafast dielectric response allows one to understand the dynamics of the electronic system upon ultrafast induced heating. A pure experimental approach for measuring the time-dependent dielectric function of gold nanoparticles over a broad spectral range is, to this date, not fully achieved.

In this work, a polyelectrolyte matrix material is used to efficiently build multilayer nanoparticle structures with defined layer thicknesses. This is important in order to make them best suitable for XRD investigations. For optical experiments, the existence of several particle layers is advantageous as they considerably increase the reflectance and absorbance, while the particle concentrations within single layers remain low and the clustering of particles is avoided. The preparation of polyelectrolyte multilayers with nanoparticles has been reported several times. However, highly stratified particle layers, necessary for XRD investigations, in polyelectrolyte samples are rare. The optical response to strong and ultrafast laser excitation of metal nanoparticles has typically been studied of particles being embedded in solution or in glass or oxide matrices.[17–19] When this thesis work was started, it was not clear whether these pump-probe experiments can be performed nondestructively in such a soft matter/metal nanoparticle compound system.

This thesis presents the preparation and characterization of multilayer gold nanoparticle/polyelectrolyte composite structures and their subsequent ultrafast pump-probe spectroscopic investigation. Chapter 2 gives a short introduction to gold nanoparticles regarding the origin of their optical and dielectric properties. The principles of effective medium theories are explained on the basis of the Maxwell Garnett mixing theory. The chapter closes with a review of the state of the scientific knowledge on the ultrafast dynamics in nanoparticle systems upon ultrafast laser heating.

Chapter 3 covers the experimental methods on the preparation and characterization of gold nanoparticle/polyelectrolyte compound structures. The preparation of nanoparticle layers by using the layer-by-layer deposition techniques is described and a presentation of the applied characterization techniques is given, which include X-ray reflectivity, atomic force microscopy, transmission electron microscopy, UV-Vis spectroscopy, and angular-dependent reflectance and transmittance measurements.

Chapter 4 presents the experimental methods for ultrafast pump-probe spectroscopy. A description of the optical setup and the noncollinear optical parametric amplifier (NOPA) is presented which includes the characterization of the used laser pulses. Chapter 5 covers the structural analysis of gold-nanoparticle multilayer samples. Furthermore, the coupling of particles within one layering plane and the interaction of two particle planes is determined by static optical experiments. A multilayer sample is thoroughly characterized according to a possible birefringence, the static dielectric function, and the volume fraction of gold particles inside the sample. In chapter 6 the ultrafast pump-probe spectroscopy results are presented and discussed. These results comprise the time-dependent monitoring of the effective dielectric function after laser pulse excitation and the reflectivity measurements of the vibrational mode of nanoparticles with sizes of 10 nm and 20 nm.

Several books were particularly helpful in acquiring knowledge and skills to prepare and statically characterize stratified multilayer nanoparticle films. First, the book “Multilayer Thin Films” by G. Decher and J. B. Schlenoff provides information on the preparation and the physical processes during the polyelectrolyte buildup.[20] U. Kreibig and M. Vollmer in their textbook “Optical Properties of Metal Clusters” give a comprehensive overview on the fundamental physical properties of such systems.[21] The ultrafast properties of nanoparticle systems are treated in many articles and review papers. A recently published review by G. V. Hartland “Optical Studies of Dynamics in Noble Metal Nanostructures” (2011) gives a comprehensive summary of the processes in the particles and surrounding medium.[22]

2 Theoretical Background

This chapter presents optical properties of nanoparticle compound structures which are relevant to this thesis. It is shown how the resonant electronic polarization of nanosized objects embedded in a transparent dielectric medium affects the compound dielectric function. A harmonic oscillator model is used to describe this resonance and derive the according real and imaginary part of the dielectric function. The contribution of electronic intraband and interband transitions are described for bulk gold and then translated to the nanoparticle system. The Maxwell-Garnett effective medium theory is introduced, which simulates the effective dielectric function from the constituents' dielectric constants. Subsequently, a formalism is presented which models the reflectance and transmittance of thin anisotropic multilayer structures. The last section summarizes the results of the ultrafast measurements of electron and lattice dynamics in nanoparticle systems.

2.1 Complex Dielectric Function

A material's dielectric function ϵ describes the polarization and dissipation of electromagnetic waves in that material. Analyzing the material's electronic system allows one to determine this dielectric function and thus predict the frequency-dependent absorbances and reflectances. The dielectric function can be calculated from the susceptibility χ of the material using $\epsilon = 1 + \chi$, where χ is related to the polarization density \mathbf{P} by $\mathbf{P}(\omega) = \epsilon_0 \chi \mathbf{E}(\omega)$.

The following formalism shows how this electronic polarization density can be derived by using a linear oscillator model which describes the motion of electrons that are driven by an oscillating external electric field \mathbf{E} . This model explains the origin of the complex refractive index and the complex dielectric function. It is often applied to approximate the dielectric function for systems in which the exact absorption mechanism is unknown, because it well simulates a resonance with an eigenfrequency ω_0 and it accounts for the damping of the electrons and a possible bonding of the electrons to the atom.

The following description of the dielectric function was essentially deduced from the textbooks “Optical Properties of Nanoparticle Systems: Mie and Beyond” by M. Quinten[23], “Photonik” by G.A. Reider[24], and “Optical Properties of Metal Clusters” by U. Kreibig and M. Vollmer[21].

The general procedure to derive the polarization density and hence the dielectric function starts by calculating the displacement of electrons under the external elec-

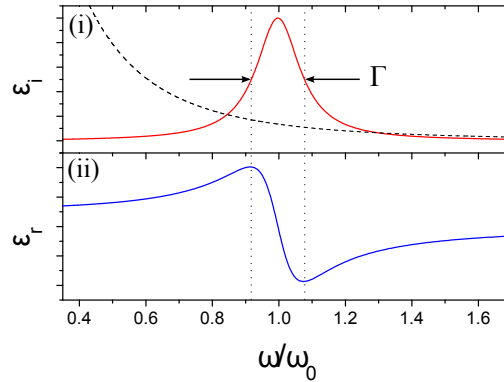


Figure 2.1: Calculations of the imaginary (i) and real (ii) parts of the dielectric function according to the harmonic oscillator model.

tric field E_0 . The according equation of motion reads as follows:

$$m_e \frac{\delta^2 \mathbf{x}}{\delta t^2} + m_e \Gamma \frac{\delta \mathbf{x}}{\delta t} + a \mathbf{x} = e \mathbf{E} e^{-i\omega t} \quad (2.1)$$

with the electronic mass m_e and the scattering rate Γ . The linear force term $a \cdot \mathbf{x}$ describes the electrostatic restoring forces, where \mathbf{x} is the displacement and a is the linear force constant. This term gives rise to an eigenfrequency ω_0 at which the system is resonantly excited and which is directly proportional to a as follows: $a = m_e \omega_0^2$. Solving equation 2.1 yields the following amplitude of the conduction electrons:

$$\mathbf{x}(\omega) = \frac{-e/m_e}{\omega^2 - i\omega\Gamma} \mathbf{E}(\omega). \quad (2.2)$$

Via the fundamental expressions for the induced dipole moment $\mathbf{p}(\omega) = -e\mathbf{x}(\omega)$, the total polarization density $\mathbf{P}(\omega) = n_e \mathbf{p}(\omega)$ can be determined to be

$$\mathbf{P}(\omega) = n_e \frac{e^2/m_e}{\omega^2 - i\omega\Gamma} \mathbf{E}(\omega). \quad (2.3)$$

The dielectric function which results from this induced polarization density can now be determined from the relation $\mathbf{P} = \epsilon_0(\epsilon - 1)\mathbf{E}(\omega)$:

$$\epsilon_r = 1 + \omega_p^2 \frac{(\omega_0^2 - \omega^2)}{(\omega_0^2 - \omega^2)^2 + \omega^2 \Gamma^2} \quad \text{and} \quad \epsilon_i = -\omega_p^2 \frac{\omega \Gamma}{(\omega_0^2 - \omega^2)^2 + \omega^2 \Gamma^2}, \quad (2.4)$$

where $\omega_p^2 = n_e e^2 / \epsilon_0 m_e$ is the material plasma frequency. These equations are plotted in figure 2.1. The imaginary part ϵ_i exhibits the shape of a Lorentz distribution function with the maximum position being located at ω_0 .

In a system where more than one absorption mechanism is active, the total sus-

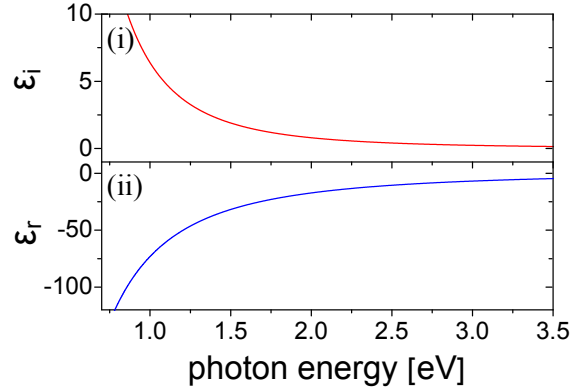


Figure 2.2: Drude contribution to the dielectric function in bulk gold. (i) shows the imaginary and (ii) the real part of the dielectric function.

ceptibility is given by a summation of all individual contributions. In bulk noble metals, these comprise the intraband absorption and contributions from interband excitations, resulting in $\epsilon = 1 + \chi_{IB} + \chi_{DS}$.

In the next two sections, the intraband and interband contributions to the dielectric function of bulk gold are described in detail. The subsequent section presents an effective medium model for the simulation of the dielectric function of gold-nanoparticle structures.

Intraband Dielectric Contribution in Bulk Gold The intraband susceptibility describes the excitation of free electrons within the conduction band. Unlike in equation 2.1, the electrons in a bulk system do not feel Coulomb restoring forces because the system is invariant upon translational motion of the electrons. Consequently, the eigenfrequency is zero ($a = m_e \omega_0 = 0$) and the dielectric function, which exhibits a resonance at $\omega = 0$, is given by

$$\epsilon_r = 1 - \omega_p^2 \frac{1}{(\omega^2 + \Gamma^2)} \quad \text{and} \quad \epsilon_i = -\omega_p^2 \frac{\Gamma}{\omega(\omega^2 + \Gamma^2)}. \quad (2.5)$$

These equations present the Drude contribution to the bulk metal dielectric function and are plotted in figure 2.2. The influence of the ionic lattice on the conduction electrons can be accounted for by using the effective electronic mass m_{eff} instead of m_e . The Drude absorption in bulk gold is characterized by the strong absorption for low ω (infrared) as the imaginary part is reciprocal proportional to ω : $\text{Im}(\epsilon) \propto \frac{1}{\omega}$. At $\omega = 0$, the real and imaginary parts diverge.

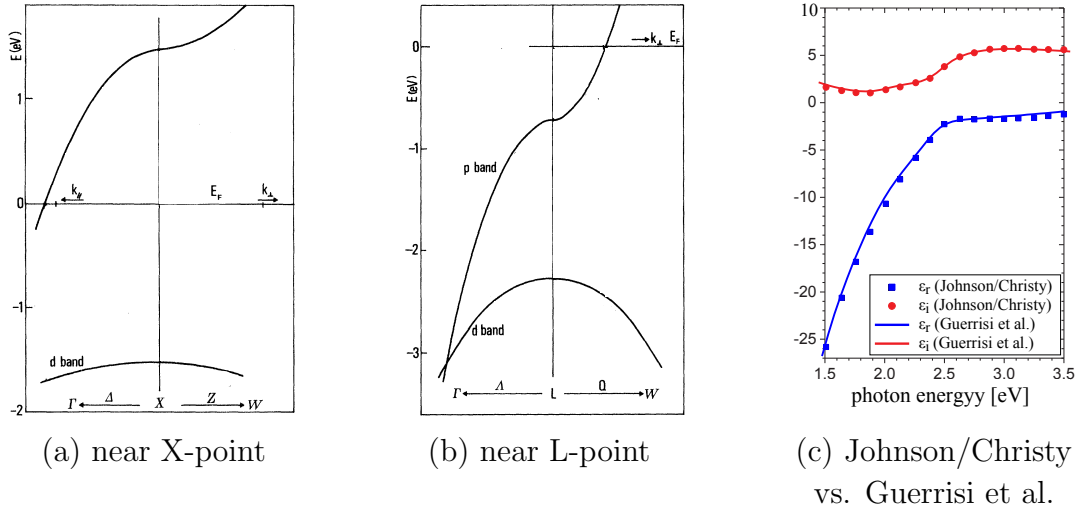


Figure 2.3: (a) and (b) present the results of band structure calculations of bulk gold by M. Guerrisi et al. at two different points of the Brillouin zone (Modified after reference [25]). (c) The solid lines depict the theoretical dielectric function of gold according to the band structure calculations of M. Guerrisi et al. The symbols correspond to experimental values measured by P. B. Johnson and R. W. Christy in 1972.[26]

Interband Contribution The interband excitations in bulk gold describe the transition of electrons from the filled and low-lying d-bands to the partly filled sp-band in the UV spectral range. For systems in which the band structure is not precisely known, the interband contribution is typically approximated by simulating a sequence of resonances, each being described by the dielectric function of the harmonic oscillator given by equation 2.4.[27] In gold, however, where the band structure has been precisely determined, the interband contribution to the dielectric function is typically calculated by determining the joint density of states, which gives the density of pairs of states for the d- and sp-band, which are connected by an optical transition.

Figure 2.3 (a) and (b) shows band structure calculations from Guerrisi et al. at the L and X symmetry points of the Brillouin zone for one particular temperature.[25] The resulting dielectric function is calculated at 600 K and plotted in figure 2.3 (c) along with the experimentally derived values of the dielectric function measured by P. B. Johnson and R. W. Christy in 1972 for a gold film.[26] For photon energies above the threshold energy $E_{IB} = 2.2$ eV, the contribution to the dielectric function is due to interband transitions at these two symmetry points.[26] The pronounced contribution below 2 eV results from Drude intraband absorption processes in bulk gold.

The sketch given in figure 2.4 (a) presents a simplification of the gold band structure, which is frequently used in the literature. The d-bands are approximated to be rather flat, while the sp-band is assumed to exhibit a nearly parabolic shape as in free electron metals. The overlap of the two bands indicates their strong corre-

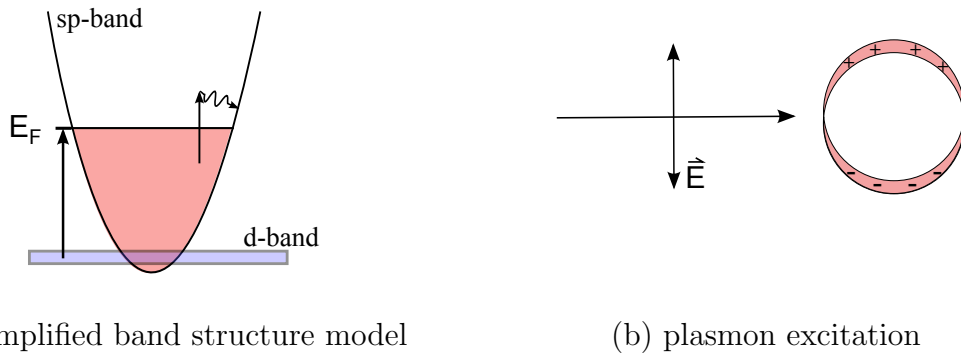


Figure 2.4: (a) Simplified presentation of the band structure in gold. The flat d-bands overlap with the sp-conduction band. The vectors indicate interband (left) and intraband (right) transitions. (b) Cartoon of the nanoparticle electronic polarization induced by an electromagnetic wave.

lation, which causes the material response to be independent of the exact nature of the excitation mechanism (interband or intraband excitation).

Dielectric Function of Gold Nanoparticles and Effective Medium Theories

In metal nanoparticles, the harmonic oscillator given by equation 2.1 well describes the motion of the conduction electrons upon electromagnetic irradiation. Contrary to the free electrons in bulk metals, these electrons are exposed to restoring coulomb forces from the lattice ions during displacement, which are accounted for by the linear force term $\mathbf{a} \cdot x$. Consequently, this system exhibits an eigenfrequency ω_0 at which the electrons perform a collective oscillatory motion with respect to the fixed ion cores and which results in the appearance of the resonance absorption. All oscillator strength is then stored within this narrow spectral part of the resonance, while in the near infrared, the material becomes transparent. This is called the LSPR and is represented by the Lorentz oscillator given in figure 2.1.

If the wavelength of irradiation is much greater than the nanoparticle radius, i.e., $\lambda \gg R$, the plasmons are quasi-static and therefore dipolar. In that case, the electric field is constant across the particle due to the small particle size and varies with time only. Multipole excitations are suppressed and phase retardation effects can be neglected. In this thesis, only dipolar plasmons are regarded.

The contribution of the conduction electrons to the dielectric function of the nanoparticles is described by equation 2.4, which was derived from the harmonic oscillator model. This method neglects the influence of the dielectric environment, although a realistic nanoparticle system can only be described by considering the nanoparticles and the dielectric properties of their surrounding even if they are located in vacuum. Several effective medium theories have been developed, which approximate the response of nanosized metal objects embedded in a dielectric medium to electromagnetic radiation by treating the structure as a homogeneous sample layer with

an effective dielectric function ϵ_{eff} . The assumption of an effective medium is valid for compound systems in which the nanosized objects are much smaller than the wavelength of the investigating radiation.

J.C.M. Garnett derived an equation for spherical metal nanoparticles which are statistically distributed in a transparent dielectric medium with the dielectric function ϵ_m : [28]

$$\epsilon^{eff} = \epsilon_m + 3f \cdot \epsilon_m \frac{\epsilon_{particles} - \epsilon_m}{\epsilon_{particles} + 2\epsilon_m}. \quad (2.6)$$

The effective dielectric function ϵ^{eff} is a function of the constituents' dielectric constants and of the volume filling factor f . This parameter describes the amount of nanoparticle material in the compound structure and is defined as the ratio of particle volume to the overall sample volume:

$$f = \frac{V_{particles}}{V_{particles+medium}}. \quad (2.7)$$

This Maxwell-Garnett formula is equivalent to the well-known Clausius-Mossotti formula for molecular structures. It is strictly valid for small filling factors f ($f < 10^{-2}$) but was experimentally proven to be correct for higher values of f . [29, 30] Although this formula does not explicitly account for the size of the nanoparticles, the particles must conform to the restrictions of the quasi-static regime. Moreover, this formula is only valid for spherical particles, for which ω_0 is related to the plasma frequency ω_p as follows: [21]

$$\text{in vacuum: } \omega_0 = \frac{\omega_p}{\sqrt{3}}, \quad \text{and in medium: } \omega_0 = \frac{\omega_p}{\sqrt{1 + 2\epsilon_m}}. \quad (2.8)$$

In reference [21], U. Kreibig and M. Vollmer tabularly summarize the position of the resonance as a function of ω_p for differently shaped objects.

By means of the Maxwell-Garnett formula given in equation 2.6, it is possible to predict the spectral position of the surface plasmon resonance. It exists for wavelengths (frequencies) at which the denominator ($\epsilon_{particles} + 2\epsilon_m$) becomes zero. Since the dielectric constant of the embedding medium is real, the resonance condition can be modified to $Re(\epsilon_{particles}) = -2Re(\epsilon_m)$.

The resonance intensity is then determined by the imaginary part $Im(\epsilon_{particles})$ of the particles' dielectric function. The smaller the extinction parameter at the resonance wavelength, the smaller is the denominator value and more pronounced is the resonance.

The linewidth of the resonance [full width at half maximum (FWHM)] is equal to the phenomenological constant Γ as indicated in panel (i) of figure 2.1. In the free electron approximation, Γ has the physical meaning of a scattering rate and is equal to the reciprocal relaxation time of the electrons: $\Gamma = 2\pi/\tau$. The relaxation of the

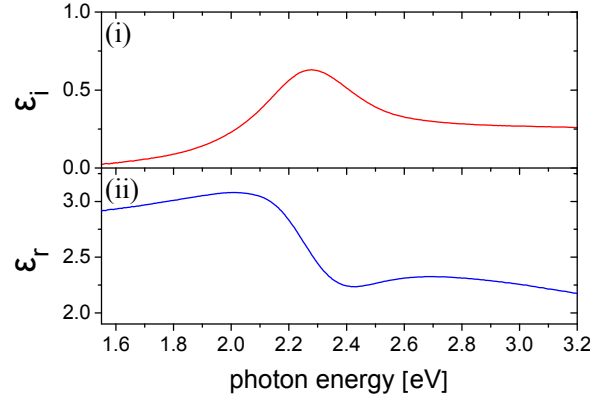


Figure 2.5: Example of the imaginary (i) and real (ii) parts of the effective dielectric function of an arbitrary polyelectrolyte/nanoparticle compound structure.

electrons is based on the scattering processes of the electrons with other electrons (e–e), phonons (e–ph), surfaces (e–sf), and impurities (e–imp), or it results from radiative relaxations. Γ is then given by $\Gamma = \frac{2\pi}{\tau_{tot}} = 2\pi\left(\frac{1}{\tau_{e-e}} + \frac{1}{\tau_{e-ph}} + \frac{1}{\tau_{e-sf}} \dots\right)$ Figure 2.5 shows a typical spectrum of a compound structure with embedded spherical gold nanoparticles with a diameter of 10 nm. The imaginary dielectric function of gold nanoparticle samples is typically characterized by an asymmetric resonance shape, which results from the overlap of the LSPR with the interband contribution to the gold dielectric function.

The real $Re(\epsilon^{eff})$ and imaginary parts $Im(\epsilon^{eff})$ of the dielectric function, as plotted in figure 2.5, are related to each other by the Kramers-Kronig relations. Generally, these relations connect two frequency-dependent functions in a linear way, for example, $Im(\epsilon)$ and $Re(\epsilon)$, $R(\omega)$ and $T(\omega)$, or $n(\omega)$ and $\kappa(\omega)$, independent of the exact absorption processes that take place. Consequently, if one of these functions is experimentally determined, the Kramers-Kronig relations facilitate deriving the second function. Since these relations comprise a frequency integral ranging from zero to infinity, the spectra, which are measured in a finite range only, must be extrapolated. However, this procedure bears errors since during extrapolation, possible contributions of resonances in the UV-range are neglected, which may contribute considerably.

2.2 Reflectances and Transmittances

The reflectance R and transmittance T of a bulk material surface are described by the well-known Fresnel formulas:[24]

$$R = |\rho|^2 \quad \text{with} \quad \rho = \frac{n_{air}\cos(\alpha) - n_{bulk}\cos(\beta)}{n_{air}\cos(\alpha) + n_{bulk}\cos(\beta)} \quad (2.9)$$

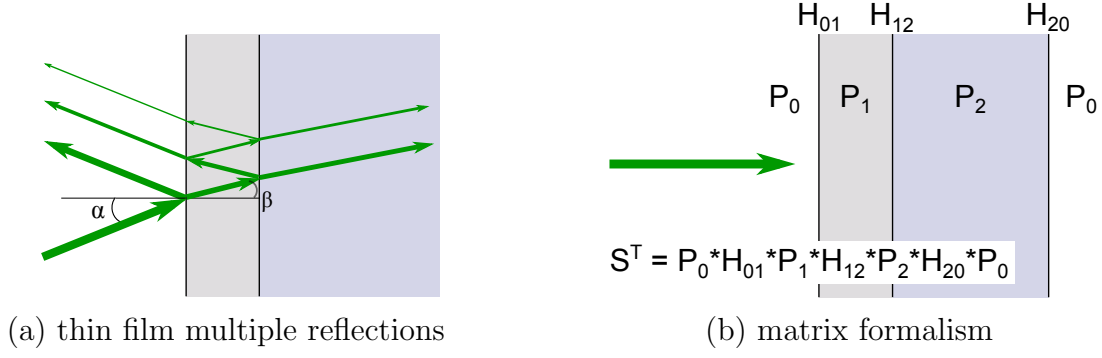


Figure 2.6: (a) Beam propagation in a thin layer sample. (b) The matrix formalism applied to a thin layer sample on a substrate. The system matrix S describes the complete structure and allows for calculating the according reflectance and transmittance (see equations 2.18 and 2.19).

$$T = \frac{n_{bulk} \cos(\beta)}{n_{air} \cos(\alpha)} |\tau|^2 \quad \text{with} \quad \tau = \frac{2n_{air} \cos(\alpha)}{n_{air} \cos(\alpha) - n_{bulk} \cos(\beta)}. \quad (2.10)$$

Equations 2.9 and 2.10 apply to s-polarized light, where α is the angle of the incident wave with the surface normal [see figure 2.6 (a)]. β describes the angle of the refracted beam inside the structure with the surface normal and is connected to α by Snell's law.[24] ρ and τ are called the amplitude reflection coefficient and amplitude transmittance coefficient, respectively.

In order to determine the reflectance and transmittance of a thin film structure, one has to take into account multiple reflections inside the thin film [Figure 2.6 (a)], which may modify the intensity of the reflected and transmitted light by constructive or destructive interference. Especially, if the interface roughnesses are much smaller than the wavelength of the investigating light, significant changes in the reflected and transmitted intensities may occur.

The reflection coefficient of such structures is then determined by adding the contribution from the surface reflection to the reflected contribution from the rear interface and taking into account the phase difference $\Delta\phi$ of these two waves. Accordingly, all other multiple reflected beams must be added, as shown in equation 2.11. The transmittance is calculated likewise (eq. 2.12).

$$\rho_{total} = \rho_{01} + (\tau_{01}\tau_{10})\rho_{12}e^{2i\phi D_1} + (\tau_{01}\tau_{10})\rho_{10}(\rho_{21})^2e^{4i\phi D_1} + (\tau_{01}\tau_{10})\dots \quad (2.11)$$

$$\tau_{total} = (\tau_{01}\tau_{10})e^{i\phi D_1} + (\tau_{01}\tau_{10})(\rho_{10})^2e^{3i\phi D_1} + (\tau_{01}\tau_{10})(\rho_{10})^2e^{5i\phi D_1} + \dots \quad (2.12)$$

The subscripts 0, 1, and 2 describe the ambient air, the thin film, and the substrate material, respectively. D_1 is the thin film thickness, and ϕ is the phase.

If the sample of investigation exhibits an anisotropic structure, the dielectric properties must be described by a complex dielectric tensor ϵ . In 1987, Oscar E. Piro derived expressions for the transmittance and reflectance of such anisotropic absorbing crystal plates with smooth surfaces.[31] He defined the amplitude reflection and transmission coefficients for the electric fields at a single interface of the crystal plate for s-polarized light:

$$\rho_{12} = \frac{\sqrt{\epsilon_1 - \sin(\alpha)^2} - \sqrt{\epsilon_2 - \sin(\alpha)^2}}{\sqrt{\epsilon_1 - \sin(\alpha)^2} + \sqrt{\epsilon_2 - \sin(\alpha)^2}} \quad (2.13)$$

$$\tau_{12} = \frac{2\sqrt{\epsilon_1 - \sin(\alpha)^2}}{\sqrt{\epsilon_1 - \sin(\alpha)^2} + \sqrt{\epsilon_2 - \sin(\alpha)^2}}, \quad (2.14)$$

where the subscripts describe the media 1 and 2 at the interface. The phase information is given by

$$\phi_1 = \frac{2\pi D_1}{\lambda} \sqrt{\epsilon_1 - \sin(\alpha)^2}, \quad (2.15)$$

where α describes the angle between the incoming beam and the surface normal. Equivalent formulas exist, which apply to perpendicular polarized light.[31]

In order to calculate the final reflection amplitude, again, the contribution from the surface reflection is added to the reflected contribution from the rear interface, which passes the absorbing medium twice. Accordingly, all multiple reflected beams are added likewise. As a consequence, this method accounts for interference effects.

In a multilayer system, however, this procedure becomes too extensive because the beam propagation here is rather complicated. Already a two layer system would require extensive numeric descriptions, which inhibit analytical inversions, if necessary.

Matrix Method for Determining R and T of Multilayer Structures A convenient method for modeling reflectances and transmittances of a multilayer structure is based on a matrix formalism from M. V. Klein and T. E. Furtak.[32] Therein, matrices which describe the electric fields at interfaces (H) and inside transmitting media (P) are derived according to the Fresnel equations. In this thesis, this method is expanded to the formulas derived by Oscar Piro for anisotropic media.[31] The matrices H and P are then given by

$$H_{12} = \frac{1}{\tau_{12}} \begin{pmatrix} 1 & \rho_{12} \\ \rho_{12} & 1 \end{pmatrix} \quad (2.16)$$

and

$$P_1 = \begin{pmatrix} \exp(i\phi_1) & 0 \\ 0 & \exp(-i\phi_1) \end{pmatrix}, \text{ respectively,} \quad (2.17)$$

where ρ , τ , and ϕ are defined as before in equation 2.13–2.15. Thus, H contains the reflection and transmission coefficients at the interfaces and P describes the propagation effects in the layer.

In order to describe a multilayer system, these matrices are then sequentially multiplied in the order in which the light passes through the elements they describe, as illustrated in figure 2.6 (b) for a two-layer structure. The result is a system matrix S from which the amplitude coefficients ρ and τ , which describe the complete structure, can be calculated directly. The final reflectance is given by

$$R = |\rho|^2 = \left(\frac{(S_R)_{12}}{(S_R)_{22}} \right)^2, \quad (2.18)$$

while the transmittance is calculated from the system matrix as:

$$T = |\tau|^2 = \frac{1}{|(S_T)_{22}|^2}. \quad (2.19)$$

This equation describing an intensity is valid for transmittances in a medium which is identical with the incident one. For transmittances in a different medium, $|\tau|^2$ must be multiplied with the correction factor $\frac{n_1 \cos(\beta)}{n_0 \cos(\alpha)}$, which accounts for the change in the beam width due to refraction.

The final matrix S contains all effects from the single matrices as reflection and absorption, and additionally, it accounts for multilayer effects such as multiple reflections within the layers.

2.3 Ultrafast Electron and Phonon Dynamics

This section summarizes the most relevant results of the investigations of the electronic and structural dynamics that follow the absorption of ultrashort laser pulses. Representative publications and review articles are given, which report on these processes in metal nanoparticle systems and which proved to be particularly helpful for understanding the ultrafast processes.

In 2000, for example, J. Hohlfeld summarized the electronic relaxation dynamics in bulk metals after ultrafast excitation.[33] A review article from G. V. Hartland describes the according processes in nano-objects and provides a detailed literature

survey.[22] Other frequently cited reviews on ultrafast dynamics in metallic nanoparticles were published by S. Link[34], F. Vallée and coworkers[35, 36], and G. V. Hartland[37].

The following list describes the physical processes in gold nanoparticles after laser excitation in chronological order:

1. In nanoparticles, the absorption of laser pulse photons with energies close to the plasmon frequency ω_0 results in the excitation of the LSPR. This plasmon subsequently decays by radiative processes or by excitation inside (intraband) or by transition into (interband) the conduction band.[38] In large particles (diameter >100 nm) the most likely relaxation process is due to the emission of photons (radiative effect).[22] In small particles, the plasmon resonance rather relaxes due to the scattering events of the electrons with surfaces, other electrons, phonons, impurities, etc., which result in the loss of phase information (dephasing process). The typical lifetime of the LSPR in gold particles measures a few femtoseconds (~ 5 fs), which conforms to a spectral plasmon width of about 100 nm (FWHM).[39] After the dephasing process, the electronic system is described by a nonthermal electron distribution.

In addition to the plasmon resonance excitation, it is possible to also excite the intraband and interband transitions directly. Especially, for energies above the plasmon resonance (>2.5 eV), which is above the interband transition threshold, it is most likely to excite electrons from the d-bands into the sp-band. However, the processes following laser pulse excitation are independent of the exact excitation mechanism. This invariance is a result of strongly coupled electrons which cause the system to be identical a few femtoseconds after excitation.

The dephasing processes, which occur within a few femtoseconds, are beyond the scope of this thesis. Given the time resolution of the used laser system, processes are studied which take place on time scales longer than 100 fs and which are presented in the following.

2. The nonthermal electron distribution is characterized by a step-like electron occupation distribution at the Fermi energy, as shown in figure 2.7 (b). Via electron-electron interaction, the occupation thermalizes to a hot Fermi distribution [see Figure 2.7 (c)]. In bulk gold, this redistribution process takes place on a time scale of typically 500 fs.[40, 41] Many publications have reported on the simulation of the dielectric function which corresponds to the hot Fermi distribution in metal films and nanoparticle structures after laser excitation.[37, 40, 42, 43] The widely used procedure starts by calculating the smearing at the Fermi edge and then determining the imaginary dielectric function from the band structure model of Guerrisi et al. shown in figure 2.3 (a)–(c). Using the Kramers-Kronig relations then facilitates the derivation of the according real part.[44] The calculations for metal films are supported by

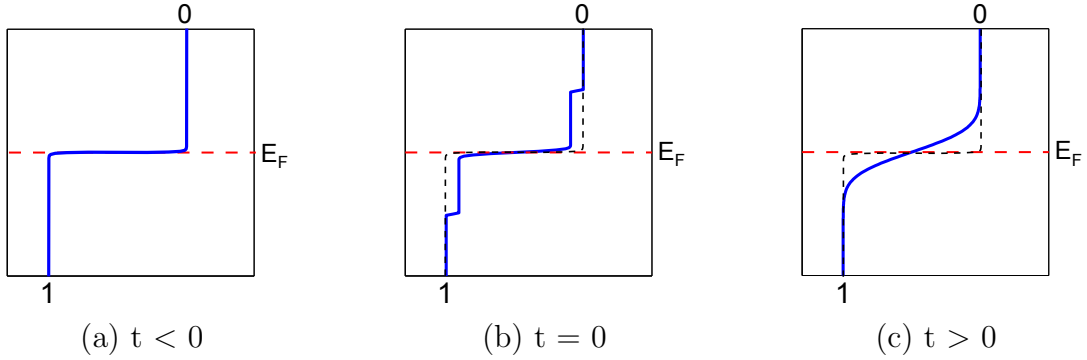


Figure 2.7: (a) Electronic occupation at the Fermi-level before excitation, (b) non-thermalized electron distribution right after excitation, and (c) ~ 500 fs after thermalization to a hot Fermi distribution.

a large body of literature in which the experimentally derived dielectric function confirms with the theoretical results. Especially, ultrafast pump-probe spectroscopy proved to be a powerful tool for investigating such electronic thermalization processes.[19, 36, 41, 45–49] A purely experimental derivation of the broadband dielectric function of a nanoparticle system was not available when this thesis work was started.

3. After the thermalization of the electron distribution to a hot Fermi distribution, about 500 fs after excitation, the electron temperature strongly differs from the lattice temperature. Via electron–phonon coupling, energy is transferred from the hot electrons to the lattice until both systems are in thermal equilibrium. The coupling of these two systems is described by the two-temperature model (TTM), which describes the changes in the according temperatures by $C_e(T_e)\delta T_e/\delta t = -G(T_e - T_L)$ and $C_L(T_L)\delta T_L/\delta t = G(T_e - T_L)$. G is the electron–phonon coupling constant which is linked to the scattering rate of the electrons with the lattice.[50] Because C_e in gold is strongly temperature dependent, the rate at which the system thermalizes depends on the induced temperature. In the low perturbation regime, the electron–phonon coupling constant in gold measures ~ 1 ps and T_e decays exponentially. For strong excitation conditions, the signal decay is nonexponential and the decay time measures several picoseconds.[37, 48–51] Since the lattice heat capacity is significantly larger than the electronic one, ($C_L > C_e$) the rise of the lattice temperature ΔT_L is considerably smaller than that of ΔT_e .
4. According to the displacive excitation mechanism, the rise in the lattice temperature T_L directly results in an expansion of the lattice. The diameter of spherical nanoparticles, therefore, increases to a larger value $D_{hot} = D(1 + \beta \cdot \Delta T)$, where β is the volume expansion coefficient. If the lattice is heated on an ultrashort time scale, the expansion occurs impulsively and triggers a volume oscillation around the expanded particle diameter D_{hot} . In spherical

particles, this volume oscillation, also called breathing mode, is isotropic and has been studied intensively by ultrafast pump-probe spectroscopy. Nanorods exhibit a second vibrational mode, the extensional mode, in which the rods elongate and become thinner.

These vibrational motions are typically investigated by measuring the change in transmittance during a vibrational period at distinct wavelengths in the vicinity of the resonances. From the results, it was concluded that the resonance shifts to smaller and larger wavelengths upon expansion and contraction of the lattice.[17, 37, 44, 48, 49, 52] To be precise: The expansion of the particle leads to a decrease in electron density and therefore to a modification of the plasma frequency ω_p . Since the maximum position of the resonance is a function of ω_p (see equation 2.8 for spherical particles), the resonance changes accordingly. P. Zijlstra, in 2008, presented the simultaneous observation of two vibrational modes (breathing and extensional mode) in single nanorods.[53, 54] S. Park et al. used the method of optical heterodyne detected four-wave-mixing spectroscopy to simultaneously observe changes in the dispersive and absorptive part of the detected signal for a gold nanorod sample.[55] In 2011, the extensional mode of bipyramidal gold nanoparticles was investigated for a broad spectral range across the longitudinal plasmon resonance in transmission geometry, revealing a periodic shifting of the plasmon resonance upon vibration.[56] Moreover, A. Plech et al. have detected structural relaxation changes in protein labeled gold nanoparticles by time-resolved X-ray scattering measurements.[57] However, no quantitative analysis of the vibrational amplitudes has been given so far.

3 Experimental Methods I: Sample Preparation and Characterization

When this thesis work started, the UDKM group had no experience in the preparation of polyelectrolyte multilayer structures, in the incorporation of nanoparticles and the optical properties of such compound structures. The group was kindly introduced to the material properties and to the layer-by-layer deposition technique by the group from Prof. Möhwald, especially by Dr. Torsten K. Sievers.

The first section of this chapter gives an introduction to the fabrication of polyelectrolyte multilayers, including a description of their characteristic properties which play an important role in this thesis. Subsequently, all materials that were applied are listed, and finally, the characterization methods used for the analyzation of our polyelectrolyte multilayer samples are described.

3.1 Polyelectrolyte Multilayers with Embedded Nanoparticles

A polyelectrolyte is a molecule that is composed of monomers with identical chemical structure linked to each other. The monomers comprise an electrolyte group which dissolves upon contact with aqueous solution resulting in the charging of the polymer molecule. This charging bears the opportunity to electrostatically bond oppositely charged polyelectrolytes. A prominent method to grow polymeric multilayered samples is the layer-by-layer (LbL) assembly technique. Thereby, single monolayers are successively deposited with nanometer precision on a sample's surface. Early stage LbL experiments describe the alternate adsorption of positively and negatively charged particles and were proposed by Iler in the 1960s.[58] Several groups expanded the application of this method first to molecules and later to polyelectrolytes.[59, 60] The broad interest in these materials and their processing method is reflected by the large body of literature in which fundamental theories on the building process and various deposition techniques are described, studies of influential parameters are presented, and the incorporation of nano-objects is investigated.[61] Several reviews and feature articles summarize the evolution of this prominent method pointing out the possible future role in medicine, technology, and science.[3, 62, 63] In this thesis, two of the most common LbL deposition techniques are applied: the dip-coating and the spin-coating methods. In both methods, a negatively charged substrate is exposed to polyanionic aqueous solution until one monolayer is adsorbed by electrostatic bonding to the surface. Subsequently, the substrate is exposed to the polyanionic solution for the adsorption of the oppositely

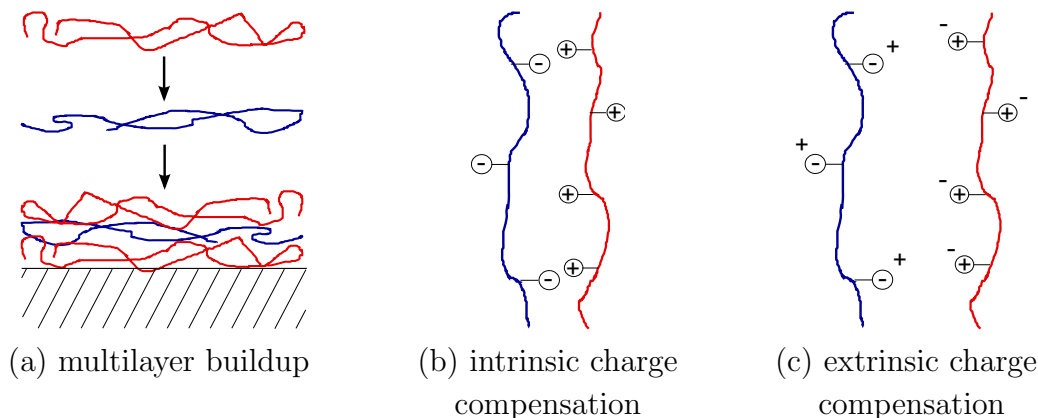


Figure 3.1: (a) In the layer-by-layer method, the polyelectrolyte layers are successively deposited on the topmost film. (b) and (c) illustrate the two complex formation processes. During intrinsic charge compensation, only the charged polyelectrolyte segments take part in complex building, while in the extrinsic one, Na^+ or Cl^- counterions are involved. (Modified after [64])

charged polyelectrolyte. Repeating these steps in an alternating manner leads to multilayered structures [see Figure 3.1 (a)]. In principle, there is no limit to the number of layers that can be deposited. K. M. Lenahan et al. reported on films consisting of more than 1000 layers.[65]

The driving force in the LbL process is based on the principle of maximizing entropy, which is the main statement of the second law of thermodynamics. In what sense this is related to the adsorption process can be understood by the common microscopic model of competitive ion pairing:[20, 66]

Low molecular weight ions, like Na^+ and Cl^- , are located in the vicinity of the polyelectrolyte chains and act as counterions (or screening ions) to the charged polyelectrolyte segments. These charged segments compete with the counterions on the polyelectrolyte molecule in the surface layer for bonding to that molecule. Figures 3.1 (b) and (c) demonstrate two types of charge compensation. The key difference in the intrinsic charge compensation (segment–segment bonds) in comparison with the extrinsic one (salt ions participate in neutralization) is that segment–segment bonding implies the release of counterions. By each release and intrinsic bond formation, the total number of degrees of freedom in the system increases and consequently the entropy increases. This effect is yet intensified by the subsequent dissociation of water ions. This dissociation is caused by the hydrophobic nature of the polyelectrolyte backbone which becomes more effective upon the release of hydrophilic salt ions. Immersing the multilayer structure after polyelectrolyte adsorption into deionized water removes all excess salt ions, and the final conformation is due solely to intrinsic charge compensation, that is, to segment–segment bonds. Only in the lowermost and surface layers, some ions remain. Since the total binding energy is

determined by the summation of all individual bonded segments, the restored energy in such polyelectrolyte multilayers is rather large. Schlenoff et al. have shown that this energy is proportional to the number of released water molecules.[67]

Generally, the applicability of the LbL assembly technique is not restricted to materials forming covalent bonds. Multilayers were successfully produced that rely on hydrogen bonding [68–70], van der Waals interaction, π – π bonding or donor–acceptor bonding. Above this, it is likely that more than one kind of interaction at a time contributes to the adsorption process.

The structural characteristics of the formed multilayer, such as layer thickness, surface roughness, internal structure, etc., rely on various parameters. The dependency of the adsorbed layer thickness, for example, was studied extensively for both the dip-coating and the spin-coating method.[71–74] A decisive parameter that was identified is, for example, the ionic strength, that is, the amount of sodium chloride (NaCl) added to the polyelectrolyte solution. With few counterions provided, thin layers are produced due to the repulsive segment–segment interactions of the polyelectrolyte molecule. In contrast, at high ionic strengths the polyelectrolyte charges are strongly screened such that segments experience only little repulsive forces. The molecule arranges in a curly way with loops and tails and consequently result in the conformation of thicker layers. Moreover, the layer thickness of the adsorbed material depends on the deposition technique used. Applying identical solutions, the spin-coating procedure leads to thicker layers than the dip-coating one. Since solutions for spin-coating typically possess a significantly higher polyelectrolyte concentration, this effect is yet enhanced.[75]

Within this thesis, polyelectrolyte multilayers are made out of poly(allylamine hydrochloride) (PAH) and poly(sodium 4-styrenesulfonate) (PSS). The solutions for dip-coating were prepared with 1/2 mol/l of NaCl and for the solutions for spin-coating with 1 mol/l of NaCl. The structures made of these polyelectrolytes using either assembly method show a linear growth behavior.[59, 76] The thickness of each adsorbed double layer measures around 2.2 nm and 2.5 nm for the dip- and the spin-assembled samples, respectively.

One frequently investigated feature of polyelectrolyte multilayers is the mobility of polyelectrolyte chains in the structures, because such structures never reach a thermodynamic equilibrium. The molecules inside the structure are rather in continuous motion, whereas their mobility determines to what extent these molecules interpenetrate each other, also after formation. A key parameter here is the polyelectrolyte charge density. Weakly charged polymers show strong chain mobilities and therefore an increased self diffusion which causes the elimination of any layered structures. This effect is also observed for polyelectrolytes that are screened by salt ions.[77, 78] Further parameters that were used to tailor other multilayer features are, for example, the adsorption duration, the type of salt and solvent, the pH value, the temperature, and the number of drying steps and their duration. For instance, L. Krasemann et al. and Klitzing et al. presented membranes with size selective permeability (porosity) by tuning the thickness porosity, structure, chem-

ical compositions, and the size of permeating components.[70, 79] Complexes or multilayers made out of PSS/PAH show a high stability and an almost no swelling behavior upon exposure to humidity or NaCl solution. This results from the high degree of association of the polyelectrolytes, their hydrophobic nature, and the low permeability.[66, 80]

The availability of a charged polyelectrolyte surface layer facilitates the adsorption of nanosized objects which possess a net surface charge. With further deposition of polyelectrolytes onto the adsorbed charged objects it is possible to fully incorporate these objects inside the polyelectrolyte structure. A comprehensive amount of literature is available which reports on successfully manufactured multilayer structures with incorporated objects such as: inorganic nanoparticles [2, 3, 71, 81–89], quantum dots[90], proteins[91], DNA[92], charged viruses[93], and many more.

The versatility which arises from the incorporation of functional objects and the multifunctionality of the polyelectrolytes themselves in combination with technical simplicity and low-cost materials is the reason for the high attractiveness of the layer-by-layer method of polyelectrolytes for devices and industrial products. A few applications that were reported recently comprises, for example, functional membranes[79, 94], capsules for drug delivery[7, 95, 96], sensing films[90, 97–99], photonic and photovoltaic devices[100–106], optical amplifiers[106], various coatings[87, 107–110], and many more.

3.2 Materials

3.2.1 Polyelectrolytes

All polyelectrolytes that were employed for sample preparation throughout this thesis are listed in table 3.1.

Polyelectrolyte	Abbreviation	M_w [kDa]	charge
Poly(sodium 4-styrenesulfonate)	PSS	70	anionic
Poly(allylamine hydrochloride)	PAH	70	cationic
Poly(ethyleneimine)	PEI	750	cationic

Table 3.1: List of the polyelectrolytes that were employed in this thesis work. All polymers were purchased from Sigma-Aldrich.

Poly(ethyleneimine)(PEI) is a branched cationic polyelectrolyte with a monomer molecular weight of 163.266 g/mol. It was delivered as a 50wt% aqueous solution. PEI is known for its strong adsorption properties and is therefore used as the first polyelectrolyte to be adsorbed on the substrate. Most importantly, it compensates for small inhomogeneities in the surface charge distribution of the substrate,

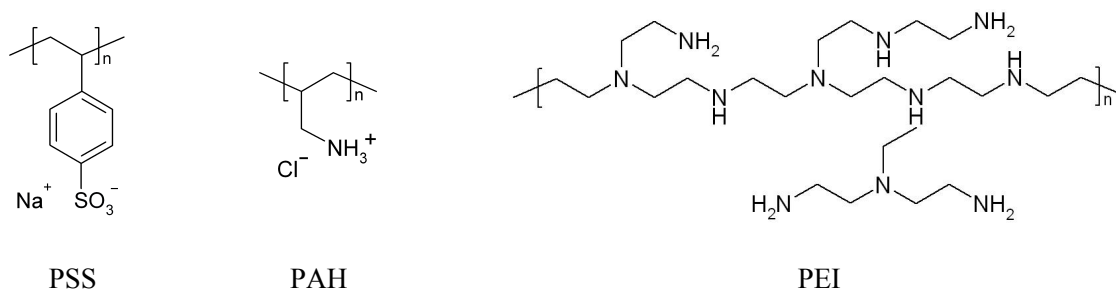


Figure 3.2: Chemical structures of the used polyelectrolytes. (Modified after [111])

which otherwise could cause defects in the multilayer structure. Poly(allylamine hydrochloride) (PAH) is a linear cationic polyelectrolyte with a monomer molecular weight of 93.56 g/mol. PAH is a weakly charged polyelectrolyte. Poly(sodium 4-styrenesulfonate) (PSS) is linear and anionic, and its monomer weight measures 206.20 g/mol. PSS was dialyzed against ultrapurified water from an ELGA (PURE-LAB Classic) water purifier system before application. All polyelectrolytes were purchased from Sigma-Aldrich Chemie GmbH (Germany).

The polyelectrolytes are soluble in water but possess a hydrophobic backbone. This hydrophobic backbone is responsible for the dissociation of water molecules when hydrophilic salt counterions are released.

3.2.2 Gold Nanoparticles

Gold nanoparticles with 10 nm and 20 nm diameter were purchased as colloidal suspensions from Sigma-Aldrich (item numbers: G1527-25ML and G1652-25ML, respectively). They were manufactured by the chemical reduction of chloroauric acid HAuCl_4 with trisodium citrate. As a result, anionic citrate molecules are linked to the surface of the readymade particles. These molecules prevent the colloids from clustering and facilitate their incorporation into a polyelectrolyte structure by adsorption onto positively charged PAH layers. The adsorbed gold particles create a negatively charged surface layer, allowing the LbL assembly to proceed with the next PAH layer. The particle concentrations in the solutions measure 0.01% by weight. For the dip-coating technique, the suspensions were used as delivered, whereas a diluted solution with ultrapurified water and a mixing ratio of 1:1 was prepared for the spin-coating technique. Particles with a diameter of 150 nm were purchased from British-Biocell-International (BBI). The manufacturing procedure is the same as for the particles from Sigma-Aldrich. The particle concentration in solution is specified to amount $1.66 \cdot 10^9$ particles/ml.

Note that particles were successfully adsorbed on polyelectrolyte layers only when using the colloidal solutions mentioned above. The attempt to use other particle solutions from Sigma-Aldrich or BBI remained unsuccessful.

3.2.3 Substrates

The standard substrates used throughout this thesis are transparent glass slides with 1–2 mm thickness that are suitable for characterization by optical spectroscopy. The slides were either made of soda-lime glass or fused silica glass, both having an amorphous structure. Due to the smoothing properties of PEI and PSS/PAH multilayers there is no requirement of perfectly flat substrate surfaces for manufacturing gold-nanoparticle/polyelectrolyte composites. Only for the purpose of roughness studies by means of atomic force microscopy, either silicon wafers or mica sheets were employed. Both possess a profoundly smooth surface with a roughness (root mean square) in the nanometer range. All mentioned substrates are suitable for X-ray reflectivity measurements.

It is worth mentioning that in optical spectroscopy using a coherent light source, measurements in reflection geometry give rise to interference effects due to reflections from either side of the substrate, which overlap in space and time on the detector. Using substrates with a thickness of at least 1 mm allows one to spatially separate the backside reflection of the substrate from the frontside one for a typical angle of incidence of 40° . Especially for low-roughness substrates it is important to detect the frontside reflection only. That is, for such substrates the wavelength of detection is typically two orders of magnitude higher than the surface roughness, such that the reflected intensities are rather large and may lead to a significant modulation of the detected reflectance due to interference.

3.3 Sample Preparation

3.3.1 Chemical Cleaning

The prerequisite condition of a substrate being suitable for the LbL process is the availability of a homogeneously negatively charged hydrophilic surface. Thorough cleaning is required in order to remove any organic residue from the surface. A widely applied method is the immersion of the glass substrate into peroxymonosulfuric acid. Thereby, a beaker glass with a substrate is partly filled with hydrogen peroxide H_2O_2 . Then, sulfuric acid H_2SO_4 is added accounting for a mixing ratio of about 3:1. After 20 min in the strongly oxidizing acid, the substrate is rinsed with purified water. A completely wetted surface proves the surface to be homogeneously hydrophilic. Peroxymonosulfuric acid is strongly explosive and must be handled with care.

Alternatively, glass slides and silicon wafers were cleaned by immersing them in an ultrasonic bath with acetone for 10 min. Also, here, a complete wetting of the surface was observed, evidencing it to be homogeneously hydrophilic. Since this method is less hazardous and much simpler to apply, it became the standard cleaning routine. AFM measurements additionally confirmed the surface to be free of organic residues. Mica substrates are made of multilayered crystalline sheets which are rather elastic.

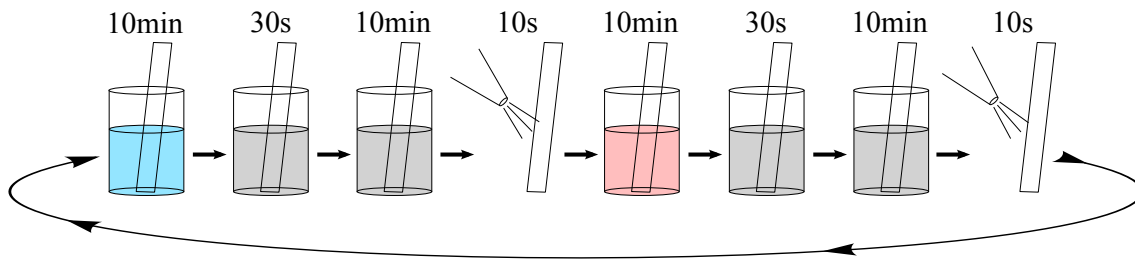


Figure 3.3: Schematic presentation of the preparation procedure according to the dip-coating technique. After the adsorption of the polyelectrolytes (red and blue), two washing steps are carried out (grey), followed by a drying step with a nitrogen air blowing unit. The specified durations are waiting times after immersion of the substrate into the respective material or times which describe the duration of the nitrogen air blow.

These substrates are cleaned by simply pulling of the top layer with adhesive tape.

3.3.2 Dip Coating

The solutions for the dipping procedure were prepared to have a polymer concentration of 10^{-3} mol/l and NaCl concentration of 1/2 mol/l. The preparation procedure is visualized in figure 3.3. Each polyelectrolyte layer adsorption cycle implies four steps. First, the substrate is immersed into the polyelectrolyte solution for 10 min. This duration is beyond the saturation time of the polyelectrolyte adsorption process. This time is chosen in order to assure the reproducibility of defined thicknesses. The adsorption rate for the dipping process is exclusively defined by the diffusion constant. A short rinsing step that implies dipping into pure deionized water for 30 seconds is followed by a thorough bath in deionized water for 10 min. During these steps, excess polyelectrolytes that are only loosely bound are washed off. Salt ions, which were introduced into the structure during each polyelectrolyte adsorption step are removed from the structure and only few ions remain in the surface layer. Finally, the surface is dried with nitrogen air. The next adsorption cycle starts with the oppositely charged polyelectrolyte. Alternating dipping is performed until the film has the desired thickness. Implementation of gold particles into the sample is achieved by replacing one PSS adsorption cycle with the one for gold nanoparticles. Therefore, the sample is immersed into the gold solution for 60 min, then rinsed with deionized water in two stages again, and finally dried as before. The next layer to be adsorbed is again PAH.

The entire dipping procedure was carried out by a computer controlled dipping robot. This allowed to prepare samples with manufacturing times up to several days without interruption. In order to assure a uniform sample growth, it is necessary to keep the environmental circumstances constant throughout the process. The purity of the washing water and the polyelectrolyte and NaCl concentration in

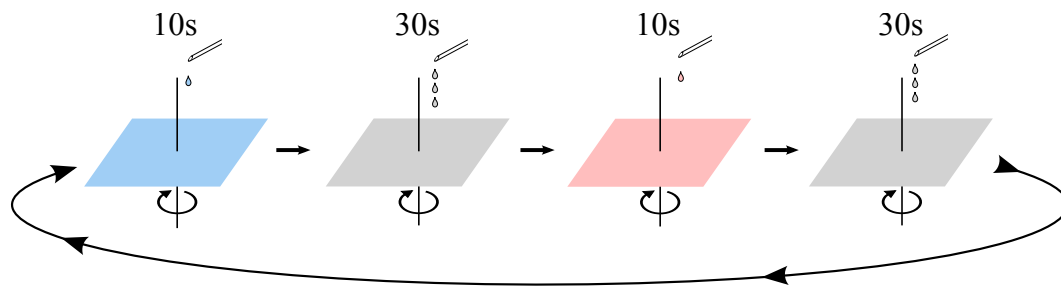


Figure 3.4: Schematic presentation of the preparation procedure for polyelectrolyte multilayers according to the spin-coating LbL technique. The specified durations are waiting times after dispersion of the respective material until the next step is executed. The spin-coater is constantly running throughout this process. (Modified after [111])

solution was maintained by regularly replacement with fresh material. However, it was not possible to control the humidity of the ambient air.

3.3.3 Spin Coating

The polyelectrolyte concentration for the spin-coating solutions is adjusted to 10^{-3} mol/l with 1 mol/l of NaCl. The spin coater is run continuously with a constant spin speed of 3000 rpm throughout the polyelectrolyte multilayer assembly. The preparation procedure is visualized in figure 3.4. One polyelectrolyte-layer assembly cycle composes the following steps: First, about 0.02 ml of the polyelectrolyte solution is dispensed onto the substrate's centre so that it immediately covers the entire surface due to centrifugal forces. After 10 s the liquid film is washed off by successively giving three drops of purified water onto the sample in order to remove the excess polyelectrolyte and salt. By waiting for another 30 s while spinning, the surface is dried and the next polyelectrolyte layer of opposite charge can be deposited likewise.

For the purpose of incorporating the gold particles, the spin coater is stopped and the sample is completely wetted with approximately 0.5 ml gold suspension. After a waiting period of 60 min, before the suspension is dried up, it is spun off at a speed of 1000 rpm. The sample is then rinsed with three drops of purified water as before. N_2 gas flow is used to support the drying process as the rotation speed of 1000 rpm is rather slow. The preparation continues with the next PAH layer. Also, here, rinsing is important as it removes excess gold particles which would aggregate during drying and it washes off excess salt ions which otherwise would crystallize. The spin coater (Laurell) used for preparing the samples basically consists of a nitrogen flooded chamber equipped with a rotary disc. This disc is attached to a vacuum pump which affixes the sample to the disc by generating a low-pressure vacuum. Parameters such as spin-speed, spin-duration, and acceleration are computer

controlled, whereas the dispensing of solution is carried out manually with syringes. The adsorption rate in the spinning process is considerably increased by a high polyelectrolyte concentration and by the centrifugal forces that act on the polyelectrolyte molecules in the solution.[112] The time required to deposit one double layer of polyelectrolyte is 20 s as compared to 40 min by dip coating.

3.3.4 Dipping vs. Spinning

The key advantage of dip coating is the independence of the substrate size and shape, whereas spin coating is restricted to flat surfaces. Thus, this method is capable of coating spherical, cylindrical, concave, convex or even hollow objects. Capsules used for drug delivery are for example fabricated by LbL deposition of polyelectrolytes on colloidal particles. After decomposition of this particle a hollow sphere remains.[113] The only requirement is that the surface has to be initially charged. The main drawback of dip coating is that it is a material- and time-consuming method. The fabrication of a typical dip-coated sample takes 1–2 days, whereas an equivalent spin-coated one is manufactured within 5 h only. This duration of assembly can be critical since the environmental conditions such as temperature and humidity have to be kept stable throughout the preparation process. Also, the polyelectrolyte and NaCl concentrations in the solution and the pureness of the rinsing water must be maintained. Preparing non-flat substrates within significantly shorter durations could be achieved by applying a hydrodynamic method. Thereby, the substrate is spun inside the polyelectrolyte solution such that advection contributes to the adsorption process resulting in a faster adsorption rate.[62, 114]

It is the first task of this thesis to investigate and compare the stratification of gold-nanoparticle layers in spin- and in dip-coated samples.

3.4 Sample Characterization Methods

The structural characterization that is carried out in this thesis comprises the analysis of the sample's thickness, its surface roughness, and the stratification of the gold layers in the structure. The optical examination methods additionally facilitate the derivation of the complex refractive index and hence of the static dielectric function. The samples were tested for a possible birefringence, and the space filling factor was identified, which is defined as the fraction of the gold particle volume on the total sample volume $f = \frac{V_{particles}}{V_{particles+medium}}$. The applied methods are nondestructive except for transmission electron microscopy measurements, which require the slicing of the sample into thin cross-sectional layers. Also, thickness measurements by means of an AFM imply the scratching of the sample layer so that the difference in height can be measured.

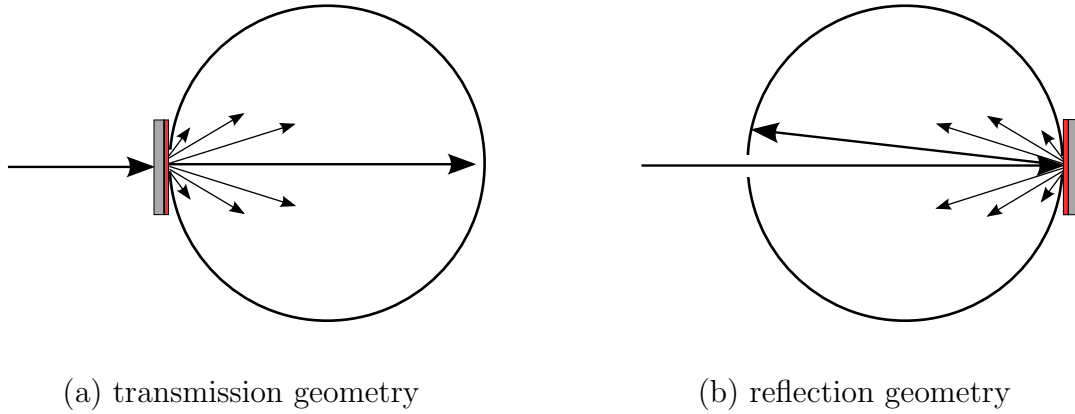


Figure 3.5: Schematic presentation of the detection setup in the UV-Vis-NIR spectrometer using an integrating sphere (Ulbricht sphere). This sphere detects both the specular and the diffuse scattering components. Adjustments are possible in which only the diffuse scattering contributions are measured (not shown here).

3.4.1 UV-Vis Spectroscopy

Transmittances and reflectances are measured with an UV-Vis-NIR spectrophotometer (VARIAN CARY 5000) for wavelengths ranging from 200 nm to 800 nm. The samples are oriented at normal incidence and the transmitted/reflected light is detected with an InGaAs integrating sphere (Ulbricht sphere) as visualized in figure 3.5. The resulting spectra comprise the specular and the diffuse forward and backward scattering contributions.

In order to exactly determine the absorption of a sample, it is essential to measure both, the transmittance and the reflectance. The absorption A is given by $A = 1 - T_{sd} - R_{sd}$, where the subscript sd indicates that the specular and diffuse contributions have to be taken into account here. In order to exclusively determine specular components, the diffuse scattering spectra R_d and T_d are measured separately and are subtracted from the overall transmitted/reflected spectra T_{sd} and R_{sd} .

3.4.2 X-Ray Reflectometry

Small angle X-ray reflectometry is a prominent method to investigate thin layered samples. Besides the ability to derive parameters describing the thicknesses of layers, this method is particularly useful to analyze the structure of interfaces and thus the stratification of particle layers. The comparison of the measured X-ray reflectivity with a simulation that is based on an estimated electron density distribution provides an insight into the particle distribution within the sample. The experiments were performed at the EDR beamline of the electron storage ring Bessy II at the

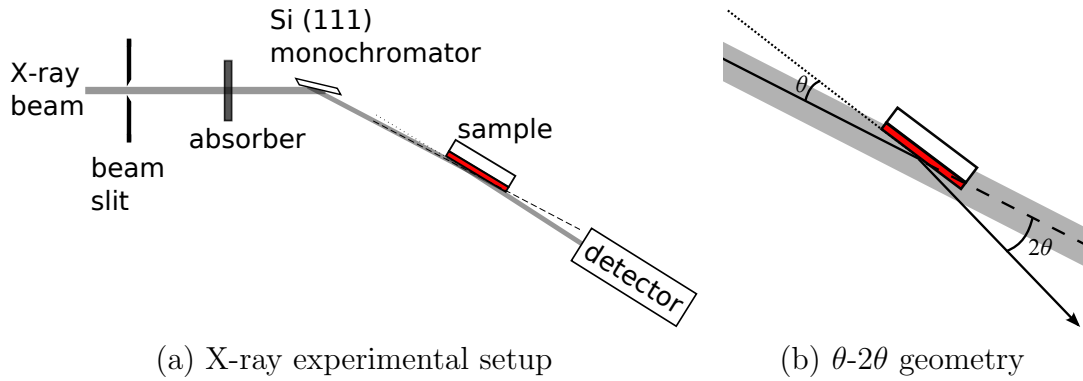


Figure 3.6: (a) Experimental setup at Bessy II for XRR measurements. (b) Illustration of the θ - 2θ geometry. This picture also visualizes the effect that with higher θ -angles, a larger cross-sectional area of the wide X-ray beam is filled out.

Helmholtz Centre Berlin. The continuous X-ray radiation ranging from 4 keV to 30 keV is monochromatized by a Si 111 monochromator.

The samples were investigated by performing a θ - 2θ scan in which the reflected intensity of the parallel and monochromatic beam is detected for varying angles (Figure 3.6). Since the actual reflected wavelength (energy) of the monochromator depends on the provided angle of incidence according to Bragg's reflection law, it is identified by using an energy dispersive detector with 4000 channels. This detector must be calibrated before application, which is achieved by investigating the X-ray fluorescence of a known probe sample, wherein the known energies of fluorescences are assigned to the channels of maximum detected intensity and by linear interpolation, and the energy for each channel is determined.

The θ - 2θ scan was performed for grazing incidence angles of $0.01^\circ < \theta < 1^\circ$. According to the X-ray nomenclature, θ is defined as the angle between the incoming beam and the sample's surface, as indicated in figure 3.6 (b). The critical angle for total external reflection is around $\theta_c = 0.18^\circ$, which is determined by the refractive indices of the environment and the sample. In the vicinity of the critical angle, the reflected intensity drastically changes by four orders of magnitude. Thus, the complete angular range was measured in four steps, each time using a different absorber. The application of absorbers is important in order to avoid very high counting rates which could lead to a saturation of the detector which in turn leads to erroneous measurements and possible damage to the detector. Before evaluation, the measured data were normalized to the respective absorbance and were linked together.

In addition, a correction to the measured intensity has to be carried out, which arises from the fact that for grazing incidence angles, the X-ray beam is much wider than the sample as visualized in figure 3.6 (b). Consequently, when rotating the sample to higher values of θ , it fills out a larger cross-sectional area of the beam such that an increasing amount of photons hit the sample and is being reflected.

This effect is taken into account by correcting the detected intensity by a factor of $\sin(\theta)^{-1}$, which corresponds to the increase in the beam cross-sectional area that is being taken up by the sample upon rotation. As a result, the detected intensity is constant for $\theta < \theta_c$, as required.

3.4.3 Atomic Force Microscopy

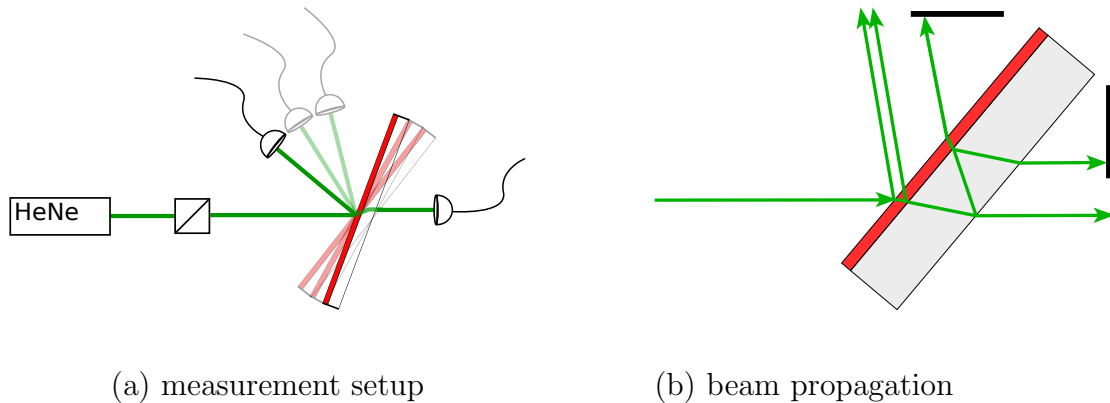
In AFM, the surface topography of a sample is analyzed by scanning a defined area with a sharp metal tip. This tip is attached to an elastic cantilever which is bent to a greater or lesser extent according to the position of the tip. Laser light, which is reflected from that cantilever, is used to detect minimal movements of the tip down to several angstroms. Here, the AFM is operated in the tapping mode. Piezoelectric actuators set the cantilever into vibrational motion at a frequency which is close to the resonance frequency of the cantilever. Moving the tip close to the surface, it interacts with the sample surface and the amplitude and frequency are modified. While scanning the area of interest using an x-y translation stage, the tip's vibrational motion is detected and a topographical map of the investigated area is generated.

This method is particularly suitable for investigations of soft-matter samples since the forces exerted on the surface are considerably reduced compared to the contact mode. In that mode, the tip is in contact with the surface throughout the measurement process. Especially shear forces during translational motion cause damage to the samples and inhibit the measurement of correct topography images.

Besides the surface analysis, this microscopy setup was used to measure the thickness of sample layers. Therefore, the sample is scratched with a scalpel such that the polyelectrolyte-gold material is removed and the substrate is laid open. Then, a profile measurement across the scratch reveals the difference in height between the substrate and the layer surface. For such measurements, all described substrates are suitable, except mica sheets, which are too soft and usually get damaged during mechanical removal with a scalpel.

3.4.4 Angular-Dependent Reflectance and Transmittance

Static angular resolved reflection and transmission experiments are performed using a commercial helium–neon laser (Thorlabs) with an operational wavelength of 543 nm. The intensities of transmission and reflection are taken for α angles ranging from 20° to 85°, where α is defined as the angle between the incident beam and the surface normal. The according measurement setup is pictured in figure 3.7 (a).



(a) measurement setup

(b) beam propagation

Figure 3.7: (a) Setup for angle-dependent reflectance and transmittance measurements. The polarizer assures the HeNe light to be purely s - or p -polarized. (b) Typically both reflections from the sample layer interfaces are detected, but the transmitted and reflected beams from the rear substrate interface are blocked.

Incorporating a polarizer behind the laser output allows for adjusting the polarization and assures this to be stable. Measurements are performed once with parallel (p -polarized) and once with perpendicular (s -polarized) orientation of the electric field. Since such lasers typically show minor polarization or intensity instabilities, the incident intensity is always recorded along with the detection of the transmitted or reflected light.

It is important to take into account interference effects resulting from the interaction of the reflection from the substrate's backside with the sample layer reflections. In order to inhibit any alteration of the reflected intensity, the reflection from the backside of the substrate is blocked, as depicted in figure 3.7 (b). It is therefore necessary to use substrates of at least 1 mm thickness such that the reflections are clearly separated in space.

4 Experimental Methods II: Ultrafast Pump-Probe Spectroscopy

This chapter provides a short introduction to optical ultrafast pump-probe spectroscopy. A brief specification of the commercial laser system is followed by a detailed description of the self-built optical setups for white-light continuum (wlc) generation and ultrashort pulse generation with tunable wavelengths. The construction of this experimental setup represents an essential part of this thesis as no optical measuring facility existed when this thesis work started.

The generated laser pulses are characterized with regard to their spectrum and pulse duration. Finally, the principle of pump-probe spectroscopy is explained and sketches for each optical setup are presented.

4.1 Experimental Setup for Pump-Probe Spectroscopy

4.1.1 Ti:Sapphire Laser System

All optical time-resolved experiments in this thesis were performed with a commercial regenerative amplified femtosecond laser system from Spectra-Physics. The system consists of a high-repetition rate oscillator (MaiTai) and an amplification unit (Spitfire Pro), which is pumped by a high-power laser (Empower). Both the oscillator and amplifier unit comprise a Ti:sapphire crystal as active medium. The amplifier is operated at a wavelength of 795 nm at a repetition rate of 5 kHz. It is specified to provide pulses shorter than 120 fs with a pulse energy of 340 μJ . The beam is *p*-polarized and its profile measures 7 mm in diameter.

The MaiTai oscillator is a wideband tunable actively mode-locked Ti:sapphire laser that emits femtosecond (<100 fs) pulses with a repetition rate of 80 MHz. Its tunability ranges from 710 nm to 920 nm; however, the optimum wavelength is around 795 nm, where the pulse energy measures about 20 nJ (average power > 1.5 W). The outgoing beam is *p*-polarized, i.e., the polarization ratio measures *p*-pol:*s*-pol $> 500:1$. This oscillator is a sealed-off laser system which requires no maintenance such as cleaning or readjustment by the user. Reliable mode-locking is ensured by a regeneratively controlled acousto-optic modulator. Only a small fraction of the provided power is guided as the seed into the amplification unit such that the remaining energy is available for other applications.

Amplification in Spitfire Pro is performed according to the principle of “chirped pulse amplification”. Thereby, temporally stretching of the MaiTai seed pulses to several

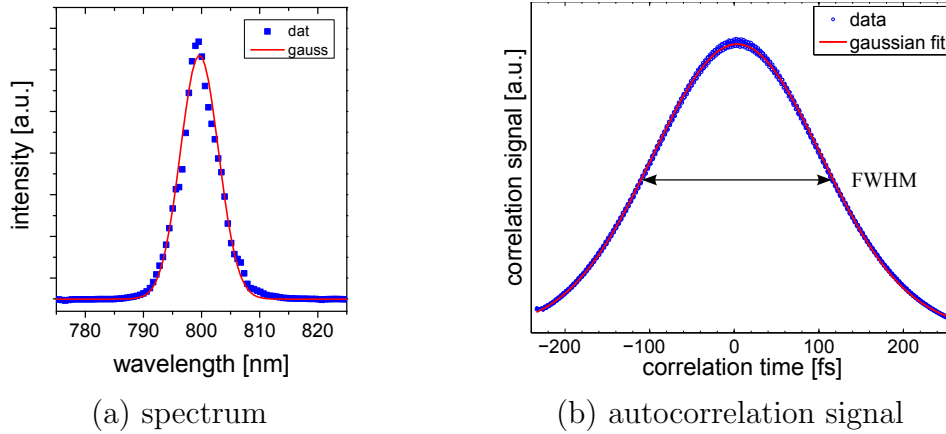


Figure 4.1: (a) Measured spectrum of the Spitfire Pro laser system (blue symbols). The red line is a Gaussian fit to the data. (b) The measured (blue symbols) and fitted (red line) autocorrelation signals define the laser pulse length to measure 165 fs (FWHM).

picoseconds considerably reduces the power density in the Ti:Sapphire crystal during amplification. In this way, the crystal is prevented from being damaged due to high peak powers of femtosecond laser pulses. Therefore Spitfire Pro comprises an optical stretcher, the regenerative amplifier unit, and an optical compressor. First, the oscillator seed pulses pass the optical stretcher, which basically consists of a highly dispersive grating and an optical path. The spectral beam components are spatially dispersed by the grating and the optical path is aligned such that the red components travel a slightly longer path than the blue components. This induces a positive chirp such that the pulse length increases and the laser power density is significantly reduced. Pockels cells then select pulses with a repetition rate of 5 kHz. These pulses are guided into the cavity, where they are regeneratively amplified in the Ti:sapphire crystal, which is pumped by the high-power (11 W) Empower laser at 532 nm. Each pulse passes the crystal at least 20 times until the gain is saturated. The pulses are then coupled out and guided to the optical compressor, which finally reduces the pulse length by producing a negative chirp. Pulse-to-pulse fluctuations (RMS), which are measured each time the laser is switched on and off, typically amount to 0.46.

4.1.2 Noncollinear Optical Parametric Amplifier

The amount of energy that is deposited in a sample by laser light illumination is decisively determined by the wavelength-dependent absorption coefficient. For a typical gold-nanoparticle composite as used in this thesis, the maximum absorption occurs at around 540 nm leading to an absorption of about 40%. Therefore, the ability of tuning the pump wavelength is crucial in order to effectively excite the electronic system of a sample. While laser pulses can be easily adjusted from 800

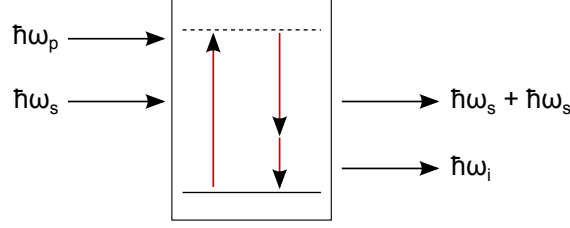


Figure 4.2: Photonic description of the difference frequency mixing process.

nm to 400 nm by second harmonic generation (SHG) in a nonlinear crystal, the conversion to wavelengths in the visible spectrum is more complex. By parametric amplification it is possible to amplify a low-intensity signal beam (ω_s) by difference frequency mixing with an intense pump beam (ω_p). This process allows one to adjust the signal beam to a particular wavelength provided that $\omega_s < \omega_p$. A tool that exploits this process and that proves to be extremely useful for the generation of ultrashort laser pulses with tunable frequencies in the visible range is the noncollinear parametric amplifier (NOPA).[115–117] It has become a common instrument in ultrafast optical pump-probe spectroscopy in order to investigate processes that take part on a time scale of a few hundred femtoseconds. In the parametric amplification process in the NOPA, two electric fields with frequency ω_p and ω_s interact in a 2-mm type-I β -barium borate (BBO) crystal and induce a second-order polarization of the following form:

$$\begin{aligned}
 P^{(2)}(x, t) = \frac{1}{4}\epsilon_0\chi^{(2)} & [E(x, \omega_p)E(x, \omega_p)e^{j2\omega_p t} + E(x, \omega_s)E(x, \omega_s)e^{j2\omega_s t} \\
 & + 2E(x, \omega_p)E(x, \omega_s)e^{j(\omega_p+\omega_s)t} + 2E^*(x, \omega_p)E(x, \omega_s)e^{j(\omega_p-\omega_s)t} \\
 & + E(x, \omega_p)E^*(x, \omega_p) + E(x, \omega_s)E^*(x, \omega_s)] \\
 & + cc .
 \end{aligned} \tag{4.1}$$

In order that an electromagnetic wave with frequency ω_i is generated, it must efficiently couple to one component of the polarization wave given in equation 4.1. Only if these two waves match in their wavevectors, the generated wave (ω_i) is constantly driven by the polarization wave throughout the crystal and its amplitude steadily increases. This is possible in birefringent materials only because waves with different frequency would always disperse in a linear optical medium. In the difference frequency mixing process, phase matching of ω_i and ω_p in the BBO is satisfied if $k_i = k_p - k_s$. The polarization expression can thus be reduced to

$$P^{(2)}(x, t) = \frac{1}{2}\epsilon_0\chi^{(2)} E(x, \omega_p)E^*(x, \omega_s)e^{-j(k_p-k_s)x-(\omega_p-\omega_s)t} + cc . \tag{4.2}$$

This polarization gives rise to an electromagnetic wave with frequency ω_i that is described by

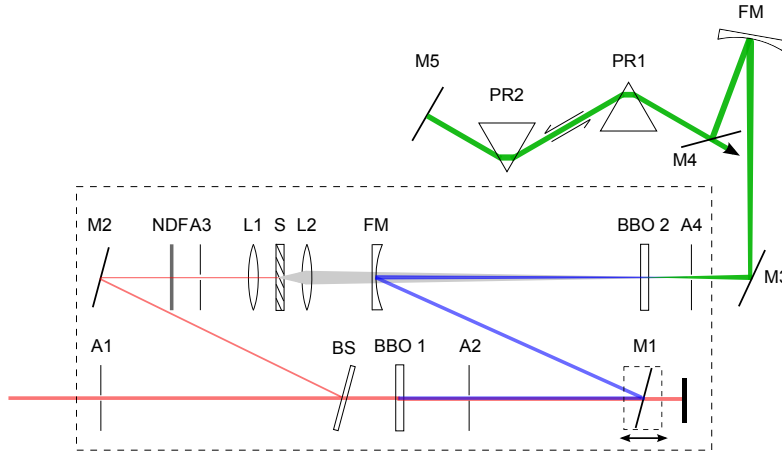


Figure 4.3: Setup of the noncollinear optical parametric amplifier, called NOPA, (dashed lined box) and a two-prism compressor. Used abbreviations: A = aperture, BS = beamsplitter, BBO = β -barium borate crystal, M = mirror, NDF = neutral density filter, L = lens, S = sapphire plate, FM = focusing mirror, and PR = prism.

$$E_{\omega_i}(x, t) = \frac{1}{2}E(\omega_i)e^{-j(k_i x - \omega_i t)} + cc. \quad (4.3)$$

Once this idler beam is generated, it in turn starts to interact with the intense pump beam, resulting in an amplification of the signal wave with wavevector $k_s = k_p - k_i$. In this way, the signal wave and the idler beam provoke a mutual intensity buildup with an exponential increase. The signal wavelength can take values ranging from $\omega_p/2$ to ω_p , according to the degeneration condition. Consequently, the idler's wavelength varies between $\omega_p/2$ and 0. For a BBO with a surface cut at $\theta = 29.2^\circ$, a signal wavelength of 535 nm, and a pump wavelength of 400 nm, the phase matching condition is fulfilled for an external noncollinearity angle between the pump and signal of 6.3° .

Figure 4.2 presents a photonic description of this process. Thereby, the nonlinear material (BBO) is excited by a high energetic pump photon to a higher virtual energy level. A signal beam photon with a variable frequency subsequently forces the relaxation by the stimulated emission of another photon with the same energy and momentum. In this way, energy is transferred from the intense pump beam with a fixed frequency to the low-intensity beam with a tunable wavelength. Simultaneously, with the stimulated emission of the signal photon, an idler photon is generated. With this photon, the conditions of conservation of energy and momentum are fulfilled. Its frequency is determined by the difference in frequency of the pump and signal photon.

The NOPA setup, as shown in figure 4.3, is a slightly modified version of the NOPA slim design invented by E. Riedle and coworkers. The setup is fed with 795 nm pulses from Spitfire Pro with a pulse energy of about 12 μJ . First, two apertures behind

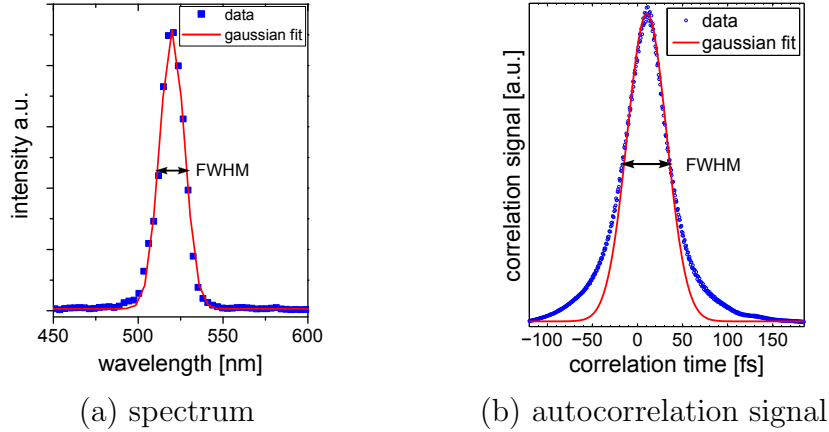


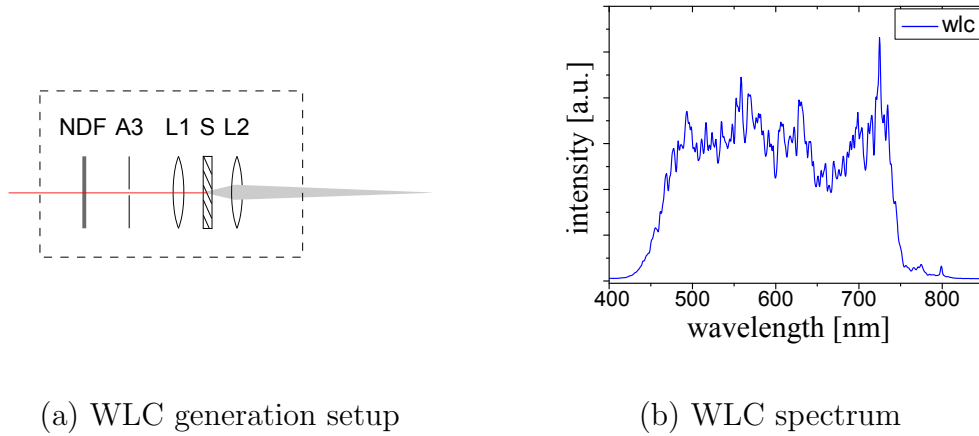
Figure 4.4: (a) The measured and fitted NOPA beam spectrum reveals a spectral bandwidth of ~ 15 nm. (b) From the according autocorrelation signal, the pulse length can be determined to measure ~ 55 fs (FWHM).

the entry allow for the readjustment of the beam path. A 1-mm uncoated glass slide is used as a beamsplitter to reflect 4% of the laser energy. This low-intensity fraction is used to generate a white-light continuum (wlc). A detailed description of this setup is given below in section 4.1.3. The generated beam with wavelengths ranging from 400 nm to about 900 nm has a pulse length of about 3 ps due to a strong dispersion. It is collimated by a lens ($f = 25$ mm) and is focused into BBO 2. The major intensity part is first frequency-doubled in the 500- μ m BBO 1 to ~ 400 nm and is then guided via a delay stage and a focusing mirror into BBO 2. This focusing mirror is displaced in height according to the noncollinearity required for phase matching of the pump and signal beams.

The phase matching angle is adjusted by blocking the signal beam and tilting the BBO such that the pump beam generates an intense fluorescence ring (transmitted parametric fluorescence). This transmitted parametric fluorescence is based as well on difference frequency mixing but is triggered by quantum fluctuations. Its intensity is a measure of the quality of the phase matching angle alignment. At the maximum intensity, the phase matching angle is optimally aligned and energy can be efficiently transferred from the pump to the signal beam, provided that pump and signal temporarily and spatially overlap in that crystal.

Changing the delay of the pump beam allows one to select the spectral part of the chirped wlc that is used for difference frequency mixing with the pump beam. In this way, the idler and signal wavelengths are tuned.

The bandwidth of the outgoing signal pulse is tuned to about 20 nm. This spectral range determines the Fourier-transform-limited pulse length of 35 fs, which is defined as the minimum length that the pulses can be compressed to. Due to the generation process itself and because of the transition through dispersive media, the signal pulse is a few hundred fs long. A SF10 (heavy flint glass) two-prism compressor is used to compress the pulses down to ~ 50 fs [see Figure 4.4 (b)]. Since



(a) WLC generation setup

(b) WLC spectrum

Figure 4.5: (a) Setup for wlc generation. Used abbreviations: NDF = neutral density filter, A = aperture, L = lens, and S = sapphire plate. (b) The measured spectrum. A filter was used for the attenuation of wavelengths above 750 nm.

this is already much shorter than the time resolution due to the probe pulse (~ 120 fs), no stronger compression is required. With a quartz prism compressor it would be possible to compress the pulses to ~ 35 fs and with a more sophisticated setup a compression to even shorter pulses could be realized.[117]

The signal beam power behind the BBO 2 at the NOPA exit measures about 60 mW, which corresponds to a pulse energy of $12 \mu\text{J}$. The corresponding conversion efficiency is higher than the typical NOPA efficiency of about 10%. The prism compressor, which includes the transmission of eight surfaces, considerably reduces the output energy to about 45 mW.

After NOPA alignment, the laser's chirp is readjusted such that the NOPA output is maximized. This means that a prechirp is given to the laser pulses, which is later compensated by the dispersive material in the beam path between the laser output and the NOPA difference frequency mixing. It is worth mentioning that only a power of ~ 430 mW is guided into the NOPA and 1.3 W remain which are being used for other applications.

4.1.3 White-Light Continuum Generation and Frequency Resolved Optical Gating

The broadband optical response of a sample upon laser pulse excitation is studied by detecting the transmittance and reflectance of a wlc probe beam. This beam is generated by focusing laser pulses (795 nm) with an energy of less than $2 \mu\text{J}$ into a 2 mm thick sapphire disc, according to the setup presented in figure 4.5 (a). The collimating BK7 lens with a 25-mm focal length assures high energy densities inside the disc. This energy density is yet increased due to self-focusing of the beam and results in the generation of a pulsed single-filament wlc.[118] A spectrum of such

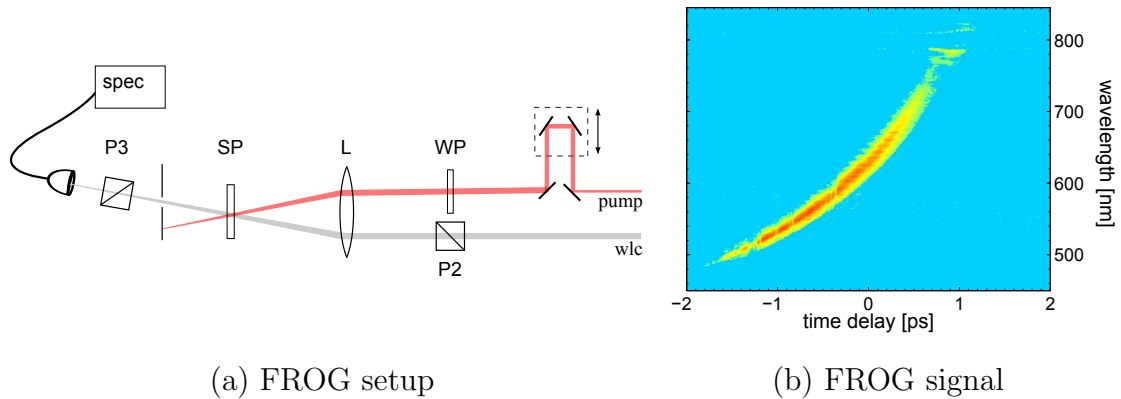


Figure 4.6: (a) Setup for “frequency-resolved optical gating” (FROG). Used abbreviations: WP = waveplate, P = polarizer, L = lens, and SP = sapphire plate. (b) Measured FROG signal.

typical white-light pulses is shown in figure 4.5 (b). It typically ranges from 450 nm to about 850 nm with a uniform intensity distribution, except around 795 nm where the fundamental mode dominates. In the shown spectrum in figure 4.5 (b), a filter (calflex-x) was used to suppress this mode in order to protect the detector. Due to dispersion in the sapphire disc and the collimating optic, the wlc pulse is strongly chirped. For the probing process, however, pulse compression is not required as long as the temporal dependence of the spectrum is known. This allows one to implement a correction algorithm in the evaluation routine, which determines the temporal zero for each wavelength individually.

Therefore, the chirp is experimentally determined by frequency resolved optical gating (FROG).[119, 120] A sketch of the corresponding setup is given in figure 4.6 (a). The p -polarized wlc beam is focused into a $100\ \mu\text{m}$ thin cover glass slide. An analyzer (polarizer) in front of the detection optic is adjusted to transmit only s -polarized light, preventing the wlc to pass so that no light is detected. High-intensity ($\sim 600\ \mu\text{J}$) gate pulses at 795 nm are then focused into the cover glass slide. Since these pulses have a pulse length of ~ 165 fs, they temporarily overlap with a narrowband fraction of the wlc spectrum (~ 3 ps) only. Upon their interaction, $\chi^{(3)}$ processes induce s -polarized components in the present spectral fraction of the wlc which then can pass through the analyzer and can be detected by the fiber spectrometer. For the best possible signal, the gate pulses must possess a linear polarization which is rotated by 45° relative to the signal beam. A two-dimensional FROG trace is taken by detecting the transmitted spectral components as a function of the delay between the signal and the gate pulse.

FROG characterization shows that the probe beam comprises wavelengths ranging from 440 nm to 810 nm. The leading red components exhibit a cross correlation of 120 fs, while the delayed blue ones measure 80 fs only. These durations limit the time resolution of the pump-probe setup, provided that the NOPA pulse length is shorter. However, a rigorous compression of the NOPA pulses to the Fourier-

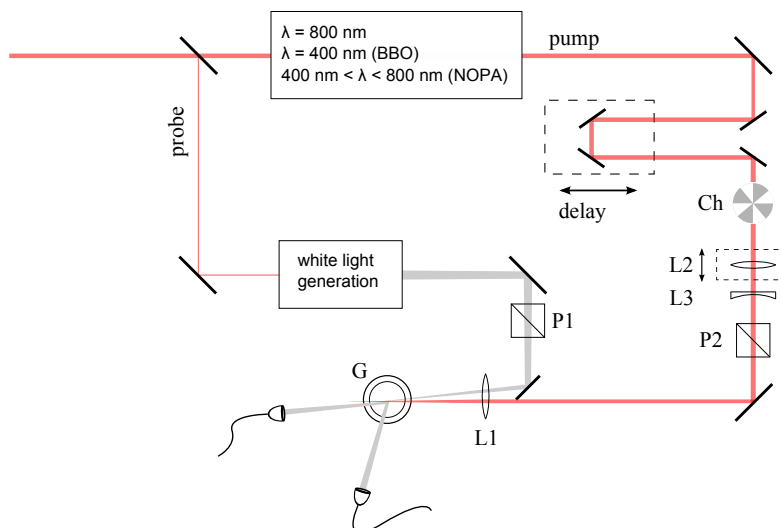


Figure 4.7: Pump-probe spectroscopy setup. In this setup a two-channel spectrometer simultaneously detects the reflectance and transmittance. Used abbreviations: L = lens, Ch = chopper, P = polarizer, G = goniometer.

transform-limited pulse length is not required. From the pulse duration of the gate pulse [shown in figure 4.1 (b)] and from the cross correlation signal, the time-zero (pulse overlap) for each probe wavelength is calculated with an accuracy of ~ 30 fs.

4.1.4 Ultrafast Pump-Probe Spectroscopy

In pump-probe spectroscopy experiments, an intense pulse (pump) excites a sample and a succeeding low-intensity pulse (probe) is used to measure the response of the system by detecting its reflection and transmission. Figure 4.7 presents an illustration of the setup. An integrated delay stage determines the moment of probing after excitation by regulating the path length difference between the pump and the probe beam. Its minimum step width of $2 \mu\text{m}$ corresponds to a temporal delay of 13.3 fs. By varying the position of the delay stage, the response of the sample upon excitation is recorded as a function of the delay time. In this setup, a beamsplitter first reflects $2 \mu\text{J}$ of the incident pulse energy for wlc generation, as described in section 4.1.3. The wlc beam is then directed onto the sample and its reflection and transmission are recorded simultaneously by a two-channel fiber spectrometer (Avantes). The remaining $\sim 300 \mu\text{J}$ are used for the excitation of the sample. They are either converted by sum frequency mixing to ~ 400 nm or guided into the NOPA for generating pulses with a wavelength of $400 \text{ nm} < \lambda < 800$ nm, or they remain unchanged. Either pulses are guided via the delay stage toward a telescope, which

is used to reduce the beam diameter. Therefore a convex lens ($f = 150$ mm) first focuses the beam. At a distance of 7.5 cm away, a concave lens with a focal length of 75 mm collimates the beam to a resulting diameter of 3.5 mm (initially 7 mm). Finally, this beam is focused onto the sample for excitation. This setup is used for measuring relative changes of the system upon excitation, such that each data point represents the normalized difference of the pumped and unpumped spectra. That is, a chopper inside the pump beam periodically blocks the pump beam with a frequency of 20 Hz, resulting in a period for one open-closed cycle of 50 ms. First, the signal of the probe beam with blocked pump is detected (dark spectra: R_0, T_0) followed by the measurement of the modulated reflectance and transmittance due to the excitation during the open cycle (R_{pump}, T_{pump}). The difference of these is finally normalized to the dark spectra, which determines the relative change in reflectance and transmittance:

$$dR = \frac{R_{pump} - R_0}{R_0} \quad \text{and} \quad dT = \frac{T_{pump} - T_0}{T_0} \quad (4.4)$$

Pump-probe spectroscopy has become a versatile tool for the study of time dependent processes that occur on time scales down to a few femtoseconds. The time resolution is solely determined by the pulse durations and is independent of the speed of the implemented electronic devices.

Time Zero In order to determine the temporal overlap of the pump and probe pulses, the process of sum frequency mixing in a BBO is exploited. Therefore, both the pump and probe beams, are focused into the BBO which is placed exactly at the position of the sample. Only when the two beams temporarily interact, the second-order nonlinear susceptibility χ^2 generates an electromagnetic wave with frequency $\omega_{sum} = \omega_{pump} + \omega_{probe}$, provided that the phase matching condition $k_{sum} = k_{pump} + k_{probe}$ is satisfied. Since the wlc probe beam is dominated by the 795 nm fundamental, the resulting frequency measures ~ 400 nm. Changing the delay between the pump and probe beams facilitates one to locate the position of temporal overlap in the BBO by observing the generated sum frequency wave, which is visible to the naked eye. Typically, the angle between the pump and the probe beams measure several degrees such that the sum frequency is located between the two transmitted beams due to the conservation of momentum.

5 Highly Stratified Gold-Nanoparticle Layers in Polyelectrolyte Matrices and Their Optical Characteristics

The unique and prominent properties of inorganic nanoparticles, originating from their mesoscopic size, their shape, and their interaction with the environment, reasons the large number of applications that incorporate such particles. The utilized characteristics can be of optical[2, 121, 122], electronic[121], or catalytic[13, 14, 123, 124] nature. In a considerable number of applications, the alignment of the particles plays a decisive role. Thin films, for example, are used for coatings[108], photovoltaics[103, 104] and sensors[81, 82]. Stratified nanoparticle layers were demonstrated to be required, e.g., in photonic structures[105], for surface processing[108, 109], in electronic and electrochemical devices[98, 125], and in filters[126].

Several attempts for implementing gold-nanoparticle arrays in a polyelectrolyte matrix have shown that Bragg peaks develop due to ordered multilayers[89, 127]. However, particle layers in these structures typically are separated by large spacer layers (>100 nm). As it is shown in this chapter (section: 5.1.3), polyelectrolyte surfaces become smoother with an increasing number of deposited layers. Therefore, it is straightforward to produce stratified layers with large-scale separation. However, decreasing the thickness of these spacer layers down to the particle diameter and maintaining the level of stratification at the same time is challenging. One of the few papers that report on such perfectly ordered, Bragg reflecting structures with ultra-thin spacers describes CdTe particles in phospholipids[86]. However, this structure lacks the potential of having tunable spacer thicknesses. 2-nm CdS particles incorporated in polyelectrolytes[71] showed pronounced Bragg peaks for spacer layers greater than 7.1 nm; however, these reflections almost vanished for spacer thicknesses around 2.6 nm.

The first section of this chapter presents the characterization and comparison of highly stratified multilayer structures with well-defined interparticle spacings that were assembled by the dip- and spin-coating LBL method, as described in section 3.3. Polyelectrolyte layers with a thickness comparable to the particle diameter have proven to be sufficient to separate particles of adjacent layers. The applied characterization methods, which include XRR and AFM, deliver information on the amount of particles in the structure (volume filling factor f), the layer thickness of the repetition unit and of the entire sample, the interparticle distance in the plane, and the surface roughness.

The second section presents precise studies on the optical characteristics of a se-

ries of spin-coated samples by analyzing absorption spectra determined from the measured reflectance and transmittance. In particular, the absorbance is investigated with respect to the maximum position and the integrated intensity of the localized surface plasmon resonance (LSPR) as a function of the polyelectrolyte cover layer thickness. This effect of changing the embedding medium of the nanoparticles in order to alter the composites' optical characteristics has been observed frequently and was exploited for tuning the spectral peak position of the LSPR and its absolute absorbance.[21] R. Ruppin, in 1986, theoretically predicted the dependence of a copper colloid-hybrid material on the refractive index of the surrounding medium.[128] In 1989, A. E. Neeves et al. calculated the enhancement of surface plasmon resonances by adding a cladding layer to the nanoparticles of different materials in suspension[129] and repeatedly a shift in the LSPR due to a dielectric substrate[130, 131] was experimentally observed. However, the range of interaction of the nanoparticles with their environment remained unknown. Here, this distance is experimentally determined for particles of 10 nm, 20 nm, and 150 nm. The results are discussed in terms of effective medium theories and with regard to the applicability of Kramers-Kronig relations.

This section furthermore includes studies on the interaction of neighboring particles within one layering plane and of two adjacent particle planes. Finally, a multilayer structure is analyzed with respect to a possible optical anisotropy and its static dielectric function is determined from $R(\omega)$ and $T(\omega)$ measurements.

5.1 Sample Structure

5.1.1 Layering Investigation

Results In this section, the evaluation and comparison of the X-ray reflectivity results of dip- and spin-coated samples which exhibit the layering sequence $[(\text{PSS}/\text{PAH})_x + (\text{Au-NP}/\text{PAH})]_n$ are presented. Both samples consist of $n = 4$ repetition units, whereas one repetition unit is defined as one layer of gold nanoparticles on several PSS/PAH double layers (DL). These polyelectrolyte layers act as spacers to the individual particle planes and are composed of either $x = 10$ (dip-coated) or $x = 8$ (spin-coated) DL. The following measurement results of spin-coated samples on mica substrates and the corresponding analysis are published in [132].

The samples were investigated according to the setup described in section 3.4.2. Figure 5.1 shows the experimentally derived X-ray intensity reflectivities (open circles) of the two samples for θ -angles ranging from 0.01° to 1° . Plot (a) is a scan of the dip-coated sample on soda-lime glass. Total reflection here occurs below 0.19° . The scan shows four Bragg peaks, whereof the first two peaks are pronounced but the third one is almost completely suppressed. These peaks are separated by about 0.17° , and the first Bragg reflection shows a peak reflectance of about 0.39. Pronounced Kiessig fringes exist throughout the measured angular range. Figure 5.1 (b)

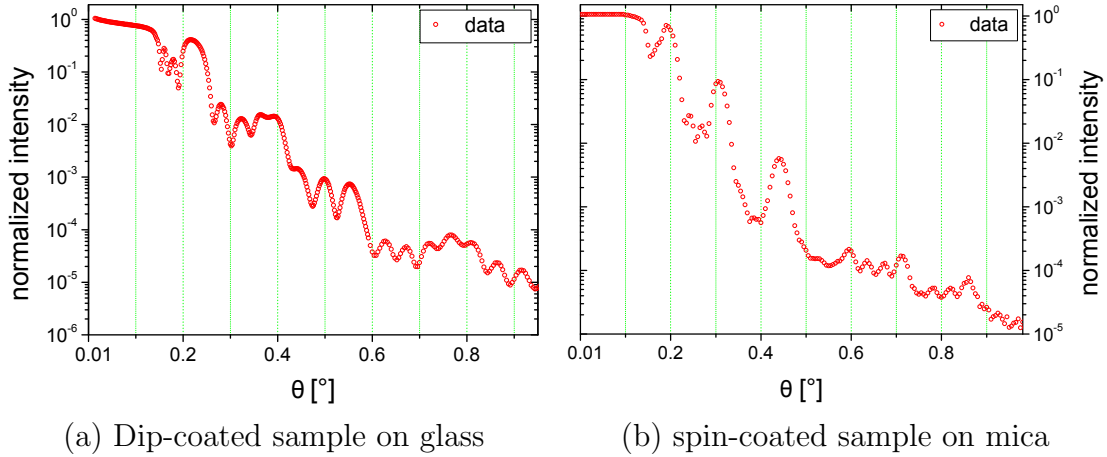


Figure 5.1: X-ray reflectivity results of a dip-coated sample on glass (a) and of a spin-coated sample on mica (b). Both structures exhibit the layering sequence $[(\text{PSS}/\text{PAH})_n + (\text{Au-NP}/\text{PAH})]_4$, where n measures 10 for the dip-coated structure and 8 for the spin coated one.

is the result of X-ray reflectivity measurements of the spin-coated sample on mica. Here, Bragg peaks up to the seventh order were detected, though only six of them are visible because the first one is hidden in the total external reflection that takes place for angles $\theta < 0.16^\circ$. These peaks are more pronounced, apart from the peaks at 0.61° and 0.74° which are strongly suppressed. The separation here measures 0.12° only. The Kiessig fringes which are hardly visible at angles below the second Bragg peak and between peaks 4 and 5 become more pronounced at larger angles.

The following section presents simulations of the X-ray intensity reflectivity, which are carried out by applying Parratts recursive formalism.[133] Therefore, one estimates a characteristic electron density distribution describing the multilayer structure from which the corresponding X-ray intensity reflectivity is calculated. This density distribution allows one to directly derive information on the structure regarding the layer thicknesses and interface morphology. The precision of this information is given by the congruence of the theoretical reflectivity with the experimental one. The X-ray intensity reflectance is basically calculated by using the Fresnel equations for X-rays. The formalism described in the following was adopted from Als-Nielsen et al.[134]. First, the complex refractive index $n \equiv 1 - \delta + i\beta$ of each layer (four polyelectrolyte and four nanoparticle layers) is expressed in terms of the respective electron density by

$$\delta_j = \frac{2\pi\rho_a f^0(0)r_0}{k^2} \quad \text{and} \quad \beta_j = \frac{\mu}{2\pi}, \quad (5.1)$$

with ρ_a being the atomic number density, f^0 being the atomic scattering factor, and r_0 , the scattering amplitude per electron. k represents the X-ray wavevector and

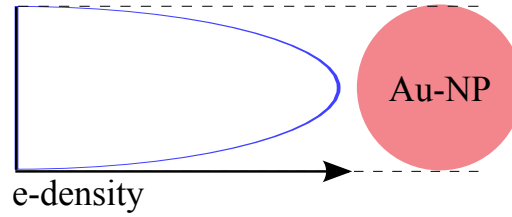


Figure 5.2: Parabolic electronic density distribution of a spherical nanoparticle

μ the absorption coefficient. The corresponding scattering wavevector Q_j for the individual layers is then determined from the fundamental relationship $Q_j = 2k_{z,j}$ and it reads as

$$Q_j = \sqrt{Q^2 - 8k^2\delta_j + i8k^2\beta_j}. \quad (5.2)$$

The reflectance of a single interface (here of layer j and $j+a$) is given by the formula

$$r'_{j,j+1} = \frac{Q_j - Q_{j+1}}{Q_j + Q_{j+1}}. \quad (5.3)$$

The reflectivity of the same layer including multiple scattering effects and refraction is calculated by taking into account the reflection of the interface underneath, under consideration of the phase ϕ :

$$r_{j,j+1} = \frac{r'_{j,j+1} + r'_{j+1,j+2} \cdot \phi_{j+1}^2}{1 + r'_{j,j+1} \cdot r'_{j+1,j+2} \cdot \phi_{j+1}^2}. \quad (5.4)$$

The final reflectance from the surface layer ($r_{0,1}$) is determined by successively calculating the reflectance of each layer starting with the lowermost one and ending with an expression for $r_{0,1}$.

So far, only structures with perfectly sharp interfaces were considered, which are represented by discontinuous electron distributions with a rectangular profile. Our structures, however, exhibit graded interfaces since gold nanoparticles and gold-nanoparticle layers inherently possess a parabolic electron density distribution as visualized in figure 5.2. Als-Nielsen et al. expanded Parratts formalism to account for graded interfaces by simply dividing each layer j into finitely small sublayers with a continuously varying electron density, as shown in figure 5.3.[134] A slight disorder of the particles and a non-monodisperse size distribution were accounted for by convoluting the distribution with a Gaussian function. Figure 5.4 shows the simulations along with the measured data from figure 5.1. It turns out that better agreement with the experimental data is achieved by assuming an electron density which is partly statistically Gauss smeared and partly ideally parabolic. This essentially indicates that the situation is not purely described by a perfect layering sequence with statistically distributed z -position of the gold particles. However, the

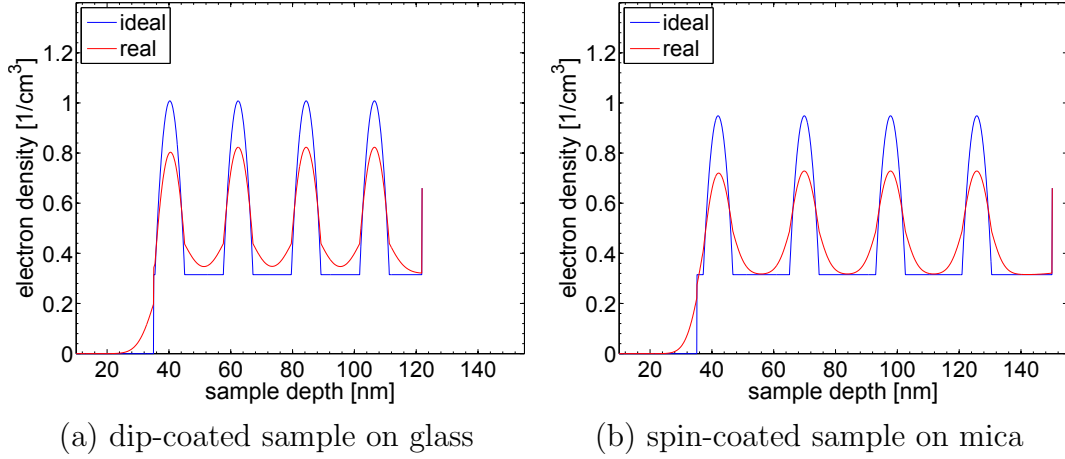


Figure 5.3: Electron density distributions along the growth direction z . The red lines represent the distributions that were assumed to simulate the reflectances according to the measurements shown in figure 5.4. The blue lines represent the ideal electronic density distribution of perfectly aligned nanoparticle layers which inherently exhibit a parabolic profile.

agreement achieved is very good (Figure 5.4). The FWHM of the Gaussian function is related to the displacement of particles relative to the ideal layering plane. Applying this formalism, one ends up with the following input parameters: thickness of the repetition unit (d_{ru}) and the overall structure (D), particle size ($2 \cdot r$), FWHM of the Gauss function, ratio of parabolic to Gauss smeared electron density distribution (PGratio).

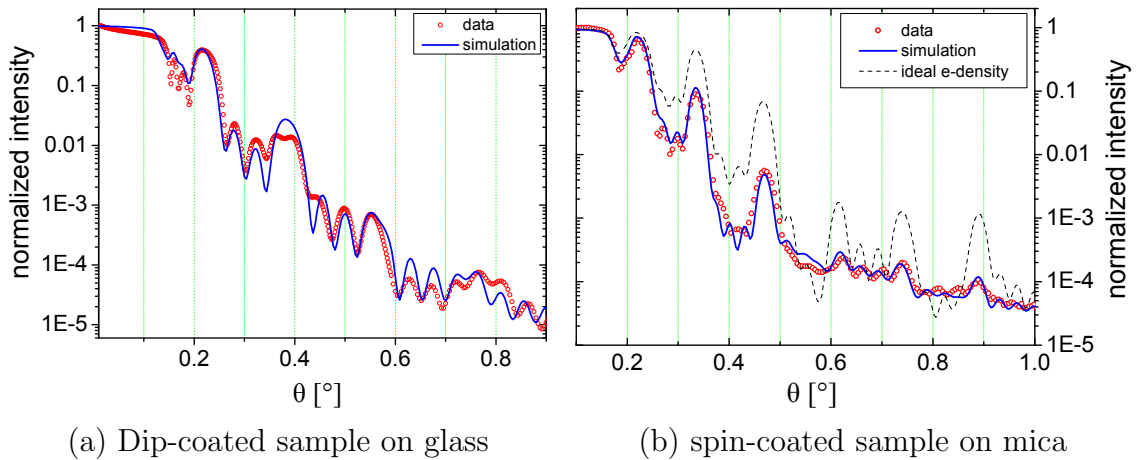


Figure 5.4: X-ray reflectivity data (red circles) and simulations (blue lines). The black dashed line represents the ideal X-ray reflectivity that belongs to the ideal electron distribution in figure 5.3.

sample	d_{ru}	d_{Au}	D	$2 \cdot r$	FWHM	PGratio	f
dip-coated	22	9.3	88	9.6	120	60	0.034
spin-coated	34	8.8	120	9.6	85	70	0.025

Table 5.1: Results of XRR measurements. Used abbreviations: d_{ru} = repetition unit thickness, d_{Au} = Au-nanoparticle layer thickness, D = total sample thickness, $2 \cdot r$ = nanoparticle diameter, FWHM = width of Gauss smearing curve, PGratio = ratio of parabolic to Gauss smeared structure, and f = volume filling factor of gold. All entries have the unit [nm] except PGratio, which is unitless

Table 5.1 summarizes the values derived from the best fits that are plotted along the experimental data in figure 5.4. Additionally, the table includes the volume filling factor f of gold nanoparticles, which was calculated from the electron density distribution and is defined as the fraction of gold volume on the overall sample volume.

Discussion The most conspicuous difference in the X-ray scan of the spin-coated sample compared to that of the dip-coated one is the existence of sharper developed Bragg peaks that are located closer together. Both features can be attributed to the fact that the spin-coated sample consists of thicker repetition units, which determine the separation of the Bragg peaks by $\Delta g \propto \frac{1}{d}$ and their width by $w \propto \frac{1}{N \cdot d}$, with N being the number of repetition units. Figure 5.3 shows the assumed electron density distributions that were used to fit the data together with the ones belonging to the ideally aligned particle distributions for comparison. These density distributions verify the repetition unit thickness of the dip-coated sample to measure 22 nm for one particle layer with 10 DL of polyelectrolyte, while the spin-coated sample consists of four layers of 28 nm with polyelectrolyte layers made of 8 DL. This significant deviation can be ascribed to the fact that spin-assisted deposition generally leads to thicker samples than the fabrication by dip coating.[75] Moreover, the spin-coated samples were prepared by using solutions of higher polyelectrolyte concentration and higher ionic strength. Both parameters result in an adsorption of thicker polyelectrolyte layers.

In order to compare the levels of stratification, the intensities of the Bragg peaks are evaluated since a statistical displacement of particles results in an attenuation of the peak intensities. The dashed line in figure 5.4 (b) represents the X-ray reflectivity of the ideal electron density distribution, that is, the purely parabolic ones. The displacement of the particles attenuates the Bragg Peak intensity to the measured level. For the dip-coated film, a rather large FWHM of 120 nm seemed most appropriate, however, only with an impact factor of PGratio = 60. In comparison, these best fitting values for the spin-coated sample measured 80 nm and 85 nm, respectively. Thus, the displacement is smaller but applies to a larger amount of

particles. Due to this and the larger separation between the gold-particle layers, the electron density decreases down to the pure polyelectrolyte value in the spin-coated case but not for the dip-coated one.

Another difference in the two X-ray reflectivity scans is the formation of pronounced Kiessig fringes for the dip-coated sample and rather weak ones for the spin-coated structure. Kiessig fringes result from the interference of reflections from the surface layer and the substrate interface layer. Thus, the fringe period allows one to identify the overall layer thickness and the peak intensities are a measure of the ratio of the two reflection amplitudes. The pronounced Kiessig fringes of the dip-coated sample indicate similar reflection amplitudes from the substrate-sample interface and the surface, since then the interference condition is optimally fulfilled. A reduced amplitude as for the spin-coated sample could have two reasons. Either, this means a much better surface roughness of the surface layer than the interface layer, or the interface at the mica-sample interface of the spin-coated sample exhibits a smaller gradient in the electron density distribution compared to the substrate-sample interface of the dip-coated sample on glass. Consequently, the mica-sample interface reflects less and the interference effect is reduced.

It is concluded that in consideration of the fact that for both structures the polyelectrolyte spacer layers were assumed to be of identical thickness throughout each sample, the simulations fit remarkably well. Especially during the dip-coating procedure, changes due to long preparation times and concentration changes in applied solutions can result in deviating layer thicknesses. The poorer quality of the fit to the dip-coated sample can be ascribed to this effect. It is worth mentioning that the investigated area of both samples measured about 10 mm². This is rather large and all measured data are an average over this area. Hence, the local layering can be assumed to be even more perfect.

5.1.2 In-Plane Particle Distribution

From the X-ray reflectivity measurements, it was possible to derive the average electron density which allowed to determine the nanoparticle volume filling factor $f = 3.4\%$. This value corresponds to an in-plane particle density of 19.5 particles per 100 nm². In order to cross-check this number, a high-resolution AFM measurement [Figure 5.5 (a)] of an equivalent spin-coated sample was performed. By simply counting the particles in the scanned area of 410 nm², a density of 17.8 particles per 100 nm² was identified, which corresponds to a lateral packing density of 15.4%. Since the maximum packing density of particles in a plane amounts to 90.7%, this corresponds to a situation, where every 7th place is occupied by a particle, as indicated in figure 5.5 (c). These volume filling factors are required parameters in the calculation of absorption spectra for compound structures by means of the Maxwell-Garnett effective medium theory.

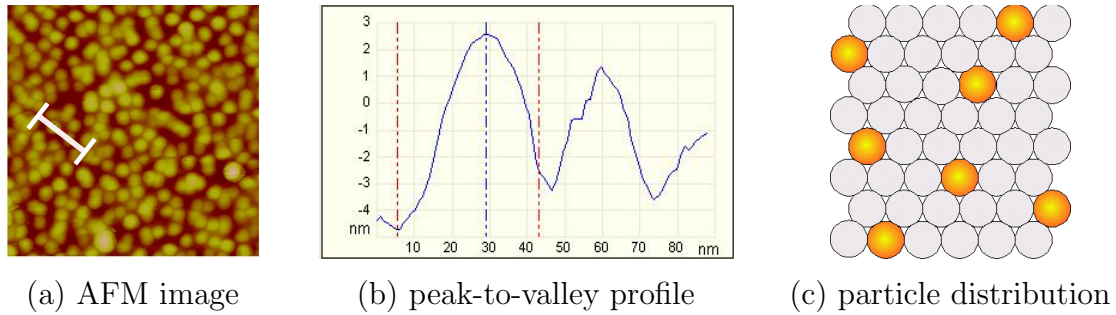


Figure 5.5: (a) AFM picture of a gold-particle layer on 8 DL PAH/PSS and (b) peak-to-valley modulation of two spheres measured along the white bar in (a). The cartoon in (c) visualizes the lateral particle distribution which corresponds to the volume filling factor of $f = 0.034$ as measured for the dip-coated sample.

5.1.3 Surface and Interface Roughness

In this section, the surface roughness of a spin-coated sample is investigated by using an AFM. Therefore, a gold-nanoparticle layer is deposited on 8 DL PSS/PAH on a mica substrate and the surface topography is measured after each PAH/PSS DL deposition. The resulting plot presented in figure 5.6 (a) clearly shows the decreasing surface roughness upon polyelectrolyte covering. From the initial 1.8 nm, the RMS roughness decreases to 1.1 nm. This initial roughness of the bare nanoparticle layer is not necessarily due to a misalignment of the particles, since also perfectly arranged particles show a peak-to-valley modulation of 5 nm due to the particles being half embedded and half sticking out. This situation, which is visualized in figure 5.5 (b), corresponds to an RMS roughness of 0.76. The value of 1.8, however, is somewhat larger so that parts of the roughness must be assigned to other origins, such as delocalization of particles.

In section 5.1.1, the disorder was taken into account by convoluting the estimated electron density distribution with a Gauss function (FWHM = 8.4 nm). However, the measured results from X-ray experiments always represent average values over the investigated area, and since this area of 10 mm² is rather large, the results and thus the Gauss FWHM of 8.4 comprise influences of the sample flatness and the global roughness. Thus, XRR inherently leads to higher roughnesses compared to the RMS roughnesses from AFM measurements, which in contrast correspond to a scanned area of 410 nm × 410 nm only and hence is a measure of the local topography. The transmission electron microscopy (TEM) image shown in figure 5.6 (b) for a dip-coated sample with eight repetition units again demonstrates the remarkable stratification of the particle layers. This image also visualizes that by the deposition of polyelectrolyte layers, the roughness can be reduced and structural defects are smoothed out to a large extent. Such self-healing properties facilitate

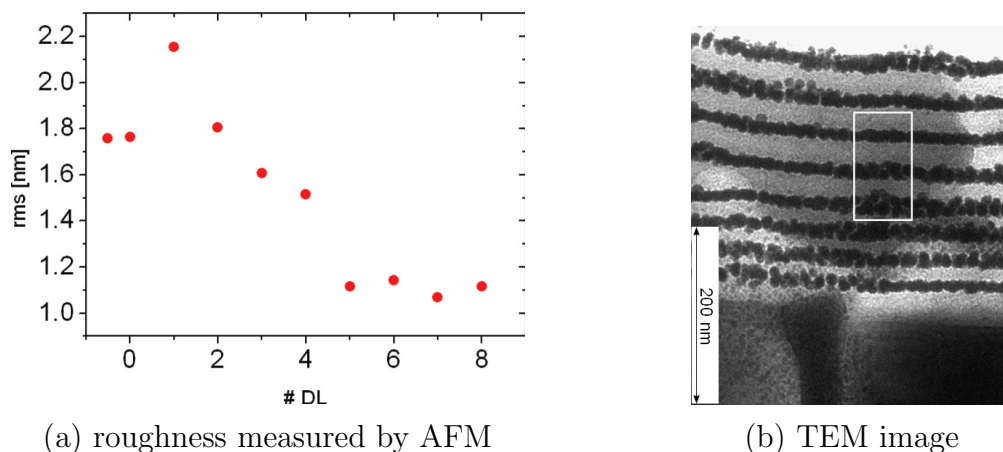


Figure 5.6: (a) AFM surface roughness results (RMS values) as a function of the number of double layers (# DL) which are deposited on the surface of a gold-nanoparticle layer. (b) TEM picture of a dip-coated sample on glass with 8 repetition units. This picture nicely visualizes the smoothing of layers with deposition of polyelectrolytes (see box).

the preparation of stratified multilayer particle films. It is furthermore verified from the TEM image that the local roughness can be much smaller than the global one measured by XRR. However, this method was not implemented as a standard investigation technique because slicing of the samples into ultrathin layers in almost all cases resulted in the destruction of the structures.

5.2 Optical Characterization by Steady-State Spectroscopy

This section presents optical reflection and transmission measurements from which precise absorption spectra are determined. The investigated samples are prepared using the spin-coating technique for time efficiency reasons. First, samples comprising only a single nanoparticle layer are studied in order to avoid possible interaction of the neighboring particle layers. The absorption spectra are analyzed with respect to the particle concentration and the covering layer thickness for particles with diameters of 10 nm, 20 nm, and 150 nm. The results are discussed in terms of Kramers-Kronig consistency. Subsequently, the interaction of two particle layers is investigated. These studies were published in *Langmuir* in 2012.[135] Finally, a multilayer structure is tested for a possible birefringence and its static dielectric function is derived.

5.2.1 Concentration Dependence of LSPR

Results Figure 5.7 shows the results from spectrophotometric measurements of samples with 10-nm particles and a layering sequence $[(\text{PSS}/\text{PAH})_8 + (\text{Au-NP}_C/\text{PAH})]_4$. The index C denotes different particle concentrations which are obtained by either using diluted gold-nanoparticle solutions or by varying the adsorption time. The reflectance and transmittance spectra were recorded according to the setup described in 3.4.1 using an integrating sphere. Hence, both spectra comprise specular and diffuse scattering components. Panels (a) and (b) present these reflectance R_{sd} and transmittance T_{sd} spectra, respectively. The reflectance spectra in panel (a) clearly reveal an increase in reflected intensity with rising concentration. At the highest particle density, which corresponds to an adsorption time of 200 min using a 50% diluted solution, the reflectance spectrum additionally exhibits strong components in the red spectral region (~ 620 nm), suggesting the rising of a second maximum. The corresponding absorbances show a similar behavior with higher particle densities. Along with the significant increase in integrated intensity, one also observes a shift in the maximum peak position. The vertical dashed line in figure 5.7 (d) indicates the maximum peak position for diluted particle solutions and adsorption times up to 60 min. At longer adsorption times, the plasmon resonance maximum shifts to the red. At the highest plotted particle density (magenta line), stronger components in the red spectral region become apparent again.

Panel (c) represents the sum of the diffuse scattering contributions for two representative curves in reflection and transmission geometries, which is in the order of 10^{-3} throughout the visible spectrum.

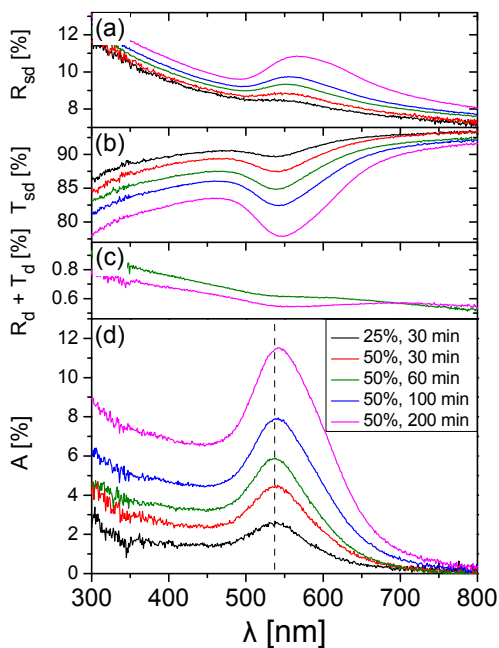


Figure 5.7:

Measured reflectance (a) and transmittance (b) spectra of structures with 10 nm particles. (c) shows diffuse scattering contributions of two samples and (d) is the absorption determined by $A = 1 - R_{sd} - T_{sd}$. The blue- and magenta-colored lines clearly show a slight red shift and higher absorption intensities in the red spectral region. Both effects indicate a clustering of particles.

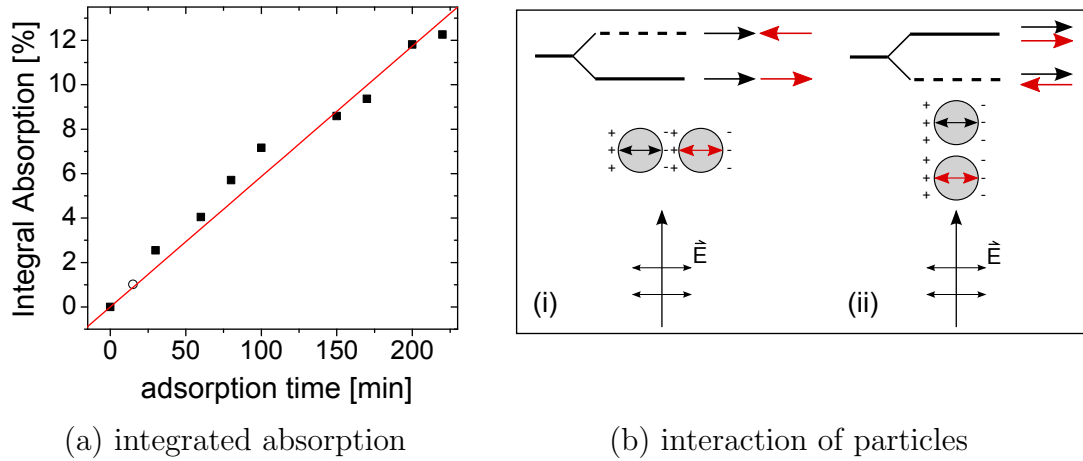


Figure 5.8: (a) Integral absorption of the plasmon resonance as a function of the adsorption time. (b) Cartoon of the energy splitting process of two interacting nanoparticles.[136]

Discussion The integrated absorption $A_I(n) = \int A(\lambda, n) d\lambda$ for wavelengths ranging from 480 nm to 680 nm is plotted as a function of the adsorption time in figure 5.8 (a). The effect that the aggregation of particles leads to an increase in intensity in the red spectral region, as visible in the magenta-colored spectra (200 min) in figure 5.7, is explained in the following.

The cartoon in figure 5.8 (b) demonstrates two coagulated particles that are investigated using light having a polarization parallel (i) and perpendicular (ii) to the particle pair axis. The induced transition dipoles are either in-line (i) or parallel (ii) to each other. The given situation here corresponds to case (i), because the particles lie within one layering plane and are investigated using light at normal incidence. The electric field vector is thus always parallel to the particle pair axis and induces in-line transition dipoles. The coagulation of particles causes the electromagnetic coupling of the dipolar particle oscillators. This coupling leads to a splitting of the transition energy due to either repulsive or attractive electrostatic forces that act on the dipoles. These electrostatic forces result from surface charges on the nanoparticles, as indicated in the cartoon. In case (i) the in-phase state results in an attraction of the dipoles such that the transition energy is decreased. On the contrary, the out-of-phase state yields a higher transition energy due to the repulsive interaction. In case (ii) it is the other way around. That is, the in-phase state causes repulsive forces and yields higher transition energies, while the out-of-phase dipoles lead to a lowering. Since the transition moment is determined by the vector sum of the individual dipole moments, the net transition moment of the out-of-phase arrangements is zero so that the complete oscillator strength is stored in the in-phase states only.[21, 136] Thus, the arrangement (i) which describes the present situation results in a red shift (lowering) and situation (ii) in a blue shift (increase).

If the distance of the two particles decreases to a minimum, a second maximum can be observed, rather than a shift, as indicated by the measurement results in figure

5.7 for a 200 min adsorption time.

In order to analyze well-defined samples, all structures in the following are prepared with an adsorption time of 60 min and 50% diluted solutions in order to inhibit the coagulation of particles. The resulting samples exhibit well-pronounced absorption bands due to dipolar plasmon resonances of single 10-nm particles only.

In conclusion, this measurement series clearly evidences the importance of considering the reflectance in order to determine absorption spectra. It is not sufficient to measure transmittances only. At 800 nm, for example, the transmission of 90% is mainly due to losses from reflection rather than absorption. Diffuse scattering contributes only little for 10-nm particles but becomes more relevant for particles with a diameter of 150 nm.

5.2.2 Peak Position and Integrated Intensity as Functions of the Polyelectrolyte Cover Layer Thickness

This section presents measurements of the surface plasmon resonance of one particle layer that is covered with polyelectrolyte layers of different thicknesses. Therefore, a series of samples with a layering sequence

$[(\text{PSS}/\text{PAH})_8+(\text{Au-NP})+(\text{PAH}/\text{PSS})_n]$ is investigated. These multilayers are deposited on fused silica glass which was coated with PEI/PAH before.

Results Figure 5.9 (a), (c), and (e) presents measured reflectances R_{sd} , transmittances T_{sd} , and the corresponding absorbance spectra for samples with cover layers varying from 0 to 14.5 DL of PAH/PSS. Zero DL corresponds to a bare particle layer without any cover layer and decimal numbers with x.5 indicate that the top layer is PAH. The plotted spectra clearly show that the absorption saturates for more than 4.5 DL, while the reflectance and transmittance spectra keep changing with further deposition of polyelectrolytes. A shift in the maximum or minimum position of the LSPR can be observed in the absorbance and transmittance spectra, respectively. The alteration of the reflectance upon polyelectrolyte covering is analyzed by evaluating the spectral position of the steepest slope (point of inversion). This feature constantly moves to the red with deposition of polyelectrolytes.

Panels (b), (d), and (f) display spectra for covering layers that consist of 20, 25, 30, or 35 DL and spectra corresponding to DL = 0 and DL = 14 for comparison. Strong shifts and modifications of the spectral shape can be observed for the reflectance throughout the covering process. In contrast, the absorbance spectra saturate with respect to the integrated intensity and peak position. Figure 5.9 shows results for a 10-nm particle layer only. However, experiments have been performed with samples that incorporate 20-nm and 150-nm particles. Particles with 150-nm diameter differ from the smaller particles by larger diffuse scattering contributions.

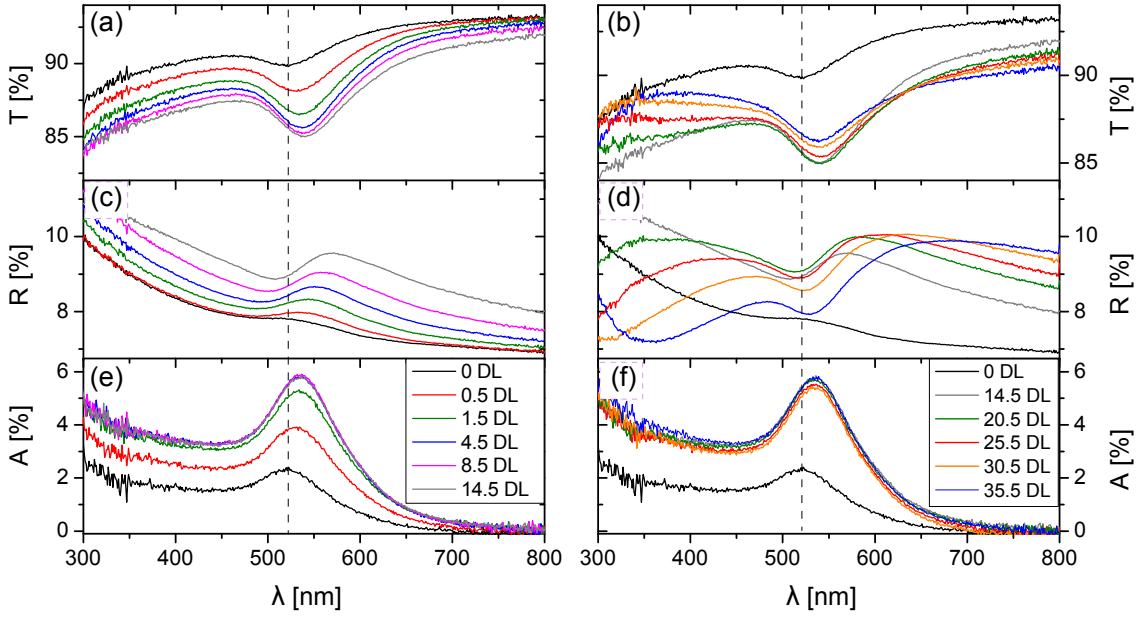


Figure 5.9: (a) and (b) Transmission and (c) and (d) reflection spectra as functions of the cover layer thickness $D_{DL} = 2.5 \cdot DL$ on a 10-nm gold-nanoparticle layer. The spectra were measured at normal incidence for 10-nm gold particles on 8 DL PSS/PAH with an in-plane particle density of $1900 \mu\text{m}^{-2}$. (e) and (f) present the corresponding absorption spectra.

Discussion Once the cover layer thickness exceeds the plasmon interaction range, the absorbance is saturated and no alteration occurs upon the deposition of additional transparent polyelectrolytes. The changes in transmittance for thicker layers are hence caused by the modified reflectance only. A quantification of this saturation is given in the following by the calculation of the integral absorption and the peak position. In order to obtain results with high precision, it is necessary to account for the interband absorption band which overlaps spectrally with the LSPR causing the asymmetric shape of the resonance feature. Therefore, an offset that qualitatively conforms to the imaginary part of bulk gold is subtracted from each spectrum, resulting in a symmetric surface plasmon resonance. The integrated intensity is directly calculated from this spectra by $A_I(n) = \int A(\lambda, n) d\lambda$ for wavelengths ranging from 480 nm to 750 nm. In order to determine the peak position, a Gauss function is fitted to the resonance. Its center defines the maximum of the plasmon resonance. The results are plotted in figure 5.10 for 10-nm, 20-nm and 150-nm particles. The integrated absorption in panel (b) clearly saturates and thus allows one to quantitatively determine the plasmon interaction range for each particle size. The peak position shown in panel (a) continues to shift beyond this interaction distance for all particle sizes.

The origin of the observed plasmon resonance shift is discussed in the following by means of equation 2.6, from which the position of the plasmon is determined by the resonance condition: $\epsilon_{Au} = -2\epsilon_m$. First, the situation of the bare particle without

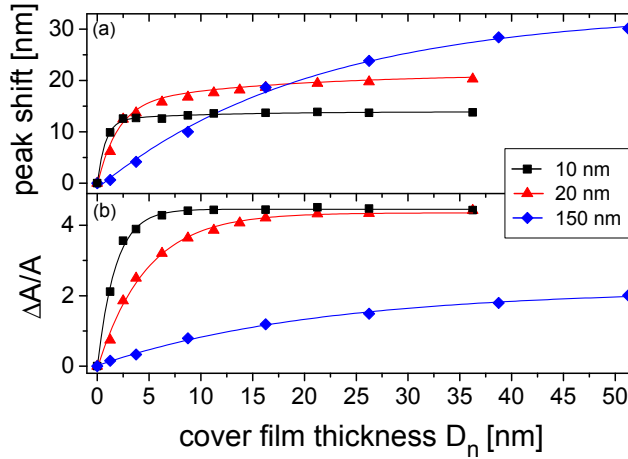


Figure 5.10: Peak shift (a) and integral absorption change (b) as functions of the cover layer thickness D_n on a single nanoparticle layer with 10-nm (black), 20-nm (red), and 150-nm (blue) particles. The symbols represent measured data, while the solid lines are double-exponential fits.

any polyelectrolyte covering is considered. These particles are half embedded in the polyelectrolyte buffer layer and half exposed to the ambient air. Therefore, they are surrounded by a dielectric medium with an average dielectric constant of about $\epsilon_m = (\epsilon_{pol} + \epsilon_{air})/2 \approx 1.95$. With each polyelectrolyte DL that is deposited, this average dielectric constant increases up to the pure polymer dielectric constant of about 2.46. This situation corresponds to a sample where the cover layer thickness D_n exceeds the LSPR interaction range. With this alteration of the embedding medium, also the resonance condition $\epsilon_{Au} = -2 \cdot \epsilon_m$ is modified. Figure 5.11 visualizes the resonance condition for the two situations:

$$-2\epsilon_m = \text{Re}(\epsilon_{Au}) = -3.9 \text{ (magenta circles for half-embedded particles) and}$$

$$-2\epsilon_m = \text{Re}(\epsilon_{Au}) = -4.9 \text{ (blue circles for fully embedded particles).}$$

The resonance for 10-nm gold particles therefore shifts from 525 nm to 538 nm.

The intensity increase of the LSPR can be explained as follows: Generally, the imaginary part of the dielectric function of gold determines how well the plasmon resonance is pronounced. In the visible spectrum, the imaginary part of gold exhibits resonances due to interband transitions and hence shows a pronounced wavelength dependence, as plotted in figure 5.11 (red line). When the resonance shifts to lower frequencies, the absolute value of the imaginary part becomes smaller and consequently allows the resonance to increase.

The results from section 5.2.2 showing strong changes in the reflectance indicate that thin layer interference alters the optical characteristics of the investigated samples. The complex refractive index is therefore determined for each set of reflectance and transmittance spectra, analyzed with regard to the cover layer thickness, and is subsequently checked for Kramers-Kronig consistency. To do so, the sample is modeled as a single effective medium layer with the complex index of refraction $\tilde{n}_{eff} = n_{eff} + i \cdot \kappa_{eff}$ on a substrate. The imaginary part of the refractive index $\kappa(\lambda)$

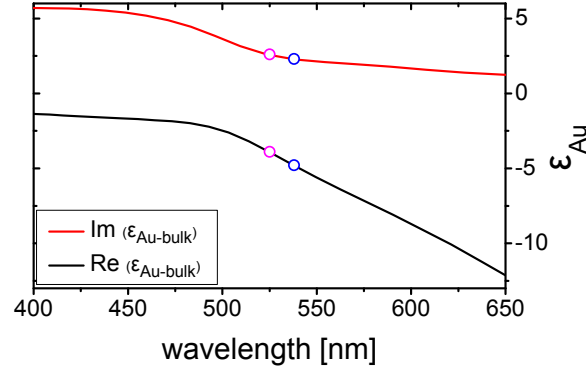


Figure 5.11: Real (black) and imaginary (red) parts of the dielectric function of bulk gold from Johnson and Christy[26]. For half-embedded particles the resonance condition is fulfilled at 525 nm (magenta circles). The red-shifted resonance (blue circles) belongs to the situation where the particles are fully covered with PAH/PSS (538 nm).

is calculated from the absorption spectra plotted in figure 5.9 (e) and (f) by

$$\kappa(\lambda) = \frac{\lambda}{4\pi} \alpha(\lambda) = -\frac{\lambda}{4\pi} \cdot \frac{\ln[1 - A(\lambda)]}{D_b + D_n} \quad (5.5)$$

and is plotted in figure 5.12 (a). The real part of the refractive index $n(\lambda)$ is determined twice: once by fitting the reflectance R , calculated from the Fresnel formulas, to the measured specular reflectance and once by fitting the transmittance T , calculated from the Fresnel formulas, to the measured specular transmittance. The resulting curves qualitatively conform with each other, though they differ by an offset. Their average value is plotted in figure 5.12 (b) and the deviation of the two fit procedures is indicated by the error bar. Panel (a) shows that the maximum of the imaginary part (κ) significantly rises upon adsorption of the first 2 DL of the polyelectrolyte. Simultaneously, a red shift is observed. Further deposition however leads to a drastic decay from 0.1 down to ~ 0.02 for a covering layer thickness of $35 \cdot 2.5 \text{ nm} = 87.5 \text{ nm}$. The real part (n) changes its characteristic shape during the deposition of the first 2.5 DL. Further adsorption leads to a decrease and immense red shift of about 50 nm determined for the spectral position with the steepest positive slope.

The fact that κ decreases upon polyelectrolyte covering while the adsorption saturates is due to the decreasing fraction of gold inside the sample as the cover layer thickness grows. The particles are basically diluted in the embedding medium, resulting in the lowering of the absorption coefficient and thus in the lowering of κ . This is also shown in equation 5.5, which comprises the division by the total layer thickness $D_b + D_n$. Consequently, the imaginary part of the effective medium κ_{eff} shown in 5.12 (a) decreases for thick covering layers.

Another important observation is that the shift of about 12 nm of the maximum

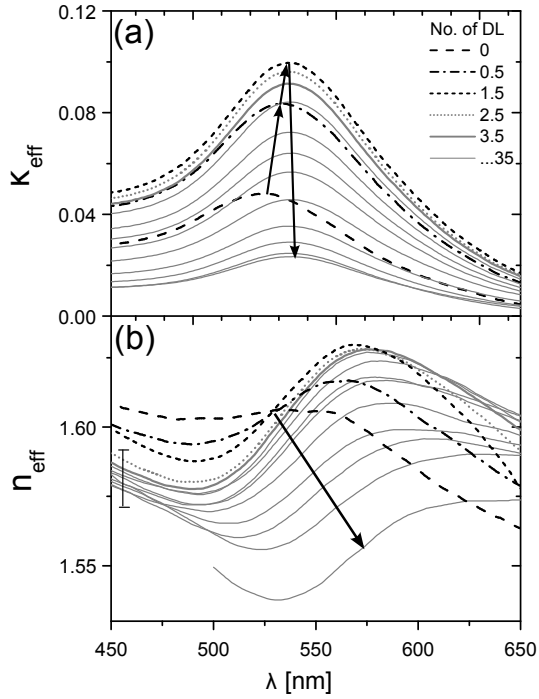


Figure 5.12:

(a) presents the imaginary part κ and (b) the real part n of the refractive index of the effective medium plotted as functions of the cover layer thickness D_n . (a) clearly shows an increase in the imaginary part for a cover layer thickness up to 1.5 DL. Further deposition leads to a significant decrease. While the red shift of the imaginary part saturates after 10 nm, the real part (b) keeps changing its spectral position throughout the deposition process.

position of κ_{eff} strongly differs from the 50-nm red shift of the spectral feature of n_{eff} . This means that Kramers-Kronig relations are no longer fulfilled. In order to describe a sample with an effective dielectric function that is Kramers-Kronig consistent, the cover layer thickness must not exceed the plasmon-interaction range. Figure 5.12 indicates that a sample with a cover layer thickness of 8 DL still satisfies these conditions. For thicker covering layers, it is necessary to treat the sample as a multilayer structure made of infinitesimal small layers with a gradually changing dielectric function. Only then, it is possible to derive physically reasonable values of n_{eff} and κ_{eff} .

5.2.3 Two Interacting Particle Layers

So far, the interaction of particles within one layer was investigated as a function of the concentration and of the embedding medium. The obtained information allows the fabrication of well-defined structures by avoiding aggregation of particles (60 min absorption time and 50% diluted colloid solution) and by eliminating the influence of the substrate and the ambient air (buffer and cover layer thickness exceeds the range of plasmonic interaction). In this section, samples with two particle layers are investigated. These particle layers are separated by m DL of PAH/PSS, resulting in the following layering sequence:

$[(PSS/PAH)_8 + Au-NP + (PAH/PSS)_m + PAH + Au-NP + (PAH/PSS)_8]$. Intermediate measurements of the spectral absorption allows for observing changes in the peak position upon particle adsorption and subsequent polyelectrolyte deposition. This peak position is studied as a function of the separating spacer layer thickness that is given by $D_{Au-Au} = m \cdot D_{DL}$.

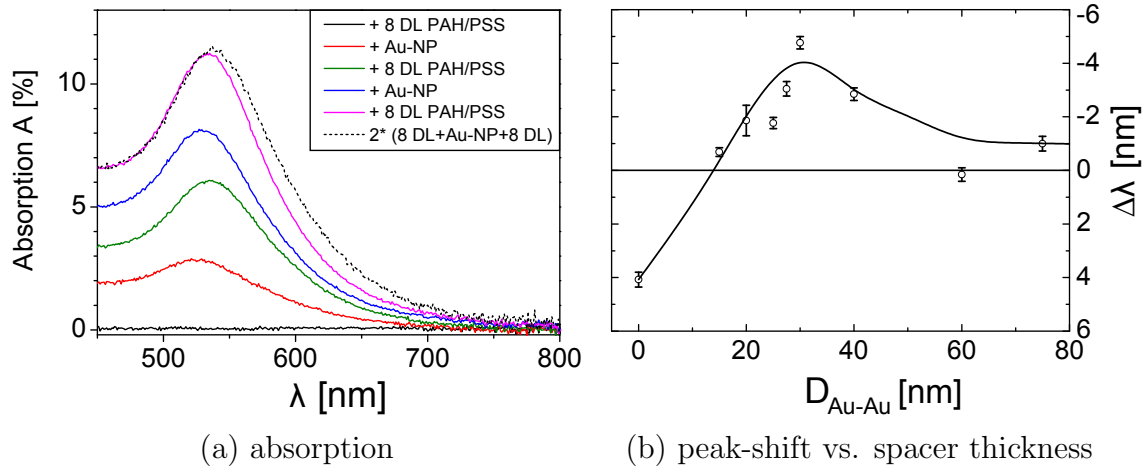


Figure 5.13: (a) presents the absorption spectra of a compound structure with two particle layers. The spectra were measured at intermediate states during the deposition process. (b) shows the shift in the plasmon resonance as a function of the separation of the two particle layers.

Results The magenta colored line in figure 5.13 (a) describes the absorption spectrum for a sample with two particle layers and $m = 16$ DL of separation. The two lowermost spectra represent the pure polyelectrolyte buffer layer and the deposited first particle layer. The subsequent adsorption of $m/2 = 8$ DL of PAH/PSS shifts the plasmon resonance to the red and increases the integrated intensity significantly by a factor of about 4 (green line), which conforms with earlier experiments. The deposition of the second gold layer moves the plasmon maximum to the blue by about 6 nm (blue line). This is expected as half of the particles in the structure are not covered by polyelectrolyte but see the ambient air and thus possess a blue-shifted plasmon resonance which effectively shifts the measured resonance to the blue. The final cover layer of 8 DL PAH/PSS on the top shifts it back to the red, although less than that for a single particle layer with identical cover layer thickness. The spectrum of such a single particle layer is multiplied by a factor of 2 and plotted along the other spectra as one could expect this spectrum to conform with the two-particle layer system. In fact, the plasmon absorption of the two particle layer system is blue-shifted with respect to the one particle layer structure. The difference in the peak positions of double particle layer structures and the reference single particle layer samples with cover layers of 8 DL is plotted in figure 5.13 (b).

Discussion The origin of the observed blue shift has been discussed before in terms of a coupled oscillator model in section 5.2.1 and is illustrated in the cartoon of figure 5.8 (b). The given situation here corresponds to case (ii), because the particle layers are investigated with light at normal incidence so that the electric field vectors are always perpendicular to the particle pair axis of the particles in neighboring layers.

As explained before, the interaction of such parallel transition dipoles results in a blue shift of the resonance maximum.

Apart from the interaction of transition dipoles, another effect may give rise to a blue shift. As explained in the previous section, a modification of the embedding medium leads to a shift in the plasmon due to the modified resonance condition. When gold nanoparticles, which exhibit a negative real dielectric function, are introduced within the interaction of a reference particle, this reference particle is effectively embedded in a medium with a low real dielectric function. Consequently, the plasmon resonance shifts to the blue. The fact that a red shift is observed for very small distances indicates a very strong dipole–dipole interaction, which effectively shifts the resonance to larger wavelengths.

5.2.4 Anisotropy of Multilayer Films

The fact that the fabricated samples do not possess a homogeneous particle distribution in the growth direction (z-direction) due to the multilayer structure, one has to consider effects of anisotropy. Therefore, all optical experiments were performed at normal incidence so far. Here, a dip-coated sample with four particle layers is tested for birefringence by analyzing the reflectance and transmittance of s- and p-polarized light at various angles of incidence. The exact layering sequence of the investigated sample is [(PAH/PSS)₁₀+(Au-NP/PAH)]₄. A helium-neon laser with an wavelength of 543 nm was used according to the measurement setup given in section 3.4.4. The reflections from the sample layer interfaces and from the backside of the substrate spatially overlap and interfere for angles α below 24° and above 78°. Intensities were therefore measured within this angular range only, where the reflections are clearly separated and the sample layer ones are only detected.

Results Figure 5.14 displays the polarization and angle-dependent transmittances and reflectances of the multilayer sample at 543 nm, showing a typical dependence on the polarization of the incoming light. The Brewster angle is located at $\alpha = 60^\circ$ determined from measurements with p-polarized light. In order to verify a possible birefringence, simulations are carried out from which the dielectric function for each polarization is identified. Therefore, it is assumed that the sample consists of one sample layer with an effective dielectric function ϵ_{eff} on a glass substrate. A convenient method for modeling reflectances and transmittances of a single or multilayer structure is based on a matrix formalism from M. V. Klein and T. E. Furtak [32] that was presented in section 2.2. Therein, matrices are derived which describe the electric fields at interfaces (H) and inside transmitting media (P) according to the Fresnel equations for anisotropic thin plates.[31] These matrices are then sequentially multiplied in the order in which the light passes through the elements they describe, as illustrated in figure 5.15. The result is a system matrix S from which the amplitude coefficients ρ and τ are calculated directly.

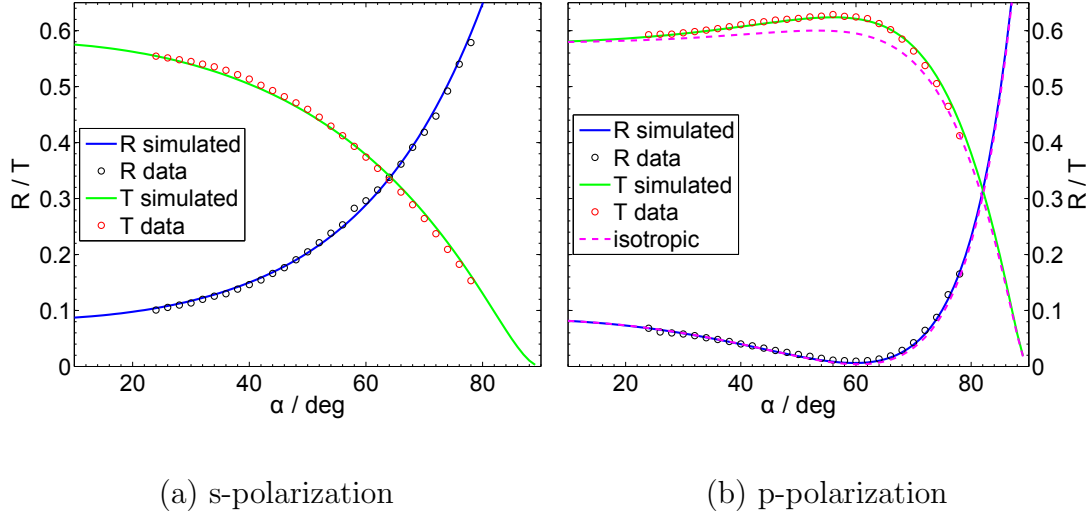


Figure 5.14: Angular-dependent transmittances and reflectances of a multilayer structure measured at 543 nm. The symbols represent experimental data, while the solid lines are simulations. Different dielectric constants were assumed for the simulations in (a) (s-polarization) and (b) (p-polarization). The magenta line in (b) was calculated with the same ϵ_{eff} as used in (a).

The reflectances $R(\alpha)$ and transmittances $T(\alpha)$ shown in figure 5.14 were derived as follows: In order to simulate a reflectance that conforms with the measurements, a system must be described which neglects the reflection from the backside of the substrate, since this was neglected in the measurement and did not interfere with the other reflections. The reflectivity was therefore calculated by assuming a single sample layer between two media (air and substrate) with refractive indices n_{air} and $n_{substrate}$ so that the rear substrate interface is neglected. In the following, the subscripts 0, 1, and 2 describe the media air, sample layer, and substrate, respectively. The system matrix for reflection (S^R) is given by the sequence

$$S^R = P^0 H^{01} P^1 H^{12}. \quad (5.6)$$

The reflectance that was used to fit the experimental data in figure 5.14 is determined by

$$R(\epsilon_{eff}) = |\rho|^2 = \left(\frac{(S^R)_{12}}{(S^R)_{22}} \right)^2. \quad (5.7)$$

In contrast to the reflectance, the simulation of the transmittance must take into account the rear interface of the substrate. According to our measurements though, the interference with the double reflected beam inside the substrate must be neglected as it is spatially separated from the directly transmitted beam. Therefore the matrix formalism cannot be applied throughout these calculations. Instead, the

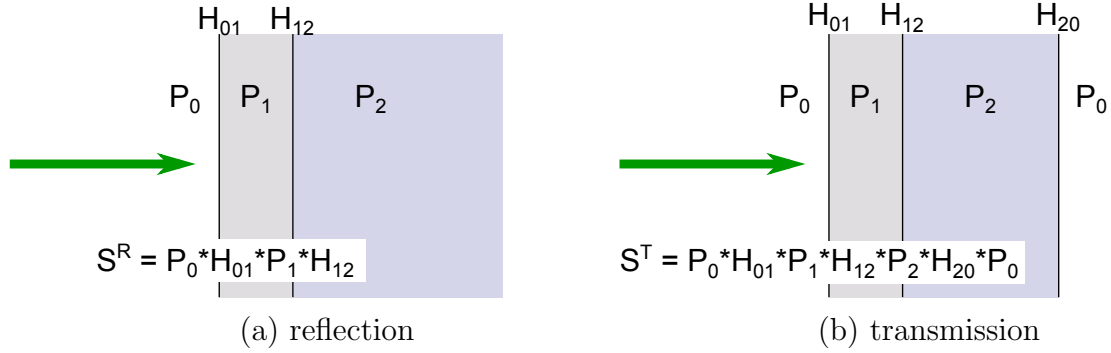


Figure 5.15: Illustration of the matrix formalism. Expressions for the system matrix S in (a) reflection and (b) transmission geometry.

intensity that is transmitted into the substrate ($S_{02}^T = H_{02}P_1H_{12}P_2$) is determined and multiplied with the transmittance of the substrate-air interface, which is described by the system matrix: $S^T = H_{20}$. Such calculations that are carried out using intensities and not the electric fields and phases do not account for interference effects. Later, the intensity contribution from the double reflected beam (T_{MR}) is added by likewise multiplication with the reflectances and transmittances. The final transmittance, which conforms with the performed experiments, is given by the following expression:

$$T(\epsilon_{eff}) = T_{02} \cdot T_{20} + T_{MR} . \quad (5.8)$$

Discussion The reflectances and transmittances plotted in figure 5.14 along with the measured data were simulated by assuming two different, polarization-dependent values for the effective dielectric functions: $\epsilon_{eff}^s = 2.65 - i0.72$ and $\epsilon_{eff}^p = 2.95 - i0.59$. The profound consistency of simulation and measurement confirms the estimated values for ϵ_{eff}^s and ϵ_{eff}^p and verifies the multilayer structure to be birefringent.

This result is not surprising as the structure is rotationally symmetric with respect to the z -axis (growth direction) and therefore is uniaxially anisotropic. For the dielectric function of such media, this means that $\epsilon(x) = \epsilon(y) \neq \epsilon(z)$. As a consequence, the structure can be regarded isotropic for s-polarized light, which has its electric field vector in the rotationally symmetric x - y plane for any angle α . Only upon investigation with light having a polarization component in the z -direction, it must be treated anisotropically, which applies to p-polarized light at angles $\alpha > 0$. The dashed, magenta-colored line in plot 5.14 (b) visualizes the deviation of the simulation with the measurement if a completely isotropic sample is assumed, that is, $\epsilon_{eff}^p = \epsilon_{eff}^s$.

It is noteworthy that the multilayered structure, which is responsible for the birefringence, was not taken into account when calculating the transmittance and reflectance. In contrast, the structure was treated as a single layer with an effective dielectric function ϵ_{eff} and two interfaces. By means of this simplification, multiple reflection effects inside the sample layers were neglected.

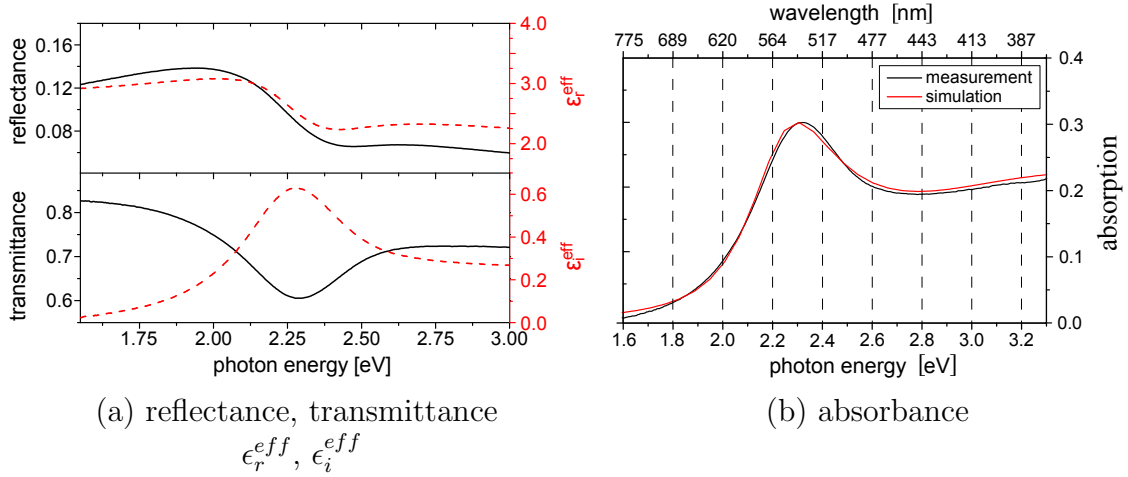


Figure 5.16: (a) Measured specular reflectance and transmittance and the real and imaginary parts of the according dielectric function at $\alpha = 0^\circ$. (b) Measured and simulated absorbance spectra. The experimental absorbance was determined by $A = 1 - T - R$, where T and R must comprise the diffuse and specular components.

5.2.5 Static Dielectric Function of Multilayer Films

The sample that is investigated in the next chapter by ultrafast pump-probe spectroscopy is analyzed according to static photospectrometric measurements. The sample is deposited on a PEI covered soda-lime glass slide and exhibits a layering sequence $[(\text{PSS}/\text{PAH})_{10} + (\text{Au-NP}/\text{PAH})_4]$. It was assured that the aggregation or interaction of particles is avoided, and the structure was characterized by X-ray reflectometry in section 5.1.1. From the according simulations, the volume filling factor $f = 0.034$ and the thicknesses of one repetition unit ($d_{r.u.} = 22$ nm) and the overall sample layer ($D = 88$ nm) were derived. In section 5.2.4, the optical properties of the structure were identified to be uniaxially anisotropic.

Spectrophotometric measurements of the sample and a reference substrate were performed independently at normal incidence using an integrating sphere according to the setup description in section 3.4.1. From the results the specular contribution of the sample layer to the transmittance ($T_0(\omega)$) and reflectance ($R_0(\omega)$) spectra was calculated without the substrate contribution and is presented in figure 5.16 (a) (black lines, left axis). The corresponding dielectric function for $\alpha = 0^\circ$, which is calculated from $R_0(\omega)$ and $T_0(\omega)$ by simply applying the inverted Fresnel formula, is plotted in the same figure (red dashed lines, right axis).

In figure 5.16 (b), the absorbance spectrum $A_0(\omega)$, derived from the diffuse and specular components of $R_0(\omega)$ and $T_0(\omega)$, is plotted along with a cross-check simulation of the absorbance. This simulation was obtained from the calculations of the effective dielectric function ϵ^{eff} using the Maxwell-Garnett formula for effective media given in equation 2.6. The input parameters f (volume filling factor) and the polyelectrolyte dielectric function were determined experimentally. The third

parameter, the dielectric function of gold, is taken from an analytical model for bulk gold from P.G. Etchegoin et al.[137] This value but was adjusted to the nanoparticle system by increasing the electron scattering rate by a factor of about 3. Such an increase is physically appropriate as electrons in nanoparticles possess a significantly higher scattering probability due to their confined size. From the effective dielectric function, the imaginary refractive index (κ) is determined by $\kappa^2 = \frac{1}{2}[\sqrt{(\epsilon_{Re}^{eff})^2 + (\epsilon_{Im}^{eff})^2} - \epsilon_{Re}^{eff}]$, yielding the absorption coefficient α via the relation $\alpha = 2\kappa\omega/c_0$. The absorption is then calculated by applying Lambert-Beers law: $A = 1 - e^{-\alpha D}$, where D is the sample layer thickness (88 nm). The profound agreement of the two curves in figure 5.16 (b) once more verifies the input parameters derived from X-ray reflectivity measurements and the adjusted scattering rate.

6 Time-Resolved Ultrafast Optical Spectroscopy

The dielectric function is the key parameter for understanding and predicting the interaction of matter with electromagnetic radiation. The implementation of nano-objects into functional materials has become a popular and attractive method to design and tune structures to have well-defined characteristics. If the embedded nano-objects are much smaller than the wavelength of the light of investigation, the structure can be treated as an effective medium with an effective dielectric function ϵ^{eff} .

In chapter 5, such composite materials were characterized according to their internal structure and steady-state optical properties. From a fundamental point of view also, the response of systems containing nanoparticles upon laser pulse excitation is particularly interesting, as the confined size of nano-objects suggests that different processes may become relevant which are of minor importance in bulk materials. The mean free path of conduction electrons, for example, measures about 42 nm in bulk gold at 273 K [21], which is considerably larger than the diameter of the particles used in this thesis. Therefore, surface scattering will contribute considerably to the relaxation process. Moreover, knowing the time-dependent dielectric function will allow for verifying results from the simulation of such electronic processes by direct comparison to experimental data. Above this, understanding the transient dielectric function will be of great importance for the development and improvement of optical sensors [9, 138–141] or devices for communication using nano-optical components [142–144].

So far, gold films and gold-nanoparticle composites have been well studied with ultrafast pump-probe spectroscopy.[18, 34, 37, 41–43, 145, 146] For single particular wavelengths only, the transient complex dielectric constant was determined from measurements of the transmittance $T(t)$ and reflectance $R(t)$ in gold films [145] and in gold nanorods measured by optical heterodyne four-wave mixing spectroscopy.[55] Although many papers have reported on measuring the response of a system by detecting either the transmittance dT or reflectance dR [18, 34, 37, 41–44, 146], there is no broadband set of information on simultaneously measured $dT(\omega, t)$ and $dR(\omega, t)$. Consequently, there is no experimental account of the transient effective dielectric function over a broad spectral range for nanoparticle composites. Y. Takeda et al. measured the broadband dielectric functions of copper and gold nanoparticles upon laser excitation. However, they did not account for their time dependence and presented results for one particular point in time only.[18, 146]

Many publications predict the response of a nanoparticle system upon laser pulse excitation, however, without testing against experimental results because a full ex-

perimental set of data was missing. Typically, these theories calculate the smearing of the Fermi edge after relaxation of the nonthermalized electron distribution to a hot Fermi distribution after laser pulse excitation of the nanoparticles. The transient imaginary dielectric function $\epsilon_i^{Au}(\omega, t)$ is then determined from a band structure model from M. Guerrisi et al. [25] (see section 2.1) and the corresponding real part is deduced by applying the Kramers-Kronig relations. Using an effective medium model, such as Maxwell-Garnett, leads to the samples effective dielectric function.[37, 40, 42, 43]

This chapter presents results of simultaneously performed time-resolved optical measurements of the photoinduced reflectance and transmittance changes in polyelectrolyte/gold-nanoparticle structures. From the information on $dR(\omega)$ and $dT(\omega)$ and the previously derived values for the layer thickness and particle concentration (volume filling factor f), the derivation of the experimental effective dielectric function is facilitated. However, inverting the Fresnel formula is analytically difficult, even for a double-layer system. Therefore, a recursive formalism is applied, which directly finds values of the real and imaginary parts $\epsilon_r^{eff}(\omega, t)$ and $\epsilon_i^{eff}(\omega, t)$ from the measured $T(\omega, t)$ and $R(\omega, t)$ using textbook equations for describing reflectances and transmittances of thin films.[32] All required input parameters are experimentally determined. These measurement results and the procedure to derive the dielectric function were published in Physical Review B (2011).[147]

With these results it is possible to focus on the simulation of the imaginary part of the effective dielectric function as the application of Kramers-Kronig relations becomes redundant. Consequently, the assumed electronic processes which modify the effective dielectric function on the ultrafast time scale can directly be tested against experiments.

The subsequent section (6.3) presents the reflectivity measurements of coherent lattice vibrations in particles of 10 nm and 20 nm diameter. In a small range of probe energies, it was possible to observe a 180° phase difference between the oscillation. Finally, the travelling strain wave in the substrate induced by the impulsive expansion of the gold nanoparticles is monitored (section 6.4).

6.1 Transient Reflectance and Transmittance

The sample being investigated in the following sections is deposited on a PEI-covered soda-lime glass slide and exhibits a layering sequence $[(\text{PSS}/\text{PAH})_{10}+(\text{Au-NP}/\text{PAH})_4]$. It was assured that aggregation or interaction of particles is avoided and the structure was characterized by X-ray reflectometry in section 5.1.1. From the according simulations, the volume filling factor $f = 0.034$ and the thicknesses of one repetition unit ($d_{r.u.} = 22$ nm) and the overall multilayer sample ($D = 88$ nm) were derived. In section 5.2.4, the structure was identified to be uniaxially

anisotropic, and in section 5.2.5, the static effective dielectric function ϵ^{eff} was derived from measurements of $R(\omega)$ and $T(\omega)$. Since time-resolved pump-probe experiments in this thesis are typically performed at reflection angles around $\alpha = 40^\circ$, this dielectric function is used to calculate the corresponding static reflectances and transmittances for s-polarized light at that α -angle. Only if these are known, it is possible to determine the absolute values of the dielectric function from the measured relative changes $dR(\omega, t)$ and $dT(\omega, t)$.

Transient reflectance and transmittance spectra are measured according to the experimental pump-probe setup described in chapter 4.1. A 400-nm p -polarized pump pulse with a pump fluence of 5 mJ/cm^2 on the sample is used for excitation. The probe beam is adjusted to be s -polarized as the sample is isotropic for electric field vectors being perpendicular to the growth direction (z -axis) of the uniaxially anisotropic structure. The probe spectrum ranges from about 1.55 eV to 2.80 eV. The beam is strongly focused onto the sample surface in order to minimize the probe area to ensure homogeneous excitation conditions.

Results Figure 6.1 presents the results of simultaneously recorded reflectance and transmittance changes. For energies below the plasmon resonance (2.28 eV), the transient reflectance [panel (b)] decreases upon excitation, while it strongly increases above that energy. Plot (a) shows one transient signal of either domain, namely, 2.06 eV and 2.48 eV and the one corresponding to the LSPR energy. The latter reveals very slight changes only that even turn from positive to negative. The transient at 2.48 eV decreases after excitation to 0 with a relaxation constant of about 5 ps, while the others relax down to a negative residual. The differential spectra shown in figure 6.1 (e) were recorded at 1 ps, 3 ps, and 5 ps after excitation. Maximal signals occur for probe energies of 2.46 eV and 2.14 eV with changes of +14% and -8%, respectively. This difference in positive and negative contributions and the similarity of the bandwidths for positive and negative changes indicate an asymmetry of the integrated intensity change. However, the amplitudes of the negative and positive peak become equal after 4 ps.

Panels (c), (d), and (f) present according pictures of the simultaneously measured transient transmittance. The selection of energies and times shown in subplots (d) and (f) is the same as that in the description of the reflectance. The spectra shown in panel (f) suggest that the energy bandwidth of plasmon resonance considerably increases upon excitation. To be more specific, with larger times, the lower zero crossing strongly shifts to higher energies from 2.02 eV to 2.1 eV, while the crossing at 2.48 eV almost stays constant within the plotted time duration of 4 ps, indicating a widening of the LSPR upon excitation and a shift of its maximum. In 6.1 (d) the time-dependent transmittance signals of three energies are plotted. All three transients decay to a different residual and the signals at 2.06 eV and 2.48 eV change their sign during electronic relaxation.

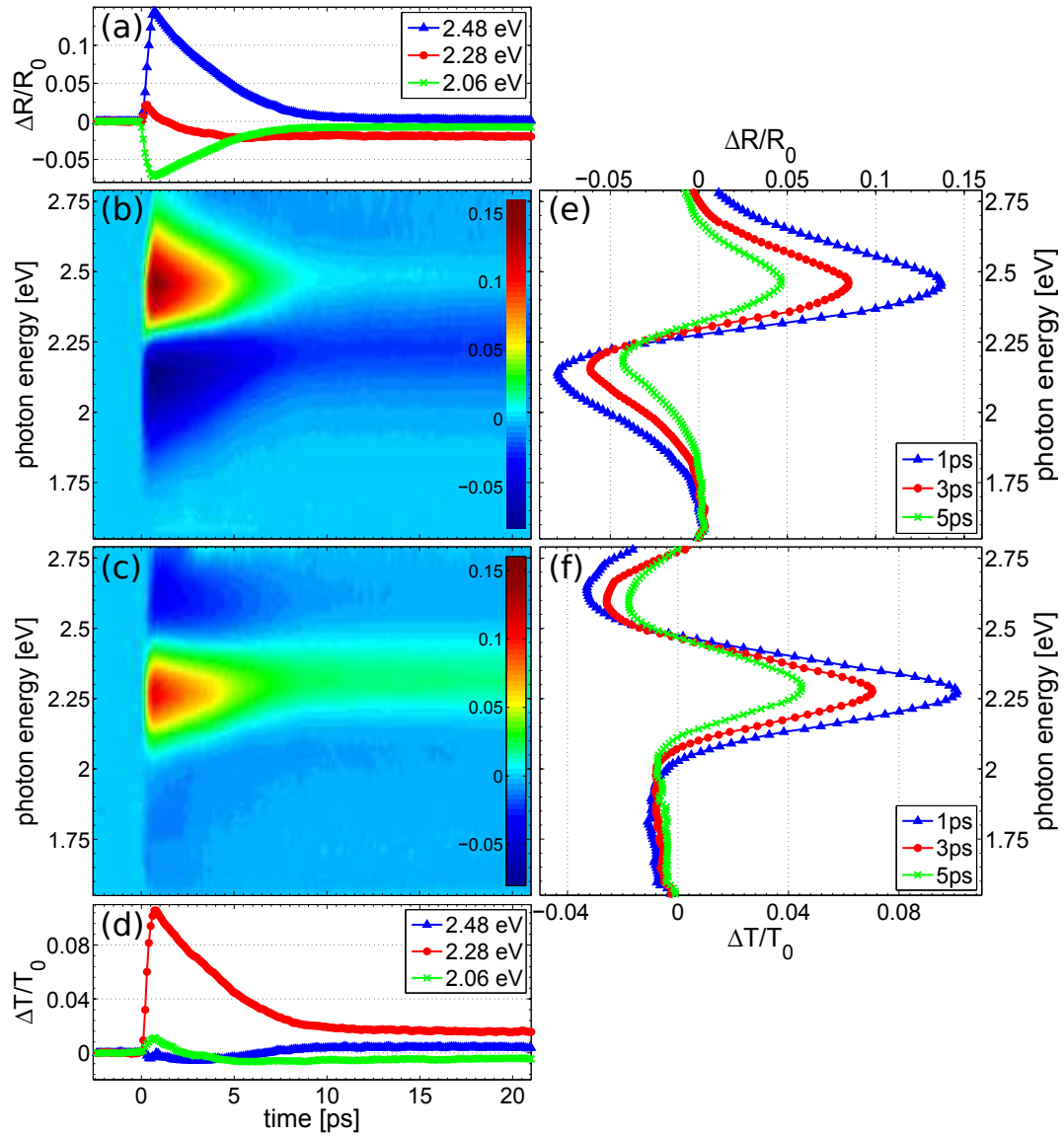


Figure 6.1: (b) and (c) show the simultaneously measured broadband reflectance $\Delta R/R_0$ and transmittance $\Delta T/T_0$, respectively. Transients of the reflectance (a) and transmittance (d) at three distinct energies. (e) and (f) show spectral projections at three distinct times after excitation.

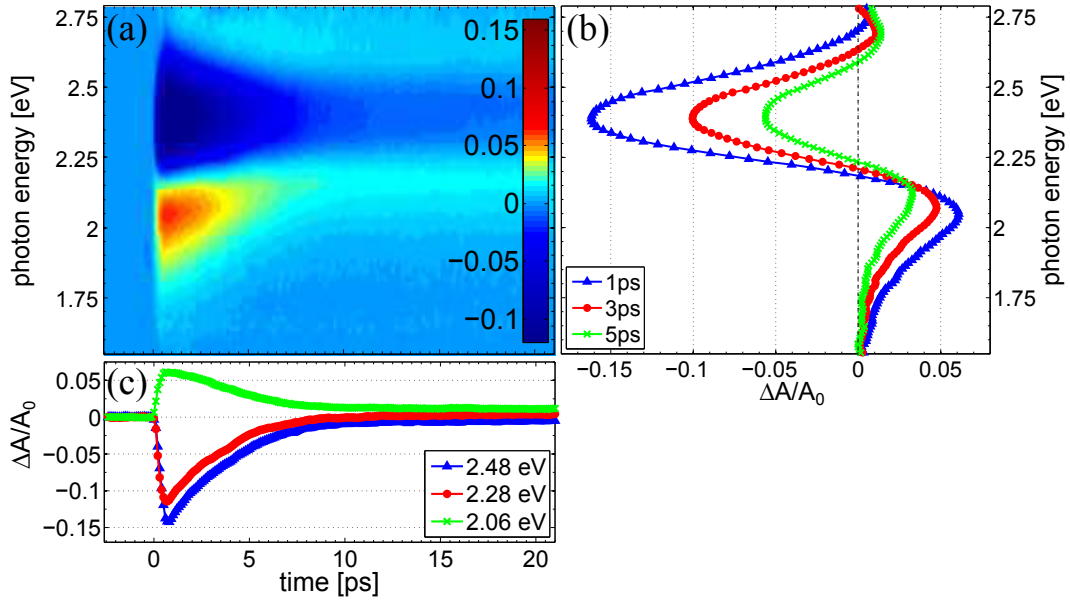


Figure 6.2: (a) Absorption ($\Delta A/A_0$) calculated from measured changes in the reflectance and transmittance. (b) Spectral projections at three distinct times after excitation. (c) Transient absorption for three energies.

Analogously, figure 6.2 presents the transient absorbance which was calculated by $\Delta A = -(\Delta T + \Delta R)$. In panel (b) again, the absorption change is plotted for three spectra determined from ΔR and ΔT that were measured 1 ps, 3 ps, and 5 ps after excitation. The plasmon resonance absorption experiences a gain in intensity below the probe energy of 2.4 eV, but a significant attenuation of -16% is observed for energies at the resonance.

Finally, figure 6.3 presents absolute spectra of the reflectance, transmittance, and absorbance in order to visualize the effects of laser excitation on the familiar absolute quantities. The left column shows spectra that were measured within the first 600 fs after excitation, i.e. for the nonthermal electron distribution that thermalized to the hot Fermi distribution. The spectra in the right column belong to times >3 ps and thus visualize the relaxation process of the electrons. Additionally, each graph comprises the according steady-state spectrum (black curve).

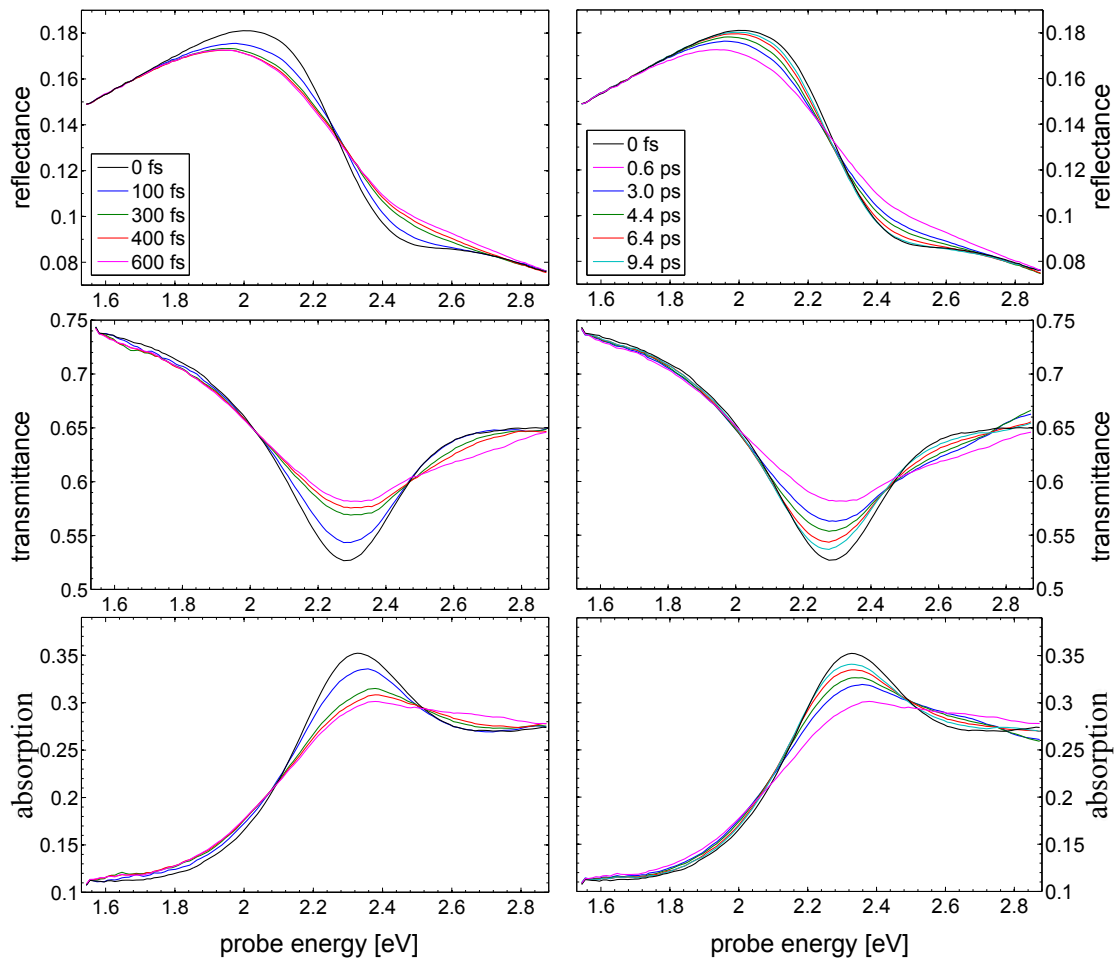


Figure 6.3: Measured absolute spectra of the reflectance (a) and (b), transmittance (c) and (d), and absorbance (e) and (f). The left side shows spectra during the thermalization process to a hot Fermi distribution ($0 < t < 600$ fs after excitation), and the right side shows spectra during the relaxation process ($0 < t < 9.4$ ps after excitation).

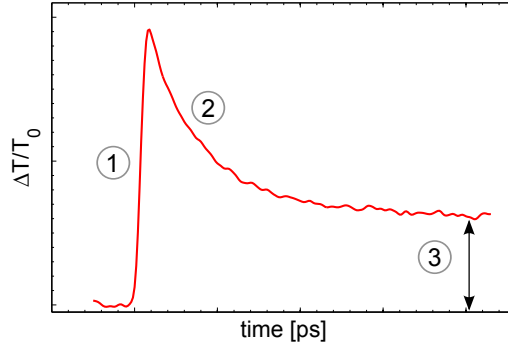


Figure 6.4: Illustrations of the three characteristic processes in pump-probe measurements. (1) Excitation and thermalization of the electrons to a hot Fermi distribution. (2) Transfer of electronic energy to the lattice via electron–phonon coupling. (3) Lattice relaxation (typically several nanoseconds).

Discussion The measured transient reflectances and transmittances are in good agreement with experimental results and predictions in the literature. Figure 6.4 shows an exemplary transient ($E_{probe} = 2.24$ eV) in order to explain the characteristic spectral features of a pump-probe signal, which comprises the rise time (1), the decay (2), and the residual value (3).

(1) The detected rise time of the signal peak amounts to ~ 600 fs. This rise time is a measure of the relaxation from the laser induced nonequilibrium electron distribution to a hot Fermi distribution by electron–electron scattering and electron–surface scattering [36, 40, 41, 46], which is described by the electron thermalization time τ_{th} . The nonequilibrium electron distribution here is created by pumping at 400 nm, which triggers intraband transitions inside the sp-band and interband transition of electrons from the d-band into the sp-conduction band [Figure 2.4 (a)]. The thermalization process is illustrated in figure 2.7 (a)–(c), which shows the electron energy distribution at the Fermi energy before excitation (a), the nonthermalized electron occupation immediately after excitation (b), and the thermalized hot Fermi distribution a few hundred femtoseconds later (c). Taking into account the given time resolution of 150 fs, the measured time of 600 fs conforms with the previously calculated and observed values of $\tau_{th} = 500$ fs. [40, 41]

The excitation of a thermalized electron distribution results in the broadening and shifting of the plasmon resonance [46, 56] which is nicely illustrated in the absorbance spectra in figure 6.3 (e) and (f). One effect that contributes to the plasmon peak attenuation results from the blue shift of the resonance upon excitation. That is, with shifting of the plasmon closer to the interband transitions, the imaginary part of the particles' dielectric function increases. Consequently, the mismatch of the plasmon resonance condition $\epsilon_{Au} = -2 \cdot \epsilon_{pol}$ becomes larger and the plasmon absorption band is less pronounced. This situation was discussed before in section 5.2.2.

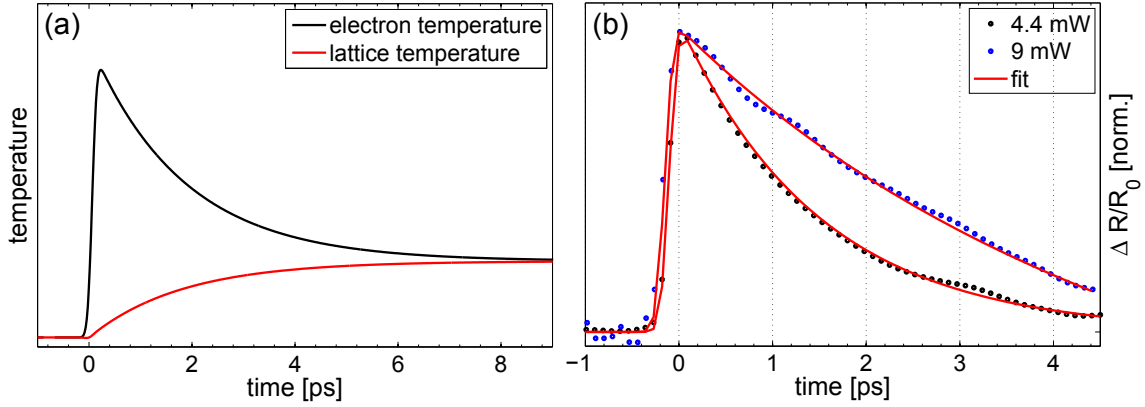


Figure 6.5: (a) Sketch of the electron and lattice temperatures during the electron–phonon coupling process. (b) Measurement of transient electronic signals for two different pump fluences.

(2) Immediately after excitation, the electrons interact with the lattice by transferring energy to the particle ions via electron–phonon interaction.[33] This is reflected in the measurement by the decay of the strong signal peak (see Figure 6.4). The temperatures of the lattice T_L and the electrons T_e during this process are described by the two-temperature model (TTM) [33, 148], which uses two coupled differential equations for describing the heat conduction of the electrons (C_e) and of the lattice (C_L) as

$$C_e(T_e)\delta T_e/\delta t = -G(T_e - T_L) \quad \text{and} \quad C_L\delta T_L/\delta t = G(T_e - T_L), \quad (6.1)$$

where G is the coupling constant that is related to the scattering rate τ_{ph} . Figure 6.5 (a) illustrates a sketch of the corresponding electron and lattice temperatures (T_e and T_L , respectively) during the electron–phonon coupling process for weak excitations. In this low perturbation regime, the measured transients exhibit the same decay behavior as the electron temperature, that is $\Delta T/T_0 \propto T_e$, where T_e behaves monoexponentially.

However, the measured transients here clearly deviate from such monoexponential relaxation kinetics which can be attributed to the strong excitation conditions. For strong perturbations, T_e is not simply decaying exponentially anymore and is no longer proportional to the measured transients. This deceleration of the relaxation process is a consequence of the temperature dependence of the electronic heat capacity $[C(T_e)]$. The TTM accounts for this correlation and predicts a rather linear decay for strong excitation conditions and an exponential decay for low excitation conditions.[50] Figure 6.5 (b) shows the measured transients of the normalized reflectance, which clearly indicate different electron–phonon coupling times τ_{e-ph} for two different pump energies. While the lower curve can be fitted with an exponen-

tial function with a decay time of 1.54 ps, the high-intensity pump transient clearly differs from such decay kinetics and behaves rather linear. Note that the coupling constant G in this model is constant.

(3) During thermalization of the electrons with the lattice, the absolute value of the detected signals decrease, however, only down to a residual value which persists throughout the measured temporal range. This residual results from the heated lattice system and disappears when the heat is transferred from the metal particles to the dielectric surrounding medium by heat diffusion. This relaxation process depends on the thermal conductivity of the dielectric medium and is on the order of a few nanoseconds. It is not investigated in this thesis.

6.2 Transient Dielectric Function

This section describes the direct derivation of the transient complex effective dielectric function $\epsilon_{eff}(\omega, t)$ of the nanoparticle/polyelectrolyte compound structure from the measured changes in the reflectance and transmittance. Generally, it is possible to calculate the real and imaginary parts of a dielectric function by inverting the Fresnel equations. However, the expressions for $R(\omega)$ and $T(\omega)$ are particularly complex for multilayer systems due to interference effects and multiple reflections inside the structure. Even for a single effective medium layer on a substrate, this inhibits the derivation of an analytical expression for $\epsilon_{eff}(R, T)$. Therefore, a numerical method is derived, in which $R(\omega)$ and $T(\omega)$ are calculated for the ranges of possible values of $\text{Im}(\epsilon_{eff})$ and $\text{Re}(\epsilon_{eff})$. On comparison with the measured values of $R(\omega)$ and $T(\omega)$, the actual values of $\text{Im}(\epsilon_{eff})$ and $\text{Re}(\epsilon_{eff})$ are identified unambiguously. The assumed range of values for the real part of the dielectric function $\text{Re}(\epsilon_{eff})$ varies from 2.25 to 3.23, while the values of the imaginary part $\text{Im}(\epsilon_{eff})$ part lie between -1 and 0. For any possible combination of $\text{Re}(\epsilon_{eff})$ and $\text{Im}(\epsilon_{eff})$, the absolute reflectance $R(\epsilon_{eff})$ and transmittance $T(\epsilon_{eff})$ is determined by the matrix formalism, deduced in chapter 2.2. In order to compare these absolute expressions of R and T to the measured relative values (dR and dT), the derived expressions are modified with the static values $R_0(\omega)$ and $T_0(\omega)$ (plotted before in figure 5.16) to

$$dR(\epsilon_{eff}) = \frac{R(\epsilon_{eff}) - R_0}{R_0} \quad \text{and} \quad dT(\epsilon_{eff}) = \frac{T(\epsilon_{eff}) - T_0}{T_0}. \quad (6.2)$$

The two contour plots in figure 6.6 present the calculated transient reflectances and transmittances as functions of the dielectric real (x-axis) and imaginary parts (y-

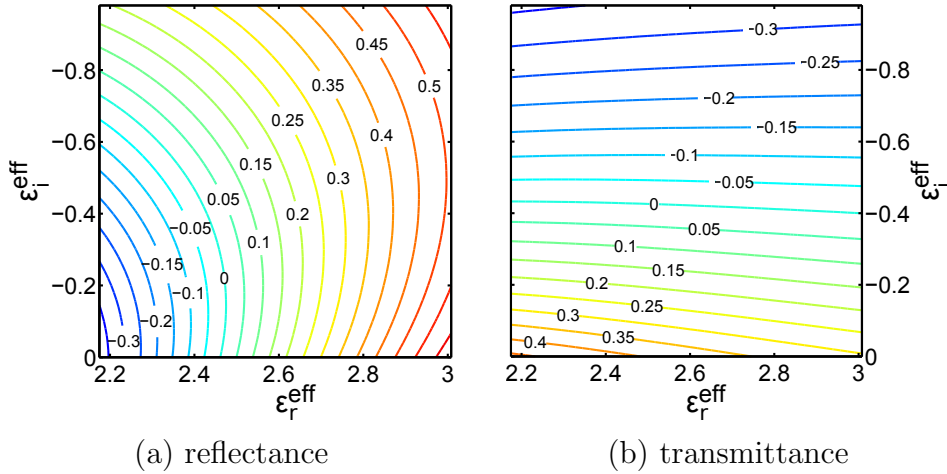


Figure 6.6: Calculated change in the reflectance (a) and transmittance (b) as a function of the assumed values of the real and imaginary parts of the effective dielectric function. These matrices apply to a probe light wavelength of 543 nm.

axis) for the particular wavelength of 543 nm. For the assumed ranges of $\text{Im}(\epsilon_{eff})$ and $\text{Re}(\epsilon_{eff})$ at that wavelength, the reflectance covers changes from -35% to +55% and the transmittance from -35% to +40%. This set of plots is calculated individually for each probe wavelength. Finally, the intersection of the contour lines that equal the measured values of $dR(t)$ and $dT(t)$ is identified for every set of plots and every measured point in time. The according real and imaginary parts of $\epsilon_{eff}(\omega, t)$ can be read off from the x- and y-axis, respectively.

Figure 6.7 presents the unnormalized change in the dielectric function $\epsilon^{eff}(\omega, t) - \epsilon_0^{eff}(\omega)$. Again, three spectral profiles at 1 ps, 3 ps, and 5 ps are plotted as well as the temporal cuts at 2.06 eV, 2.28 eV, and 2.48 eV.

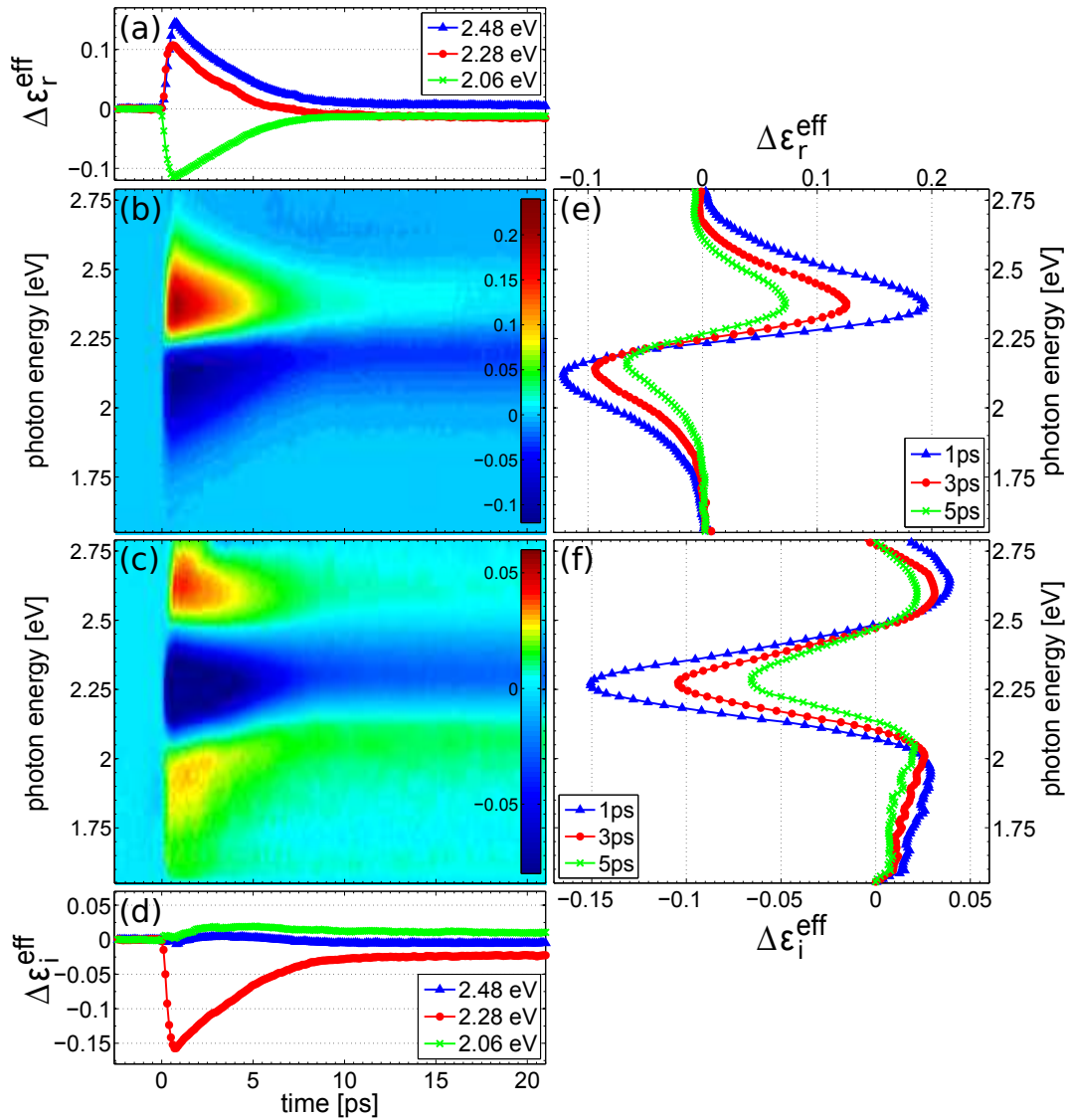


Figure 6.7: Transient real (a)–(c) and imaginary (d)–(f) parts of the dielectric function determined from simultaneous measurements of the reflectance and transmittance. Again, three temporal and spectral cuts from the 2D contour plots are presented.

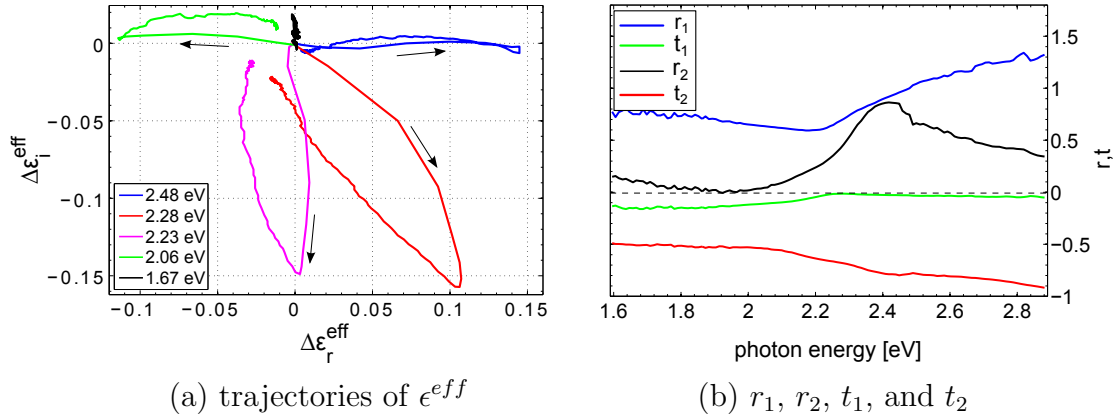


Figure 6.8: (a) Measured trajectories of the complex dielectric function as a function of time. (b) Spectral dependence of coefficients that correlate the measured quantities ΔR and ΔT to $\Delta\epsilon_r^{\text{eff}}$ and $\Delta\epsilon_i^{\text{eff}}$

Five characteristic trajectories are plotted in figure 6.8 (a), visualizing the time dependence of the changes in the real and imaginary parts of the effective dielectric function for different energies. Wavelengths are identified at which either the real (2.06 eV and 2.48 eV) or the imaginary part (1.67 eV and 2.23 eV) is affected only. The wavelengths inbetween experience changes in both the components of ϵ_{eff} . The absolute change in the shown trajectories clearly differs for different wavelengths. However, the change at 1.67 eV of only 0.1 in the imaginary part corresponds to a high relative change of +27% as the static imaginary part at this energy is very small.

From comparison of the spectral profiles in figure 6.1 (e) and (f) and figure 6.7 (e) and (f) the changes in $\text{Re}(\epsilon_{\text{eff}})$ and $\text{Im}(\epsilon_{\text{eff}})$ seem to conform qualitatively with $dR(\omega)$ and $dT(\omega)$, respectively. The exact correlation of the measured quantities with the dielectric function is given by [18, 40, 145, 146]

$$\frac{\Delta R}{R} = r_1 \Delta\epsilon_1 + r_2 \Delta\epsilon_2 \quad (6.3)$$

$$\frac{\Delta T}{T} = t_1 \Delta\epsilon_1 + t_2 \Delta\epsilon_2. \quad (6.4)$$

C. Voisin et al. [41] found a pronounced wavelength dependence for these coefficients of a gold-nanoparticle/glass compound structure. They compared the measured reflectance and transmittance with a simulation of the according dielectric function. The calculated coefficients found in this case are plotted in figure 6.8 (b). The imaginary part of the dielectric function dominates the transient transmittance over the whole spectral range ($|t_2| \gg |t_1|$), even across the resonances. The contributions

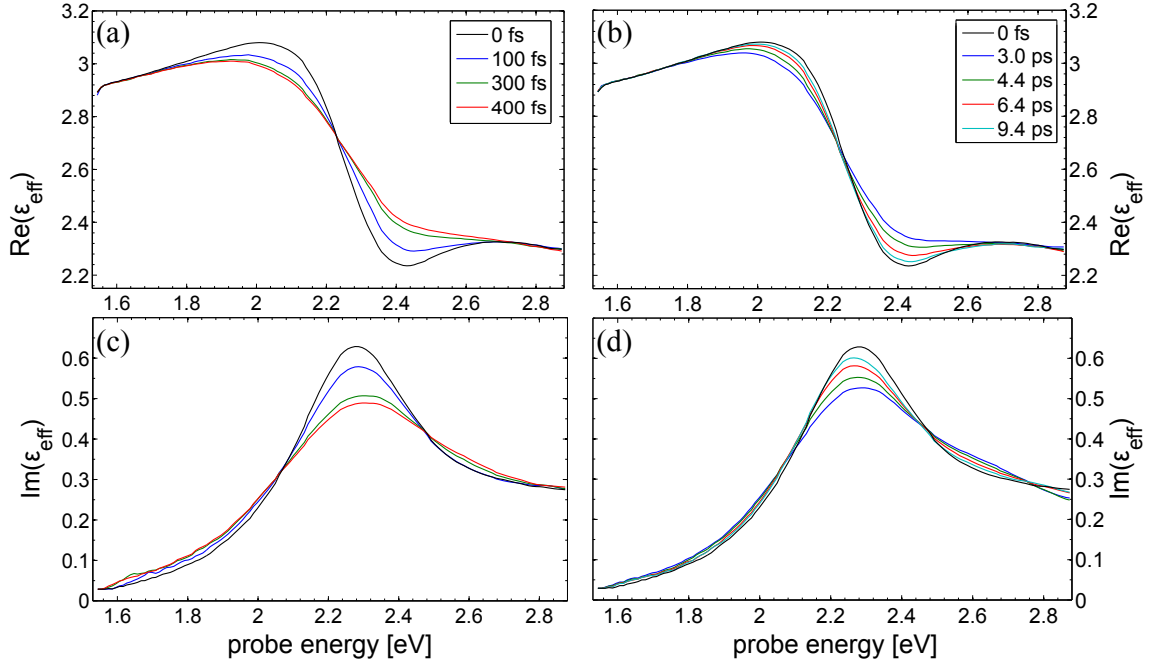


Figure 6.9: Absolute real (a) and (b) and imaginary (c) and (d) parts of the dielectric function. The left side shows spectra during the thermalization process shortly after excitation. The spectra on the right illustrate the relaxation back to the steady-state dielectric function (black line).

from both real and imaginary parts to the reflectance show a significant rise for energies above 2.2 eV, which is even more pronounced for r_2 . Finally, figure 6.9 presents absolute spectra of the real and imaginary parts of the dielectric function, analogously to figure 6.3.

Conclusion The transient dielectric function shown in figure 6.7 is experimentally derived from simultaneous measurements of dR and dT . All input parameters required for the precise determination, such as the layer thickness and the dielectric function of the substrate, were determined experimentally beforehand. This set of information represents a unique testground for theories and simulations describing the mechanisms of excitation and relaxation upon laser heating in the nanoparticle/polyelectrolyte compound system. The theories can now be directly compared to experimental results, and the application of Kramers-Kronig relations is redundant. Note that such a comparison implies that the applied effective medium theory (Maxwell-Garnett) used in the simulations describes the system correctly.

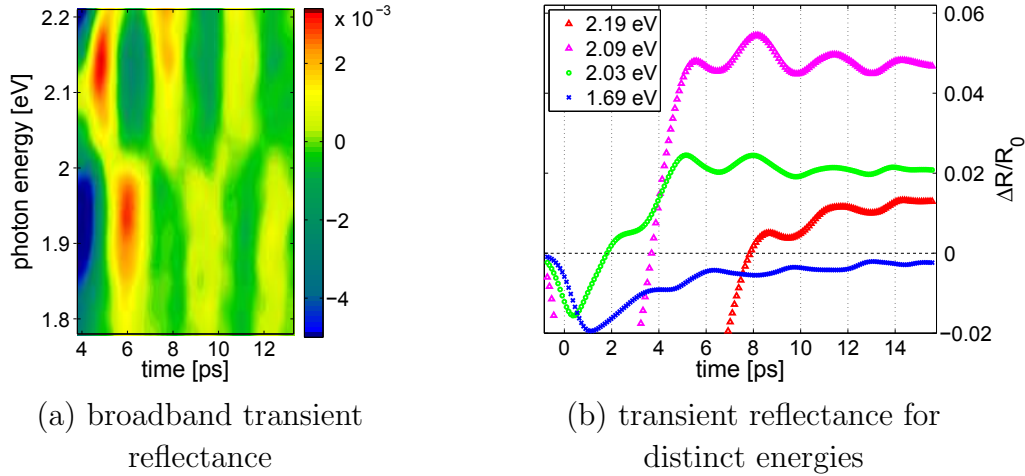


Figure 6.10: (a) 2D color-coded transient reflectance ($\Delta R/R_0$) for probe energies ranging from 1.78 eV to 2.21 eV for three oscillation periods. (b) Transient reflectance for four different energies. The investigated sample comprises four gold-nanoparticle layers.

6.3 Excited Vibrational Modes in 10 nm and 20 nm Gold Particles

When energy is transferred from the hot electrons to the lattice via electron–phonon coupling the temperature of the lattice increases [see Figure 6.5 (a)]. This lattice temperature rise induces stress in the particle, which in turn leads to an isotropic expansion of the particle to a larger diameter D^{hot} . If the energy transfer happens on ultrashort time scales, the force expanding lattice rises impulsively, resulting in an overshoot of the expansion, according to the displacive excitation mechanism. Restoring forces then cause the particle to contract again, and the particle performs a volume oscillation around the diameter D^{hot} . Here, the coherent vibrational motion is monitored and analyzed for an ensemble of particles with 10 nm and 20 nm diameter.

Results Figure 6.10 presents results of pump-probe measurements of the sample used previously within this chapter. It has a layering sequence $[(PSS/PAH)_{10}+(Au-NP/PAH)_4]$. This sample is pumped using the NOPA output beam at 540 nm, while the wlc serves as the probe beam. The data were recorded in reflection geometry at large alpha angles ($\alpha \approx 70^\circ$). The transient reflectance, which is presented in the two-dimensional plot in figure 6.10 (a) for times ranging from 3.9 ps to 13 ps after excitation, reveals a periodically changing signal for a broad energy range (1.78 eV to 2.21 eV). The oscillating period T_{10} for 10-nm particles measures

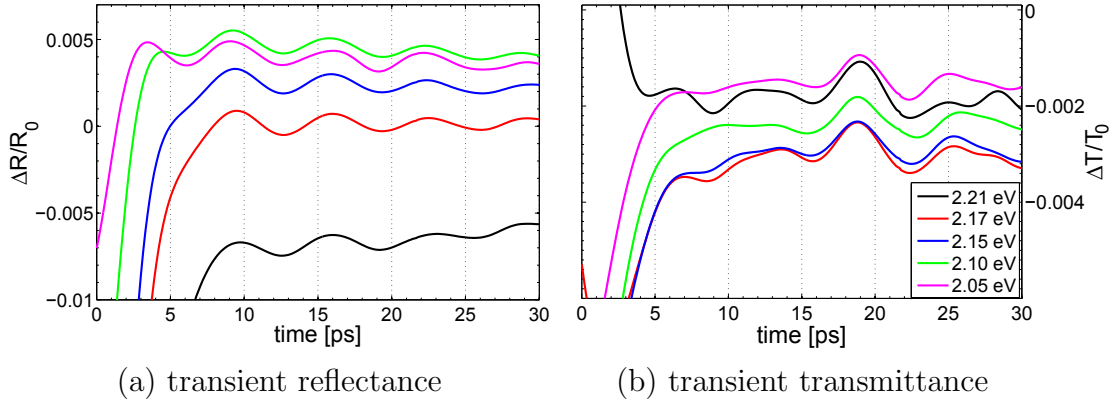


Figure 6.11: Simultaneously measured transient reflectance (a) and transient transmittance (b) of the vibrational mode of 20-nm gold nanoparticles in a polyelectrolyte matrix. The investigated sample comprises four nanoparticle layers.

3.3 ps. The oscillations for energies above 2.02 eV are 180° out of phase as compared to the ones below 2.02 eV. Panel (b) visualizes the transient signal of four distinct probe energies (1.69 eV, 2.03 eV, 2.09 eV, and 2.19 eV). The plotted data were smoothed by using a Mathcad built-in function, which basically eliminates high-frequency noise components in the signal by convolution with a Gaussian function. This explains the broadening of the sharp signal peak in figure 6.10 (b).

In figure 6.11, the results of pump-probe measurements of a sample containing 20-nm gold nanoparticles are shown. This structure, which has the layering sequence [(PSS/PAH)₁₀+(Au-NP₂₀/PAH)₄], was investigated by simultaneously measuring the transient transmittance (a) and reflectance (b). Only distinct transients are plotted because large noise signals inhibited the evaluation for a broadband energy range. The measured oscillation period amounts to $T_{20} = 6.67$ ps.

Discussion The observed oscillation periods of 3.3 ps and 6.67 ps are in good agreement with the calculated ones of $T_{10} = 3.29$ ps and $T_{20} = 6.60$ ps, which were determined by

$$T = \frac{\pi \cdot d}{\eta \cdot c_L}, \quad (6.5)$$

for $d = 10$ nm and $d = 20$ nm particles, respectively. η is an eigenvalue which equals 2.94 and was deduced from $\eta \cot \eta = 1 - (\eta c_L / 2c_T)^2$, where $c_L = 3250$ m/s is the longitudinal sound velocity and $c_T = 1200$ m/s is the transversal sound velocity for gold.[37, 149, 150]

Most of the papers which reported on monitoring the vibrational mode of nano-objects, such as spherical particles, rods, and triangular-shaped objects, have pre-

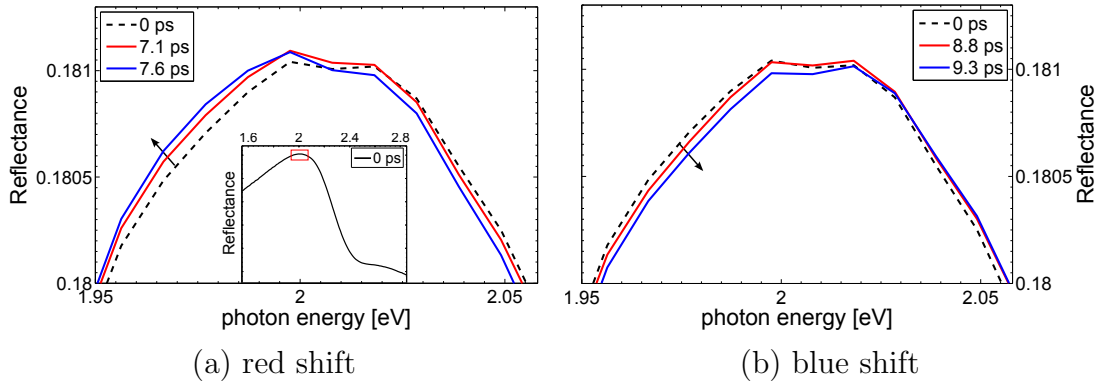


Figure 6.12: Absolute reflectance spectra during vibrational motion of 10-nm gold nanoparticles. (a) Spectra measured at 7.1 ps and 7.6 ps after excitation, visualizing the shift to the red. (b) Blue-shifted spectra recorded one half period later. The dashed line in both panels represents the static reflectance spectrum.

sented transmittance measurements at distinct probe wavelengths in the vicinity of the plasmon resonance maximum.[44, 151] From the results, it was concluded that the plasmon resonance is periodically shifting into the red and blue. In 2009, M. Pelton et al. [56] presented broadband transmittance measurements at energies around the longitudinal surface plasmon resonance of bipyramidal nanoparticles, clearly monitoring the extensional mode. The results verify that red and blue shifting of the resonance is responsible for the oscillatory signals. However, the volume change cannot directly be responsible for the observed signals, as the maximum position of the plasmon resonance is invariant for particles with diameters <50 nm. A well-accepted explanation (see section 2.3) argues that by varying the particle volume, the free electron density is modified counterwise.[37, 152] This modifies the plasma frequency of the nanoparticle material which essentially determines the maximum spectral position of the plasmon resonance. That is, the maximum position of the plasmon resonance ω_0 of the effective medium is given by the relation[21, 152]

$$\omega_0 = \frac{\omega_p}{\sqrt{1 + 2\epsilon_m}} = \sqrt{\frac{n_e e^2}{\epsilon_0 m_e (1 + 2\epsilon_m)}}, \quad (6.6)$$

where n_e is the electron density and ϵ_0 and ϵ_m are the dielectric constants of vacuum and of the polyelectrolyte embedding medium, respectively.

The broadband transient reflectance in figure 6.10 (a) was used to determine absolute reflectance spectra $R(\omega)$ from the static measured reflectance $R_0(\omega)$ at different times during one oscillation period by $R(\omega) = R_0(\omega)(1 + dR(\omega))$. The result is plotted in figure 6.12. The phase shift of 180° (see Figure 6.10) was observed at an energy of 2.02 eV, which corresponds to the spectral position of maximum static reflectance, as indicated in the inset of figure 6.12 (a). Panels (a) and (b) show

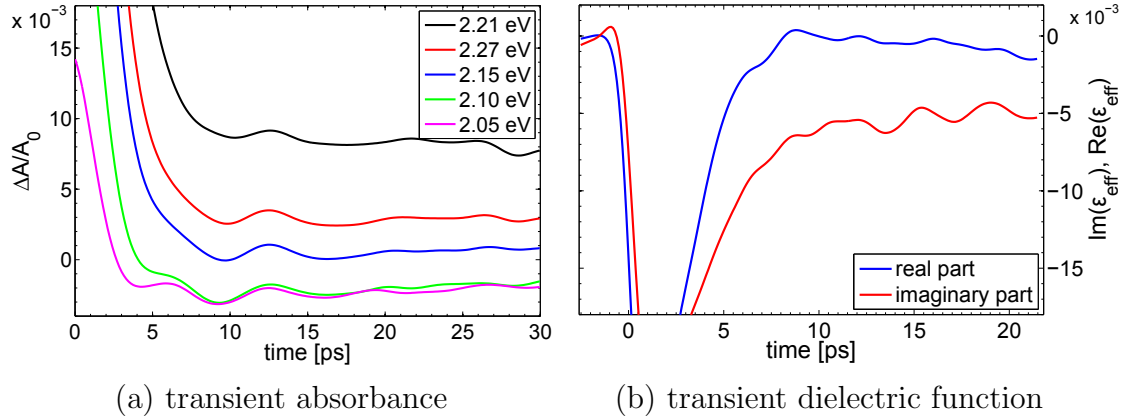


Figure 6.13: (a) Transient absorption of 20 nm gold nanoparticles embedded in polyelectrolytes. (b) Real and imaginary part of the dielectric function of 10 nm gold particles measured at 659 nm.

time-dependent spectra of the absolute reflectance in the vicinity of this energy along with the measured static spectra (dashed lines). Panel (a) presents spectra for 7.1 ps and 7.6 ps after excitation, clearly verifying a shift to the red. About one half period (1.7 ps) later, the spectrum is shifted to the blue, as shown in panel (b). These observations are in agreement with the theory of a periodically shifting plasmon resonance, since a plasmon shift goes along with an according shift of the reflectance features (see section 2.1).

From the simultaneously measured reflectance and transmittance spectra shown in figure 6.11 for a structure containing 20-nm gold nanoparticles, the corresponding absorption and the according dielectric function are calculated. The resulting transients of the absorption are shown in figure 6.13 (a). Figure 6.13 (b) presents the time-dependent real and imaginary parts of the effective dielectric function at 659 nm (1.88 eV). Clearly, the absorbance and both transients of the dielectric function change periodically upon vibrational motion of the particles.

Unfortunately, these data do not allow the derivation of the broadband time-dependent spectra of the absorption and the effective dielectric function for one breathing cycle, which would allow one to clearly identify the contributions of $\text{Im}(\epsilon_{\text{eff}})$ and $\text{Re}(\epsilon_{\text{eff}})$ to the shift of the plasmon resonance upon optical excitation and vibrational motion. Recent measurements have been performed in our group by Steffen Mitzscherling which monitor the vibrational mode in reflection and transmission geometries of a sample containing 150-nm particles for a broad energy range. From these data, it will be possible to calculate the absolute quantities of $R(\omega, t)$ and $T(\omega, t)$ and therefore the transient dielectric function $\epsilon^{\text{eff}}(\omega, t)$ during lattice oscillations.

The presented figures in this section show oscillations of more than five periods, where the first one is hidden in the strong electronic signal for some transients. The detection of coherent vibrational motions of an ensemble of particles is limited by

dephasing. That is, the polydisperse size distribution of the individual particles results in vibrational motions with different periods, according to equation 6.5. Consequently, a fast dephasing of the signals from the individual particles occurs and the average signal from the ensemble is strongly damped. For example, the vibrational motion of particles with diameters of 20.8 nm and 19.2 nm are 180° out of phase after six oscillation periods. P. V. Ruijgrok et al. presented measurements of vibrational motions showing more than 20 periods. This was achieved by monitoring the response of a single nanoparticle only, such that the dephasing effect for an ensemble of particles was eliminated. Therefore, the particle was isolated by using an optical trap.[153] In other cases a single nanoparticle system was investigated by focussing the probe beam down to the diffraction limit (few hundred nanometers) using microscopic objectives.[50] Also, very large particles and nanorods are less prone to dephasing as for such particles different probe wavelengths are sensitive to different particle diameters or rod lengths.

6.4 Monitoring the Propagating Strain Pulse in the Substrate

In section 6.3, the coherent excitation and propagation of isotropic elastic strain waves in an assembly of gold nanoparticles was investigated. It was shown that the particles in the given structure perform a collective breathing motion, which is monitored via ultrafast pump-probe spectroscopy. Here, it is shown that by impulsive expansion of the particles, a strain wave is triggered which is launched first into the polyelectrolyte environment and then into the substrate.

The following results were obtained from the time-resolved optical experiments, in which the sample is excited with a ~530-nm pump pulse and the probe beam is recorded in reflection geometry. Again, the investigated sample has the layering sequence [(PSS/PAH)₁₀+(Au-NP/PAH)]₄.

Results Figure 6.14 presents four transients of the reflectance measured at different probe wavelengths. Each transient shows an oscillating signal with a period that changes with probe wavelength. These data were smoothed using a Mathcad implemented function. High-frequency noise is therefore eliminated and the long-range oscillations (30–54 ps) remain. The ultrafast electronic response of the system to the pump pulse is considerably smeared out due to the smoothing routine.

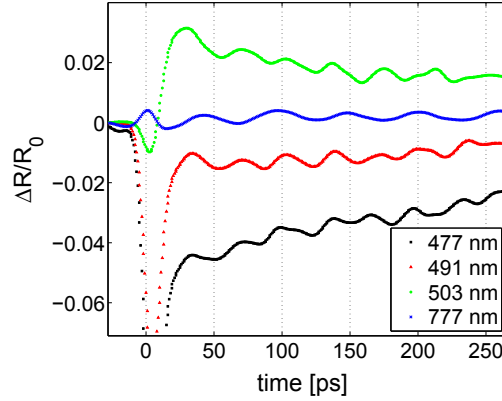


Figure 6.14: Measured transient reflectance $\Delta R/R_0$ showing oscillations with probe-energy-dependent periods. The investigated sample exhibits four stratified nanoparticle layers and particles with a diameter of 10 nm.

Discussion By the instantaneous expansion, each particle launches a spherical strain wave into the polyelectrolyte environment. Since the particles are arranged in well stratified layers, it is assumed that according to the superposition principle these waves generate a planar strain wave front which propagates along the layer normal. This assumption is supported by the fact that the excited area is significantly larger than the probed one, which gives rise to the generation of planar wave fronts as well. The generated strain wave travels at the longitudinal speed of sound to the polymer-substrate interface, where it is partly transmitted and partly reflected. The ratio of the transmitted to the reflected intensity is determined by the difference in acoustic impedance of the two media at the interface. The acoustic impedance of a material is a function of its density (ρ) and Young's modulus (E), that is, $Z = \sqrt{\rho \cdot E}$. The reflectance for the strain wave at the interface is then given by

$$R_{strain} = \frac{Z_{pol} - Z_{glass}}{Z_{glass} + Z_{pol}} \quad (6.7)$$

which becomes minimal for perfect impedance matching, that is, for $Z_{pol} = Z_{glass}$ R_{strain} is zero, and consequently, the transmission is maximal ($T_{strain} = 1$). Since polymers such as PAH and PSS are viscoelastic they exhibit solid-like impedances for stress that is applied on ultrashort time scales.[154] It is therefore expected that the polyelectrolyte embedding medium facilitates the transmission of the high-frequency strain wave into the glass substrate. C. Thomson et al., in 1986, simulated the shape of such a photoexcited strain wave front inside a thin film, as shown in picture 6.15 (a). Such bipolar strain pulses are characterized by a leading compressive part (positive strain amplitude), which is followed by an expansional one.[155]

In general, strain affects the material parameters n and κ , and in this special case,

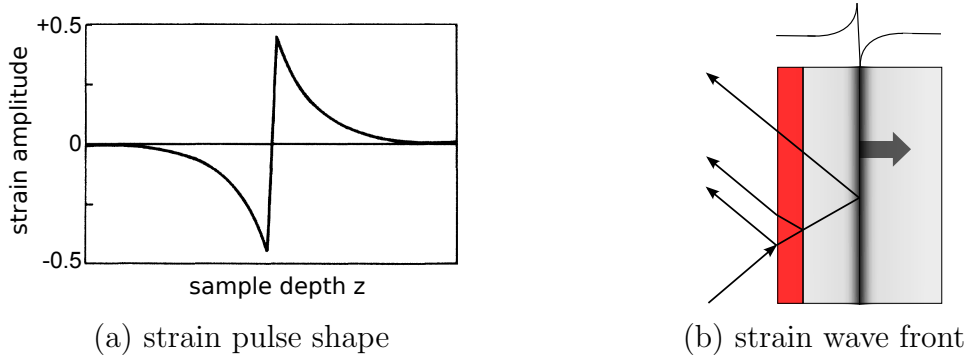


Figure 6.15: (a) Illustration of a dipolar strain pulse. (b) The detected reflectance results from an interference of the sample layer reflectance and the travelling strain pulse in the substrate.

it results in a sharp discontinuity of the refractive index n of the glass, which can be regarded as an additional interface which reflects the incoming light. C. Thomsen et al. furthermore formulated an expression for the reflectivity at the samples surface including the contribution from the moving strain pulse in the structure, which is illustrated in figure 6.15 (b). The interference of the individual reflected beams leads to a modification of the detected reflectivity $R(\omega, t)$. As the strain pulse propagates into the substrate, the phase difference in these reflected waves changes sinusoidally and consequently does $R(\omega, t)$. One oscillation period is performed exactly when the strain wave travels a distance which is equal to the wavelength of the probe light. Therefore, this process depends on the probe wavelength. The expression for $R(\omega, t)$ given by C. Thomsen et al. can be reduced to a proportionality relation which includes this wavelength dependence:[155]

$$\Delta R(t) \propto \sin\left(\frac{4\pi nvt}{\lambda} - \phi\right) \quad , \quad (6.8)$$

where v is the speed of sound in the soda-lime substrate. By Fourier analysis of the measured data, the corresponding frequency spectra are determined. The results are plotted in figure 6.16 (a), revealing a discrete frequency for each measured transient. Note that the limited number of measured points in time restricts the spectral resolution of the Fourier spectrum, which here measures about 0.001 ps^{-1} . Figure 6.16 (b) presents the derived frequencies as a function of the probe wavelength. A fit, which is based on equation 6.8, is plotted along with the data. The only fitting parameter is the speed of sound, which in fact is the slope of the line and is identified to measure 4700 m/s .

In 2011, M. Herzog et al. from our group reported on quantitative pump-probe measurements of the transient strain in a nanolayered perovskite structure on a $SrTiO_3$ (STO) substrate.[156] By probing with ultrafast X-ray diffraction, it was possible to observe a rising shoulder to the substrate Bragg peak caused by the strain wave

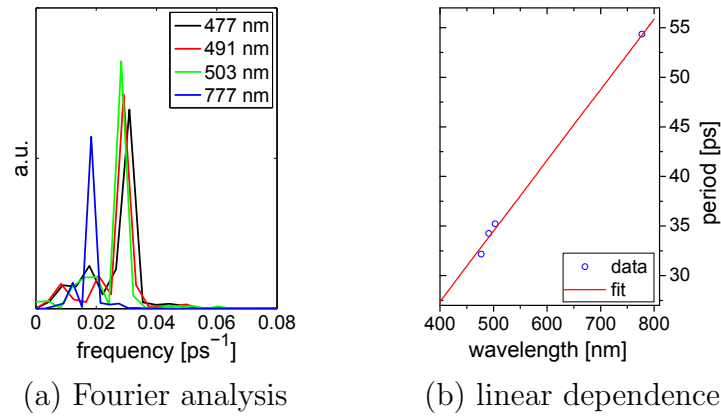


Figure 6.16: (a) Fourier analysis of the detected oscillations in the reflectance transients. (b) Oscillation frequency plotted versus the probe wavelength. The slope is a measure of the sound velocity in the glass substrate.

in the substrate. Theoretical modelling allowed to assign absolute values of strain to the observed modifications of the X-ray diffraction pattern. Repeating the experiments with identical excitation conditions in an all optical pump-probe setup allowed to also calibrate the detected amplitude to the induced strain. Therefore, a future experiment is to substitute the glass substrate by a STO one and repeat the measurements. By an analysis of the measured oscillation amplitude, one should be able to absolutely determine the strain produced by breathing nanoparticles. However, the detection in STO will be more difficult as compared to glass, since STO exhibits a higher acoustic impedance which results in a smaller transmission coefficient for the incoming acoustic strain wave. Consequently, the detected signal is expected to show a significantly smaller amplitude.

7 Summary

Preparation of Stratified Multilayer Structures

Polyelectrolyte structures with highly stratified gold-nanoparticle layers were successfully fabricated by both the dip-coating and the spin-coating layer-by-layer methods. For time efficiency reasons, the spin-coating method was the standard way to prepare the layered structures. A typical structure is deposited on a PEI covered substrate and exhibits the layering sequence $[\text{PEI}+(\text{PSS}/\text{PAH})_8+(\text{Au-NP}/\text{PAH})_4]$ which is a total of 73 layers. It was possible to produce stratified layers with polyelectrolyte spacer thicknesses of the order of the particle diameter (10 nm). The structures were thoroughly characterized using the X-ray reflectivity, optical spectroscopy, atomic force microscopy (AFM), transmission electron microscopy (TEM), and angular resolved reflection and transmission methods (chapter 5). The XRR-scans (see Figure 5.4) show small-angle Bragg peaks up to the seventh order, evidencing the stratified structure. The results derived from these scans were cross-checked by additional methods such as AFM (global and local roughnesses) or absorption spectroscopy (volume filling factor). The shown TEM image in figure 5.6 nicely visualizes the profound stratification of the nanoparticle layers.

The smoothing effect (section 5.1.3), which describes the reduction of the surface roughness and the compensation of surface imperfections by adsorption of polyelectrolyte layers, is a decisive factor in the buildup process of stratified particle layers. Optical absorption experiments verified the volume filling factor derived by XRR and AFM. Because of the birefringent nature of the structure, which was verified by angular-dependent reflectance and transmittance spectroscopy in section 5.2.4, all optical experiments were either performed at 0° or using s-polarized light.

Interaction of Particles and Particle Layers

The results obtained in section 5.2.1 and 5.2.3 facilitate the building of structures with well defined in-plane particle concentrations and particle-plane separations. Using a 50% diluted nanoparticle solution and a 60-min adsorption time results in a “dense” nanoparticle layer without the occurrence of clustering.

The optical absorption of a single nanoparticle layer was studied as a function of the cover layer thickness by accurate and comprehensive UV-Vis spectroscopy measurements (section 5.2.2). Reflectances and transmittances of samples were quantified by using an integrating sphere, which also detects the forward and backward scattering components. The absorption is then correctly determined by $A = 1 - T - R$.

With the deposition of transparent polyelectrolyte cover layers, a red shift of the plasmonic maximum and an increase of the spectrally integrated absorption were observed. The saturation of these effects is a measure of the plasmon interaction range which was determined to be on the order of the particle size. The investigated structures were fabricated with particles of 10 nm, 20 nm, and 150 nm. The imaginary part of the refractive index κ was experimentally derived for this effective medium. It was shown that the measured reflectances and transmittances (and accordingly n and κ) no longer conform to the Kramers-Kronig relations if the cover layer thickness exceeds the range of plasmon interaction.

Besides the interaction of nanoparticles within one layering plane, the interaction of two adjacent nanoparticle planes was characterized experimentally (section 5.2.3). Structures with two particle layers were fabricated, and the absorption was studied as a function of their separation. While the adsorption of polyelectrolyte cover layers shifts the plasmon resonance to the red, the deposition of a second particle layer results in a blue shift. Both effects were explained by the coupled oscillator model. The blue shifted plasmon resonance of a two layer structure indicates that such structures can no longer be regarded as an effective medium with an effective dielectric function and an effective index of refraction. In order to describe such samples correctly, one has to account for the layered structure, i.e., for the interfaces of the particle layers.

Ultrafast Pump Probe Spectroscopy

Polyelectrolyte/nanoparticle hybrid structures with four repetition units were investigated by ultrafast pump-probe spectroscopy (chapter 6). The changes in reflectance and transmittance of an s-polarized broadband probe beam were simultaneously measured after laser excitation. A recursive formalism was derived which determines the transient effective dielectric function at every point in time for every wavelength from the measured ΔR and ΔT on the basis of the Fresnel formulas.

Prior to the ultrafast examination, the volume filling factor of the structure was determined by XRR and cross-checked by absorption spectroscopy. The particle size was determined (XRR and TEM) and possible clustering was excluded (AFM, UV-Vis Spectroscopy). Finally, the static reflectance and transmittance spectra were verified to conform to the Kramers-Kronig relations, as the cover layer thickness does not exceed the plasmon interaction range.

With these information, the transient effective dielectric function was determined in a solely experimental way. Simulations of the effective dielectric function can now be directly compared to these experimental results in order to verify the assumed electron dynamics. The ultrafast pump-probe spectroscopy method was furthermore used to study the collective vibrational motion of the nanoparticles after impulsive excitation (section 6.3). It was possible to observe a reflectance change which con-

forms with a previously reported shifting of the plasmon resonance upon a particle volume change. Transients of the effective dielectric function at 659 nm reveal that both real and imaginary parts oscillate during particle breathing and are both contributing to the changes in the optical observables R and T.

Finally, the traveling strain wave in the substrate, triggered by the expanding gold particles, was monitored by ultrafast optical spectroscopy (section 6.4). Due to the viscoelastic properties of polyelectrolytes, the elastic modulus increases considerably under impulsive strain such that the impedance mismatch at the polyelectrolyte-substrate interface is rather low and the strain wave is launched into the substrate. All time resolved pump-probe experiments were performed in a nondestructive way at a typical pump fluence of 5 mW/cm².

Future Prospects

With the fabrication of highly stratified multilayer systems, as presented in chapter 5, the requirements for ultrafast X-ray reflectivity experiments are fulfilled. In the next step a gold nanoparticle/multilayer with well-defined structural parameters will be fabricated which leads to a high-intensity first-order Bragg peak that is clearly separated from the critical angle of the total external reflection. Both the particle plane separation and the overall layer thickness can be used to control the exact position of the Bragg peaks. The thickness variations of the particle layers after impulsive excitation can be observed via a shift and intensity modulation of the Bragg peaks. The direct measurement of such quantitative parameters is a significant advantage of using X-ray pulses for probing compared to pulses in the UV-Vis spectral region.

The experimentally determined transient effective dielectric function serves as an experimental cross-check of theories modelling the electron dynamics after laser excitation. However, one of the unknown parameter that remains is the nanoparticle dielectric function. A structure will be fabricated, which conforms to the requirements of the applied Maxwell-Garnett effective medium model. This means that according to the results of chapter 5.2.2, the thickness of the bottom and cover layer must be on the order of the plasmon range in order to eliminate influences of the substrate and the ambient air. Moreover, the dielectric constant of the transparent embedding medium must be known precisely. It is then possible by inverting the effective medium expression to derive the pure nanoparticle dielectric function.

In another experiment, the transient reflectance and transmittance will be measured precisely for one breathing mode cycle in order to derive the real and imaginary parts of the effective dielectric function. The broadband changes of these components during one breathing mode cycle, analogous to the spectra shown in figure 6.9, will contribute to the understanding of the electronic system during vibrational motion.

Bibliography

- [1] D. V. Talapin, J.-S. Lee, M. V. Kovalenko and E. V. Shevchenko. “Prospects of Colloidal Nanocrystals for Electronic and Optoelectronic Applications”. *Chemical Reviews* **110**, 389 (2010).
- [2] M.-C. Daniel and D. Astruc. “Gold Nanoparticles: Assembly, Supramolecular Chemistry, Quantum-Size-Related Properties, and Applications toward Biology, Catalysis, and Nanotechnology”. *Chemical Reviews* **104**, 293 (2004).
- [3] P. T. Hammond. “Form and Function in Multilayer Assembly: New Applications at the Nanoscale”. *Advanced Materials* **16**, 1271 (2004).
- [4] X. Huang and M. A. El-Sayed. “Gold nanoparticles: Optical properties and implementations in cancer diagnosis and photothermal therapy”. *Journal of Advanced Research* **1**, 13 (2010).
- [5] B. Khlebtsov, V. Zharov, A. Melnikov, V. Tuchin and N. Khlebtsov. “Optical amplification of photothermal therapy with gold nanoparticles and nanoclusters”. *Nanotechnology* **17**, 5167 (2006).
- [6] R. Popovtzer, A. Agrawal, N. A. Kotov, A. Popovtzer, J. Balter, T. E. Carey and R. Kopelman. “Targeted Gold Nanoparticles Enable Molecular CT Imaging of Cancer”. *Nano Letters* **8**, 4593 (2008).
- [7] M. Delcea, H. Moehwald and A. G. Skirtach. “Stimuli-responsive LbL capsules and nanoshells for drug delivery”. *Advanced Drug Delivery Reviews* **63**, 730 (2011).
- [8] S. Mallidi, T. Larson, J. Aaron, K. Sokolov and S. Emelianov. “Molecular specific optoacoustic imaging with plasmonic nanoparticles”. *Optics Express* **15**, 6583 (2007).
- [9] X. Yang, E. W. Stein, S. Ashkenazi and L. V. Wang. “Nanoparticles for photoacoustic imaging”. *Wiley Interdisciplinary Reviews: Nanomedicine and Nanobiotechnology* **1**, 360 (2009).
- [10] F. Le, D. W. Brandl, Y. A. Urzhumov, H. Wang, J. Kundu, N. J. Halas, J. Aizpurua and P. Nordlander. “Metallic Nanoparticle Arrays: A Common Substrate for Both Surface-Enhanced Raman Scattering and Surface-Enhanced Infrared Absorption”. *ACS Nano* **2**, 707 (2008).

- [11] X. Huang, I. El-Sayed and M. A. El-Sayed. *Fluorescent Quenching Gold Nanoparticles: Potential Biomedical Applications*, 573–599 (John Wiley & Sons, Inc., 2010).
- [12] D. A. Genov, A. K. Sarychev, V. M. Shalaev and A. Wei. “Resonant Field Enhancements from Metal Nanoparticle Arrays”. *Nano Letters* **4**, 153 (2004).
- [13] M. Haruta. “When Gold Is Not Noble: Catalysis by Nanoparticles”. *The Chemical Record* **3**, 75 (2003).
- [14] *Catalysis and Electrocatalysis at Nanoparticle Surface* (Marcel Dekker, Inc., 2003), 1 edn..
- [15] T. Pradeep and Anshup. “Noble metal nanoparticles for water purification: A critical review”. *Thin Solid Films* **517**, 6441 (2009).
- [16] K. Lisha, Anshup and T. Pradeep. “Towards a practical solution for removing inorganic mercury from drinking water using gold nanoparticles”. *Gold Bulletin* **42**, 144 (2009).
- [17] M. Perner, S. Grésillon, J. März, G. von Plessen, J. Feldmann, J. Porstendorfer, K. J. Berg and G. Berg. “Observation of Hot-Electron Pressure in the Vibration Dynamics of Metal Nanoparticles”. *Physical Review Letters* **85**, 792 (2000).
- [18] Y. Takeda, O. A. Plaksin and N. Kishimoto. “Dispersion of nonlinear dielectric function of Au nanoparticles in silica glass”. *Optics Express* **15**, 6010 (2007).
- [19] C. Voisin, D. Christofilos, N. Del Fatti, F. Vallée, B. Prével, E. Cottancin, J. Lermé, M. Pellarin and M. Broyer. “Size-Dependent Electron-Electron Interactions in Metal Nanoparticles”. *Physical Review Letters* **85**, 2200 (2000).
- [20] G. Decher and J. B. Schlenoff (Eds.). *Multilayer Thin Films* (Wiley-VCH, 2003).
- [21] U. Kreibig and M. Vollmer. *Optical Properties of Metal Clusters*, vol. 25 of *Springer Series in Material Science* (Springer Verlag, 1995).
- [22] G. V. Hartland. “Optical Studies of Dynamics in Noble Metal Nanostructures”. *Chemical Reviews* **111**, 3858 (2011).
- [23] M. Quinten. *Optical Properties of Nanoparticle Systems* (Wiley - VCH, 2011), 1 edn..
- [24] G. Reider. *Photonik: Eine Einführung in Die Grundlagen*. Springer-Lehrbuch: Technik (Springer, 2004).
- [25] M. Guerrisi, R. Rosei and P. Winsemius. “Splitting of the interband absorption edge in Au: Temperature dependence”. *Physical Review B* **12**, 4570 (1975).

- [26] P. B. Johnson and R. W. Christy. “Optical Constants of the Noble Metals”. *Physical Review B* **6**, 4370 (1972).
- [27] H. Kuzmany. *Solid-state spectroscopy - an introduction* (Springer Verlag, Berlin, 2009), 2nd. edn..
- [28] J. C. M. Garnett. “Colours in Metal Glasses, in Metallic Films, and in Metallic Solutions. II”. *Philosophical Transactions of the Royal Society of London. Series A, Containing Papers of a Mathematical or Physical Character* **205**, 237 (1906).
- [29] U. Kreibig, A. Althoff and H. Pressmann. “Veiling of optical single particle properties in many particle systems by effective medium and clustering effects”. *Surface Science* **106**, 308 (1981).
- [30] G. A. Niklasson, C. G. Granqvist and O. Hunderi. “Effective medium models for the optical properties of inhomogeneous materials”. *Applied Optics* **20**, 26 (1981).
- [31] O. E. Piro. “Optical properties, reflectance, and transmittance of anisotropic absorbing crystal plates”. *Physical Review B* **36**, 3427 (1987).
- [32] M. V. Klein and T. E. Furtak. *Optik* (Springer, 1988).
- [33] J. Hohlfeld, S. S. Wellershoff, J. Güdde, U. Conrad, V. Jähnke and E. Matthias. “Electron and lattice dynamics following optical excitation of metals”. *Chemical Physics* **251**, 237 (2000).
- [34] S. Link and M. A. El-Sayed. “Optical Properties and ultrafast dynamics of metallic nanocrystals”. *Annual Review of Physical Chemistry* **54**, 331 (2003).
- [35] Fabrice and Vallée. “Ultrafast spectroscopy of metals”. *Comptes Rendus de l’Académie des Sciences - Series IV - Physics* **2**, 1469 (2001).
- [36] C. Voisin, N. Del Fatti, D. Christofilos and F. Vallée. “Ultrafast Electron Dynamics and Optical Nonlinearities in Metal Nanoparticles”. *The Journal of Physical Chemistry B* **105**, 2264 (2001).
- [37] G. V. Hartland. “Coherent Excitation of Vibrational Modes in Metallic Nanoparticles”. *Annual Review of Physical Chemistry* **57**, 403 (2006).
- [38] C. Sönnichsen, T. Franzl, T. Wilk, G. von Plessen, J. Feldmann, O. Wilson and P. Mulvaney. “Drastic Reduction of Plasmon Damping in Gold Nanorods”. *Physical Review Letters* **88**, 077402 (2002).
- [39] S. Link and M. A. El-Sayed. “Size and Temperature Dependence of the Plasmon Absorption of Colloidal Gold Nanoparticles”. *The Journal of Physical Chemistry B* **103**, 4212 (1999).

- [40] C. K. Sun, F. Vallée, L. H. Acioli, E. P. Ippen and J. G. Fujimoto. “Femtosecond-tunable measurement of electron thermalization in gold”. *Physical Review B* **50**, 15337 (1994).
- [41] C. Voisin, D. Christofilos, P. A. Loukakos, N. Del Fatti, F. Vallée, J. Lermé, M. Gaudry, E. Cottancin, M. Pellarin and M. Broyer. “Ultrafast electron-electron scattering and energy exchanges in noble-metal nanoparticles”. *Physical Review B* **69**, 195416 (2004).
- [42] Y. Guillet, E. Charron and B. Palpant. “Spectral dependence of the ultrafast optical response of nonspherical gold nanoparticles”. *Physical Review B* **79**, 195432 (2009).
- [43] S. Link and M. A. El-Sayed. “Shape and size dependence of radiative, non-radiative and photothermal properties of gold nanocrystals”. *International Reviews in Physical Chemistry* **19**, 409 (2000).
- [44] N. Del Fatti, C. Voisin, D. Christofilos, F. Vallée and C. Flytzanis. “Acoustic Vibration of Metal Films and Nanoparticles”. *The Journal of Physical Chemistry A* **104**, 4321 (2000).
- [45] H. Inouye, K. Tanaka, I. Tanahashi and K. Hirao. “Ultrafast dynamics of nonequilibrium electrons in a gold nanoparticle system”. *Physical Review B* **57**, 11334 (1998).
- [46] J. Y. Bigot, V. Halté, J. C. Merle and A. Daunois. “Electron dynamics in metallic nanoparticles”. *Chemical Physics* **251**, 181 (2000).
- [47] J. Y. Bigot, J. Y. Merle, O. Cregut and A. Daunois. “Electron Dynamics in Copper Metallic Nanoparticles Probed with Femtosecond Optical Pulses”. *Physical Review Letters* **75**, 4702 (1995).
- [48] J. H. Hodak, I. Martini and G. V. Hartland. “Spectroscopy and Dynamics of Nanometer-Sized Noble Metal Particles”. *The Journal of Physical Chemistry B* **102**, 6958 (1998).
- [49] G. V. Hartland. “Measurements of the material properties of metal nanoparticles by time-resolved spectroscopy”. *Physical Chemistry Chemical Physics* **6**, 5263 (2004).
- [50] N. Del Fatti, A. Arbouet and F. Vallée. “Femtosecond optical investigation of electron-lattice interactions in an ensemble and a single metal nanoparticle”. *Applied Physics B: Lasers and Optics* **84**, 175 (2006).
- [51] J. H. Hodak, A. Henglein and G. V. Hartland. “Photophysics of Nanometer Sized Metal Particles: Electron-Phonon Coupling and Coherent Excitation of Breathing Vibrational Modes”. *The Journal of Physical Chemistry B* **104**, 9954 (2000).

- [52] G. V. Hartland. “Coherent vibrational motion in metal particles: Determination of the vibrational amplitude and excitation mechanism”. *The Journal of Chemical Physics* **116**, 8048 (2002).
- [53] P. Zijlstra, A. L. Tchebotareva, J. W. M. Chon, M. Gu and M. Orrit. “Acoustic Oscillations and Elastic Moduli of Single Gold Nanorods”. *Nano Letters* **8**, 3493 (2008).
- [54] A. L. Tchebotareva, P. V. Ruijgrok, P. Zijlstra and M. Orrit. “Probing the acoustic vibrations of single metal nanoparticles by ultrashort laser pulses”. *Laser & Photonics Reviews* **4**, 581 (2010).
- [55] S. Park, M. Pelton, M. Liu, P. Guyot-Sionnest and N. F. Scherer. “Ultrafast Resonant Dynamics of Surface Plasmons in Gold Nanorods”. *The Journal of Physical Chemistry C* **111**, 116 (2007).
- [56] M. Pelton, J. E. Sader, J. Burgin, M. Liu, P. Guyot-Sionnest and D. Gosztola. “Damping of acoustic vibrations in gold nanoparticles”. *Nature Nanotechnology* **4**, 492 (2009).
- [57] A. Plech, H. Ihee, M. Cammarata, A. Siems, V. Kotaidis, F. Ciesa, J. Kim, K. H. Kim and J. H. Lee. “Structural kinetics in protein-coated gold nanoparticles probed by time-resolved x-ray scattering”. In P. Corkum, S. Silvestri, K. A. Nelson, E. Riedle, R. W. Schoenlein, F. P. Schäfer, J. P. Toennies and W. Zinth (Eds.), *Ultrafast Phenomena XVI*, vol. 92 of *Springer Series in Chemical Physics*, 134–136 (Springer Berlin Heidelberg, 2009).
- [58] R. K. Iler. “Multilayers of colloidal particles”. *Journal of Colloid and Interface Science* **21**, 569 (1966).
- [59] G. Decher, J. D. Hong and J. Schmitt. “Buildup of ultrathin multilayer films by a self-assembly process: III. Consecutively alternating adsorption of anionic and cationic polyelectrolytes on charged surfaces”. *Thin Solid Films* **210-211**, 831 (1992).
- [60] J. H. Fendler. “Self-Assembled Nanostructured Materials”. *Chemistry of Materials* **8**, 1616 (1996).
- [61] J. Cho and F. Caruso. “Investigation of the Interactions between Ligand-Stabilized Gold Nanoparticles and Polyelectrolyte Multilayer Films”. *Chemistry of Materials* **17**, 4547 (2005).
- [62] J. B. Schlenoff. “Retrospective on the Future of Polyelectrolyte Multilayers”. *Langmuir* **25**, 14007 (2009).
- [63] S. A. Sukhishvili, E. Kharlampieva and V. Izumrudov. “Where Polyelectrolyte Multilayers and Polyelectrolyte Complexes Meet”. *Macromolecules* **39**, 8873 (2006).

- [64] J. B. Schlenoff, H. Ly and M. Li. "Charge and Mass Balance in Polyelectrolyte Multilayers". *Journal of the American Chemical Society* **120**, 7626 (1998).
- [65] K. M. Lenahan, Y.-X. Wang, Y. Liu, R. O. Claus, J. R. Heflin, D. Marciu and C. Figura. "Novel Polymer Dyes for Nonlinear Optical Applications Using Ionic Self-Assembled Monolayer Technology". *Advanced Materials* **10**, 853 (1998).
- [66] J. B. Schlenoff and S. T. Dubas. "Mechanism of Polyelectrolyte Multilayer Growth: Charge Overcompensation and Distribution". *Macromolecules* **34**, 592 (2001).
- [67] J. B. Schlenoff, A. H. Rmaile and C. B. Bucur. "Hydration Contributions to Association in Polyelectrolyte Multilayers and Complexes: Visualizing Hydrophobicity". *Journal of the American Chemical Society* **130**, 13589 (2008).
- [68] L. Wang, Z. Wang, X. Zhang, J. Shen, L. Chi and H. Fuchs. "A new approach for the fabrication of an alternating multilayer film of poly(4-vinylpyridine) and poly(acrylic acid) based on hydrogen bonding". *Macromolecular Rapid Communications* **18**, 509 (1997).
- [69] Y. Fu, S. Bai, S. Cui, D. Qiu, Z. Wang and X. Zhang. "Hydrogen-Bonding-Directed Layer-by-Layer Multilayer Assembly: Reformation Yielding Microporous Films". *Macromolecules* **35**, 9451 (2002).
- [70] R. v. Klitzing. "Internal structure of polyelectrolyte multilayer assemblies". *Physical Chemistry Chemical Physics* **8**, 5012 (2006).
- [71] J. Cho, K. Char, J. D. Hong and K. B. Lee. "Fabrication of Highly Ordered Multilayer Films Using a Spin Self-Assembly Method". *Advanced Materials* **13**, 1076 (2001).
- [72] P. A. Patel, A. V. Dobrynin and P. T. Mather. "Combined Effect of Spin Speed and Ionic Strength on Polyelectrolyte Spin Assembly". *Langmuir* **23**, 12589 (2007).
- [73] G. Ladam, P. Schaad, J.-C. Voegel, P. Schaaf, G. Decher and F. Cuisinier. "In Situ Determination of the Structural Properties of Initially Deposited Polyelectrolyte Multilayers". *Langmuir* **16**, 1249 (2000).
- [74] Y. Lvov, G. Decher and H. Moehwald. "Assembly, structural characterization, and thermal behavior of layer-by-layer deposited ultrathin films of poly(vinyl sulfate) and poly(allylamine)". *Langmuir* **9**, 481 (1993).
- [75] S.-S. Lee, J.-D. Hong, C. H. Kim, K. Kim, J. P. Koo and K.-B. Lee. "Layer-by-Layer Deposited Multilayer Assemblies of Ionene-Type Polyelectrolytes Based on the Spin-Coating Method". *Macromolecules* **34**, 5358 (2001).

- [76] E. Hübsch, V. Ball, B. Senger, G. Decher, J.-C. Voegel and P. Schaaf. “Controlling the Growth Regime of Polyelectrolyte Multilayer Films: Changing from Exponential to Linear Growth by Adjusting the Composition of Polyelectrolyte Mixtures”. *Langmuir* **20**, 1980 (2004).
- [77] P. Nazaran, V. Bosio, W. Jaeger, D. F. Anghel and R. v. Klitzing. “Lateral Mobility of Polyelectrolyte Chains in Multilayers”. *The Journal of Physical Chemistry B* **111**, 8572 (2007).
- [78] T. Boudou, T. Crouzier, K. Ren, G. Blin and C. Picart. “Multiple Functionalities of Polyelectrolyte Multilayer Films: New Biomedical Applications”. *Advanced Materials* **22**, 441 (2010).
- [79] L. Krasemann and B. Tieke. “Selective Ion Transport across Self-Assembled Alternating Multilayers of Cationic and Anionic Polyelectrolytes”. *Langmuir* **16**, 287 (2000).
- [80] S. T. Dubas and J. B. Schlenoff. “Swelling and Smoothing of Polyelectrolyte Multilayers by Salt”. *Langmuir* **17**, 7725 (2001).
- [81] S. Srivastava and N. A. Kotov. “Composite Layer-by-Layer (LBL) Assembly with Inorganic Nanoparticles and Nanowires”. *Accounts of Chemical Research* **41**, 1831 (2008).
- [82] S. Kinge, M. Crego-Calama and D. Reinhoudt. “Self-assembling nanoparticles at surfaces and interfaces.” *ChemPhysChem* **9**, 20 (2008).
- [83] C. Jiang, S. Markutsya and V. V. Tsukruk. “Collective and Individual Plasmon Resonances in Nanoparticle Films Obtained by Spin-Assisted Layer-by-Layer Assembly”. *Langmuir* **20**, 882 (2004).
- [84] D. Grigoriev, D. Gorin, G. B. Sukhorukov, A. Yashchenok, E. Maltseva and H. Möhwald. “Polyelectrolyte/magnetite Nanoparticle Multilayers: Preparation and Structure Characterization”. *Langmuir* **23**, 12388 (2007).
- [85] R. S. Krishnan, M. E. Mackay, P. M. Duxbury, A. Pastor, C. J. Hawker, B. Van Horn, S. Asokan and M. S. Wong. “Self-Assembled Multilayers of Nanocomponents”. *Nano Letters* **7**, 484 (2007).
- [86] B. Yuan, L.-L. Xing, Y.-D. Zhang, Y. Lu, Z.-H. Mai and M. Li. “Self-Assembly of Highly Oriented Lamellar Nanoparticle-Phospholipid Nanocomposites on Solid Surfaces”. *Journal of the American Chemical Society* **129**, 11332 (2007).
- [87] D. Lee, M. F. Rubner and R. E. Cohen. “All-Nanoparticle Thin-Film Coatings”. *Nano Letters* **6**, 2305 (2006).

- [88] H.-C. Lee, T.-W. Lee, T.-H. Kim and O. O. Park. "Fabrication and characterization of polymer/nanoclay hybrid ultrathin multilayer film by spin self-assembly method". *Thin Solid Films* **458**, 9 (2004).
- [89] J. Schmitt, G. Decher, W. J. Dressick, S. L. Brandow, R. E. Geer, R. Shashidhar and J. M. Calvert. "Metal nanoparticle/polymer superlattice films: Fabrication and control of layer structure". *Advanced Materials* **9**, 61 (1997).
- [90] C. A. Constantine, K. M. Gattás-Asfura, S. V. Mello, G. Crespo, V. Rastogi, T.-C. Cheng, J. J. DeFrank and R. M. Leblanc. "Layer-by-Layer Biosensor Assembly Incorporating Functionalized Quantum Dots". *Langmuir* **19**, 9863 (2003).
- [91] T. Cassier, K. Lowack and G. Decher. "Layer-by-layer assembled protein/polymer hybrid films: nanoconstruction via specific recognition". *Supramolecular Science* **5**, 309 (1998).
- [92] Y. Lvov, G. Decher and G. Sukhorukov. "Assembly of thin films by means of successive deposition of alternate layers of DNA and poly(allylamine)". *Macromolecules* **26**, 5396 (1993).
- [93] Y. Lvov, H. Haas, G. Decher, H. Moehwald, A. Mikhailov, B. Mtchedlishvily, E. Morgunova and B. Vainshtein. "Successive Deposition of Alternate Layers of Polyelectrolytes and a Charged Virus". *Langmuir* **10**, 4232 (1994).
- [94] D. M. Dotzauer, J. Dai, L. Sun and M. L. Bruening. "Catalytic Membranes Prepared Using Layer-by-Layer Adsorption of Polyelectrolyte/Metal Nanoparticle Films in Porous Supports". *Nano Letters* **6**, 2268 (2006).
- [95] M. M. de Villiers, D. P. Otto, S. J. Strydom and Y. M. Lvov. "Introduction to nanocoatings produced by layer-by-layer (LbL) self-assembly". *Advanced Drug Delivery Reviews* **63**, 701 (2011).
- [96] K. Ariga, Y. M. Lvov, K. Kawakami, Q. Ji and J. P. Hill. "Layer-by-layer self-assembled shells for drug delivery". *Advanced Drug Delivery Reviews* **63**, 762 (2011).
- [97] C. Hanisch, A. Kulkarni, V. Zaporozhchenko and F. Faupel. "Polymer-metal nanocomposites with 2-dimensional Au nanoparticle arrays for sensoric applications". *Journal of Physics: Conference Series* **100**, 052043 (2008).
- [98] A. Yu, Z. Liang, J. Cho and F. Caruso. "Nanostructured Electrochemical Sensor Based on Dense Gold Nanoparticle Films". *Nano Letters* **3**, 1203 (2003).
- [99] F. Caruso, E. Rodda, D. N. Furlong, K. Niikura and Y. Okahata. "Quartz Crystal Microbalance Study of DNA Immobilization and Hybridization for Nucleic Acid Sensor Development". *Analytical Chemistry* **69**, 2043 (1997).

- [100] M. Helgesen, R. Sondergaard and F. C. Krebs. “Advanced materials and processes for polymer solar cell devices”. *Journal of Materials Chemistry* **20**, 36 (2010).
- [101] T. Kietzke, D. Neher, K. Landfester, R. Montenegro, R. Guntner and U. Scherf. “Novel approaches to polymer blends based on polymer”. *Nature Materials* **2**, 408 (2003).
- [102] S. W. Tong, C. F. Zhang, C. Y. Jiang, G. Liu, Q. D. Ling, E. T. Kang, D. S. H. Chan and C. Zhu. “Improvement in the hole collection of polymer solar cells by utilizing gold nanoparticle buffer layer”. *Chemical Physics Letters* **453**, 73 (2008).
- [103] Z. Liang, K. L. Dzienis, J. Xu and Q. Wang. “Covalent Layer-by-Layer Assembly of Conjugated Polymers and CdSe Nanoparticles: Multilayer Structure and Photovoltaic Properties”. *Advanced Functional Materials* **16**, 542 (2006).
- [104] J.-A. He, R. Mosurkal, L. A. Samuelson, L. Li and J. Kumar. “Dye-sensitized Solar Cell Fabricated by Electrostatic Layer-by-Layer Assembly of Amphoteric TiO₂ Nanoparticles”. *Langmuir* **19**, 2169 (2003).
- [105] T. C. Wang, R. E. Cohen and M. F. Rubner. “Metallo-dielectric Photonic Structures Based on Polyelectrolyte Multilayers”. *Advanced Materials* **14**, 1534 (2002).
- [106] R. Dekker, D. J. W. Klunder, A. Borreman, M. B. J. Diemeer, K. Wörhoff, A. Driessen, J. W. Stouwdam and F. C. J. M. van Veggel. “Stimulated emission and optical gain in LaF₃:Nd nanoparticle-doped polymer-based waveguides”. *Applied Physics Letters* **85**, 6104 (2004).
- [107] Z. Wu, J. Walish, A. Nolte, L. Zhai, R. E. Cohen and M. F. Rubner. “Deformable Antireflection Coatings from Polymer and Nanoparticle Multilayers”. *Advanced Materials* **18**, 2699 (2006).
- [108] M. T. Crisp and N. A. Kotov. “Preparation of Nanoparticle Coatings on Surfaces of Complex Geometry”. *Nano Letters* **3**, 173 (2003).
- [109] H. Hattori. “Anti-Reflection Surface with Particle Coating Deposited by Electrostatic Attraction”. *Advanced Materials* **13**, 51 (2001).
- [110] P. Bertrand, A. Jonas, A. Laschewsky and R. Legras. “Ultrathin polymer coatings by complexation of polyelectrolytes at interfaces: suitable materials, structure and properties”. *Macromolecular Rapid Communications* **21**, 319 (2000).
- [111] S. Mitzscherling. “Herstellung und Charakterisierung von Nanoschichtsystemen aus Polyelektrolyten und Goldpartikeln”. Master’s thesis, University of Potsdam (2010).

- [112] C. J. Lefaux, J. A. Zimberlin, A. V. Dobrynin and P. T. Mather. "Polyelectrolyte spin assembly: Influence of ionic strength on the growth of multilayered thin films". *Journal of Polymer Science Part B: Polymer Physics* **42**, 3654 (2004).
- [113] M. F. Bédard, B. G. D. Geest, A. G. Skirtach, H. Moehwald and G. B. Sukhorukov. "Polymeric microcapsules with light responsive properties for encapsulation and release". *Advances in Colloid and Interface Science* **158**, 2 (2010).
- [114] S. T. Dubas and J. B. Schlenoff. "Factors Controlling the Growth of Polyelectrolyte Multilayers". *Macromolecules* **32**, 8153 (1999).
- [115] J. A. Giordmaine and R. C. Miller. "Tunable Coherent Parametric Oscillation in LiNbO₃ at Optical Frequencies". *Physical Review Letters* **14**, 973 (1965).
- [116] E. Riedle, M. Beutter, S. Lochbrunner, J. Piel, S. Schenkl, S. Spörlein and W. Zinth. "Generation of 10 to 50 fs pulses tunable through all of the visible and the NIR". *Applied Physics B: Lasers and Optics* **71**, 457 (2000).
- [117] D. Brida, C. Manzoni, G. Cirimi, M. Marangoni, S. Bonora, P. Villoresi, S. D. Silvestri and G. Cerullo. "Few-optical-cycle pulses tunable from the visible to the mid-infrared by optical parametric amplifiers". *Journal of Optics* **12**, 013001 (2010).
- [118] A. Brodeur and S. L. Chin. "Ultrafast white-light continuum generation and self-focusing in transparent condensed media". *J. Opt. Soc. Am. B* **16**, 637 (1999).
- [119] R. Trebino, K. W. DeLong, D. N. Fittinghoff, J. N. Sweetser, M. A. Krumbügel, B. A. Richman and D. J. Kane. "Measuring ultrashort laser pulses in the time-frequency domain using frequency-resolved optical gating". *Review of Scientific Instruments* **68**, 3277 (1997).
- [120] D. J. Kane and R. Trebino. "Single-shot measurement of the intensity and phase of an arbitrary ultrashort pulse by using frequency-resolved optical gating". *Optics Letters* **18**, 823 (1993).
- [121] F. E. Kruis, H. Fissan and A. Peled. "Synthesis of nanoparticles in the gas phase for electronic, optical and magnetic applications - a review". *Journal of Aerosol Science* **29**, 511 (1998).
- [122] K. A. Willets and R. P. Van Duyne. "Localized Surface Plasmon Resonance Spectroscopy and Sensing". *Annual Review of Physical Chemistry* **58**, 267 (2007).
- [123] T.-H. Kim and B.-H. Sohn. "Photocatalytic thin films containing TiO₂ nanoparticles by the layer-by-layer self-assembling method". *Applied Surface Science* **201**, 109 (2002).

- [124] F. Shi, Q. Zhang, Y. Ma, Y. He and Y. Deng. “From CO Oxidation to CO₂ Activation: An Unexpected Catalytic Activity of Polymer-Supported Nanogold”. *Journal of the American Chemical Society* **127**, 4182 (2005).
- [125] H. Wohltjen and A. W. Snow. “Colloidal Metal-Insulator-Metal Ensemble Chemiresistor Sensor”. *Analytical Chemistry* **70**, 2856 (1998).
- [126] A. J. Nolte, M. F. Rubner and R. E. Cohen. “Creating Effective Refractive Index Gradients within Polyelectrolyte Multilayer Films: Molecularly Assembled Rugate Filters”. *Langmuir* **20**, 3304 (2004).
- [127] G. Decher. “Fuzzy Nanoassemblies: Toward Layered Polymeric Multicomposites”. *Science* **277**, 1232 (1997).
- [128] R. Ruppin. “Optical absorption of copper colloids in photochromic glasses”. *Journal of Applied Physics* **59**, 1355 (1986).
- [129] A. E. Neeves and M. H. Birnboim. “Composite structures for the enhancement of nonlinear-optical susceptibility”. *J. Opt. Soc. Am. B* **6**, 787 (1989).
- [130] M. Duval Malinsky, K. L. Kelly, G. C. Schatz and R. P. Van Duyne. “Nanosphere Lithography: Effect of Substrate on the Localized Surface Plasmon Resonance Spectrum of Silver Nanoparticles”. *The Journal of Physical Chemistry B* **105**, 2343 (2001).
- [131] G. Xu, Y. Chen, M. Tazawa and P. Jin. “Influence of dielectric properties of a substrate upon plasmon resonance spectrum of supported Ag nanoparticles”. *Applied Physics Letters* **88**, 043114 (2006).
- [132] M. Kiel, S. Mitzscherling, W. Leitenberger, S. Santer, B. Tiersch, T. K. Sievers, H. Möhwald and M. Bargheer. “Structural Characterization of a Spin-Assisted Colloid-Polyelectrolyte Assembly: Stratified Multilayer Thin Films”. *Langmuir* **26**, 18499 (2010).
- [133] L. G. Parratt. “Surface Studies of Solids by Total Reflection of X-Rays”. *Physical Review* **95**, 359 (1954).
- [134] J. Als-Nielsen and D. McMorrow. *Elements of Modern X-Ray Physics* (John Wiley & Sons, Ltd., 2001).
- [135] M. Kiel, M. Klötzer, S. Mitzscherling and M. Bargheer. “Measuring the Range of Plasmonic Interaction”. *Langmuir* **28**, 4800 (2012).
- [136] M. Kasha, H. R. Rawls and M. Ashraf El-Bayoumi. “The exciton model in molecular spectroscopy”. *Pure Appl. Chem.* **11**, 371 (1965).
- [137] P. G. Etchegoin, E. C. L. Ru and M. Meyer. “An analytic model for the optical properties of gold”. *The Journal of Chemical Physics* **125**, 164705 (2006).

- [138] J. N. Anker, W. P. Hall, O. Lyandres, N. C. Shah, J. Zhao and R. P. Van Duyne. “Biosensing with plasmonic nanosensors”. *Nature Materials* **7**, 442 (2008).
- [139] P. Jain, X. Huang, I. El-Sayed and M. El-Sayed. “Review of Some Interesting Surface Plasmon Resonance-enhanced Properties of Noble Metal Nanoparticles and Their Applications to Biosystems”. *Plasmonics* **2**, 107 (2007).
- [140] T. A. Taton, C. A. Mirkin and R. L. Letsinger. “Scanometric DNA Array Detection with Nanoparticle Probes”. *Science* **289**, 1757 (2000).
- [141] T. Vossmeier, B. Guse, I. Besnard, R. E. Bauer, K. Müllen and A. Yasuda. “Gold Nanoparticle/Polyphenylene Dendrimer Composite Films: Preparation and Vapor-Sensing Properties”. *Advanced Materials* **14**, 238 (2002).
- [142] S. Mittler. “Gold Nanoparticles on Waveguides For and Toward Sensing Application”. In O. S. Wolfbeis, M. Zourob and A. Lakhtakia (Eds.), *Optical Guided-wave Chemical and Biosensors I*, vol. 7 of *Springer Series on Chemical Sensors and Biosensors*, 209–229 (Springer Berlin Heidelberg, 2009).
- [143] K.-Y. Jung, F. L. Teixeira and R. M. Reano. “Au/SiO₂ Nanoring Plasmon Waveguides at Optical Communication Band”. *Lightwave Technology, Journal of* **25**, 2757 (2007).
- [144] H. Nishiyama, Y. Hirata, I. Miyamoto and J. Nishii. “Formation of periodic structures by the space-selective precipitation of Ge nanoparticles in channel waveguides”. *Applied Surface Science* **253**, 6550 (2007).
- [145] N. Del Fatti, C. Voisin, M. Achermann, S. Tzortzakis, D. Christofilos and F. Vallée. “Nonequilibrium electron dynamics in noble metals”. *Physical Review B* **61**, 16956 (2000).
- [146] Y. Takeda, H. Momida, M. Ohnuma, T. Ohno and N. Kishimoto. “Wavelength dispersion of nonlinear dielectric function of Cu nanoparticle materials”. *Optics Express* **16**, 7471 (2008).
- [147] M. Kiel, H. Möhwald and M. Bargheer. “Broadband measurements of the transient optical complex dielectric function of a nanoparticle/polymer composite upon ultrafast excitation”. *Physical Review B* **84**, 165121 (2011).
- [148] S. I. Anisimov, B. L. Kapeliovich and T. L. Perel’man. “Electron emission from metal surfaces exposed to ultrashort laser pulses”. *Journal of Experimental and Theoretical Physics* **39**, 375 (1974).
- [149] G. V. Hartland, M. Hu and J. E. Sader. “Softening of the Symmetric Breathing Mode in Gold Particles by Laser-Induced Heating”. *The Journal of Physical Chemistry B* **107**, 7472 (2003).

-
- [150] A. Neubrand and P. Hess. “Laser generation and detection of surface acoustic waves: Elastic properties of surface layers”. *Journal of Applied Physics* **71**, 227 (1992).
- [151] C. Voisin, N. D. Fatti, D. Christofilos and F. Vallée. “Time-resolved investigation of the vibrational dynamics of metal nanoparticles”. *Applied Surface Science* **164**, 131 (2000).
- [152] W. Huang, W. Qian and M. A. El-Sayed. “The Optically Detected Coherent Lattice Oscillations in Silver and Gold Monolayer Periodic Nanoprism Arrays: The Effect of Interparticle Coupling”. *The Journal of Physical Chemistry B* **109**, 18881 (2005).
- [153] P. V. Ruijgrok, P. Zijlstra, A. L. Tchebotareva and M. Orrit. “Damping of Acoustic Vibrations of Single Gold Nanoparticles Optically Trapped in Water”. *Nano Letters* **12**, 1063 (2012).
- [154] R. A. L. Jones. *Soft Condensed Matter*. Oxford Master Series in Condensed Matter Physics (Oxford University Press, 2002).
- [155] C. Thomsen, H. T. Grahn, H. J. Maris and J. Tauc. “Surface generation and detection of phonons by picosecond light pulses”. *Physical Review B* **34**, 4129 (1986).
- [156] M. Herzog, D. Schick, P. Gaal, R. Shayduk, C. von Korff Schmising and M. Bargheer. “Analysis of ultrafast X-ray diffraction data in a linear-chain model of the lattice dynamics”. *Applied Physics A* **106**, 489 (2012).

List of Figures

2.1	Calculations of the imaginary (i) and real (ii) parts of the dielectric function according to the harmonic oscillator model.	6
2.2	Drude contribution to the dielectric function in bulk gold. (i) shows the imaginary and (ii) the real part of the dielectric function.	7
2.3	(a) and (b) present the results of band structure calculations of bulk gold by M. Guerrisi et al. at two different points of the brillouin zone (Modified after reference [25]). (c) The solid lines depict the theoretical dielectric function of gold according to the band structure calculations of M. Guerrisi et al. The symbols correspond to experimental values measured by P. B. Johnson and R. W. Christy in 1972.[26]	8
2.4	(a) Simplified presentation of the band structure in gold. The flat d-bands overlap with the sp-conduction band. The vectors indicate interband (left) and intraband (right) transitions. (b) Cartoon of the nanoparticle electronic polarization induced by an electromagnetic wave.	9
2.5	Example of the imaginary (i) and real (ii) parts of the effective dielectric function of an arbitrary polyelectrolyte/nanoparticle compound structure.	11
2.6	(a) Beam propagation in a thin layer sample. (b) The matrix formalism applied to a thin layer sample on a substrate. The system matrix S describes the complete structure and allows for calculating the according reflectance and transmittance (see equations 2.18 and 2.19).	12
2.7	(a) Electronic occupation at the Fermi-level before excitation, (b) non-thermalized electron distribution right after excitation, and (c) ~ 500 fs after thermalization to a hot Fermi distribution.	16
3.1	(a) In the layer-by-layer method, the polyelectrolyte layers are successively deposited on the topmost film. (b) and (c) illustrate the two complex formation processes. During intrinsic charge compensation, only the charged polyelectrolyte segments take part in complex building, while in the extrinsic one, Na^+ or Cl^- counterions are involved. (Modified after [64])	20
3.2	Chemical structures of the used polyelectrolytes. (Modified after [111])	23

3.3	Schematic presentation of the preparation procedure according to the dip-coating technique. After the adsorption of the polyelectrolytes (red and blue), two washing steps are carried out (grey), followed by a drying step with a nitrogen air blowing unit. The specified durations are waiting times after immersion of the substrate into the respective material or times which describe the duration of the nitrogen air blow.	25
3.4	Schematic presentation of the preparation procedure for polyelectrolyte multilayers according to the spin-coating LbL technique. The specified durations are waiting times after dispersion of the respective material until the next step is executed. The spin-coater is constantly running throughout this process. (Modified after [111])	26
3.5	Schematic presentation of the detection setup in the UV-Vis-NIR spectrometer using an integrating sphere (Ulbricht sphere). This sphere detects both the specular and the diffuse scattering components. Adjustments are possible in which only the diffuse scattering contributions are measured (not shown here).	28
3.6	(a) Experimental setup at Bessy II for XRR measurements. (b) Illustration of the θ - 2θ geometry. This picture also visualizes the effect that with higher θ -angles, a larger cross-sectional area of the wide X-ray beam is filled out.	29
3.7	(a) Setup for angle-dependent reflectance and transmittance measurements. The polarizer assures the HeNe light to be purely s- or p-polarized. (b) Typically both reflections from the sample layer interfaces are detected, but the transmitted and reflected beams from the rear substrate interface are blocked.	31
4.1	(a) Measured spectrum of the Spitfire Pro laser system (blue symbols). The red line is a Gaussian fit to the data. (b) The measured (blue symbols) and fitted (red line) autocorrelation signals define the laser pulse length to measure 165 fs (FWHM).	34
4.2	Photonic description of the difference frequency mixing process.	35
4.3	Setup of the noncollinear optical parametric amplifier, called NOPA, (dashed lined box) and a two-prism compressor. Used abbreviations: A = aperture, BS = beamsplitter, BBO = β -barium borite crystal, M = mirror, NDF = neutral density filter, L = lens, S = sapphire plate, FM = focusing mirror, and PR = prism.	36
4.4	(a) The measured and fitted NOPA beam spectrum reveals a spectral bandwidth of ~ 15 nm. (b) From the according autocorrelation signal, the pulse length can be determined to measure ~ 55 fs (FWHM).	37
4.5	(a) Setup for wlc generation. Used abbreviations: NDF = neutral density filter, A = aperture, L = lens, and S = sapphire plate. (b) The measured spectrum. A filter was used for the attenuation of wavelengths above 750 nm.	38

- 4.6 (a) Setup for “frequency-resolved optical gating” (FROG). Used abbreviations: WP = waveplate, P = polarizer, L = lens, and SP = sapphire plate. (b) Measured FROG signal. 39
- 4.7 Pump-probe spectroscopy setup. In this setup a two-channel spectrometer simultaneously detects the reflectance and transmittance. Used abbreviations: L = lens, Ch = chopper, P = polarizer, G = goniometer. 40
- 5.1 X-ray reflectivity results of a dip-coated sample on glass (a) and of a spin-coated sample on mica (b). Both structures exhibit the layering sequence $[(\text{PSS}/\text{PAH})_n + (\text{Au-NP}/\text{PAH})_4]$, where n measures 10 for the dip-coated structure and 8 for the spin coated one. 45
- 5.2 Parabolic electronic density distribution of a spherical nanoparticle . 46
- 5.3 Electron density distributions along the growth direction z . The red lines represent the distributions that were assumed to simulate the reflectances according to the measurements shown in figure 5.4. The blue lines represent the ideal electronic density distribution of perfectly aligned nanoparticle layers which inherently exhibit a parabolic profile. 47
- 5.4 X-ray reflectivity data (red circles) and simulations (blue lines). The black dashed line represents the ideal X-ray reflectivity that belongs to the ideal electron distribution in figure 5.3. 47
- 5.5 (a) AFM picture of a gold-particle layer on 8 DL PAH/PSS and (b) peak-to-valley modulation of two spheres measured along the white bar in (a). The cartoon in (c) visualizes the lateral particle distribution which corresponds to the volume filling factor of $f = 0.034$ as measured for the dip-coated sample. 50
- 5.6 (a) AFM surface roughness results (RMS values) as a function of the number of double layers ($\#$ DL) which are deposited on the surface of a gold-nanoparticle layer. (b) TEM picture of a dip-coated sample on glass with 8 repetition units. This picture nicely visualizes the smoothing of layers with deposition of polyelectrolytes (see box). . . . 51
- 5.7 Measured reflectance (a) and transmittance (b) spectra of structures with 10 nm particles. (c) shows diffuse scattering contributions of two samples and (d) is the absorption determined by $A = 1 - R_{sd} - T_{sd}$. The blue- and magenta-colored lines clearly show a slight red shift and higher absorption intensities in the red spectral region. Both effects indicate a clustering of particles. 52
- 5.8 (a) Integral absorption of the plasmon resonance as a function of the adsorption time. (b) Cartoon of the energy splitting process of two interacting nanoparticles.[136] 53

- 5.9 (a) and (b) Transmission and (c) and (d) reflection spectra as functions of the cover layer thickness $D_{DL} = 2.5 \cdot DL$ on a 10-nm gold-nanoparticle layer. The spectra were measured at normal incidence for 10-nm gold particles on 8 DL PSS/PAH with an in-plane particle density of $1900 \mu\text{m}^{-2}$. (e) and (f) present the corresponding absorption spectra. 55
- 5.10 Peak shift (a) and integral absorption change (b) as functions of the cover layer thickness D_n on a single nanoparticle layer with 10-nm (black), 20-nm (red), and 150-nm (blue) particles. The symbols represent measured data, while the solid lines are double-exponential fits. 56
- 5.11 Real (black) and imaginary (red) parts of the dielectric function of bulk gold from Johnson and Christy[26]. For half-embedded particles the resonance condition is fulfilled at 525 nm (magenta circles). The red-shifted resonance (blue circles) belongs to the situation where the particles are fully covered with PAH/PSS (538 nm). 57
- 5.12 (a) presents the imaginary part κ and (b) the real part n of the refractive index of the effective medium plotted as functions of the cover layer thickness D_n . (a) clearly shows an increase in the imaginary part for a cover layer thickness up to 1.5 DL. Further deposition leads to a significant decrease. While the red shift of the imaginary part saturates after 10 nm, the real part (b) keeps changing its spectral position throughout the deposition process. 58
- 5.13 (a) presents the absorption spectra of a compound structure with two particle layers. The spectra were measured at intermediate states during the deposition process. (b) shows the shift in the plasmon resonance as a function of the separation of the two particle layers. 59
- 5.14 Angular-dependent transmittances and reflectances of a multilayer structure measured at 543 nm. The symbols represent experimental data, while the solid lines are simulations. Different dielectric constants were assumed for the simulations in (a) (s-polarization) and (b) (p-polarization). The magenta line in (b) was calculated with the same ϵ_{eff} as used in (a). 61
- 5.15 Illustration of the matrix formalism. Expressions for the system matrix S in (a) reflection and (b) transmission geometry. 62
- 5.16 (a) Measured specular reflectance and transmittance and the real and imaginary parts of the according dielectric function at $\alpha = 0^\circ$. (b) Measured and simulated absorption spectra. The experimental absorption was determined by $A = 1 - T - R$, where T and R must comprise the diffuse and specular components. 63

6.1	(b) and (c) show the simultaneously measured broadband reflectance $\Delta R/R_0$ and transmittance $\Delta T/T_0$, respectively. Transients of the reflectance (a) and transmittance (d) at three distinct energies. (e) and (f) show spectral projections at three distinct times after excitation.	68
6.2	(a) Absorption ($\Delta A/A_0$) calculated from measured changes in the reflectance and transmittance. (b) Spectral projections at three distinct times after excitation. (c) Transient absorption for three energies.	69
6.3	Measured absolute spectra of the reflectance (a) and (b), transmittance (c) and (d), and absorbance (e) and (f). The left side shows spectra during the thermalization process to a hot Fermi distribution ($0 < t < 600$ fs after excitation), and the right side shows spectra during the relaxation process ($0 < t < 9.4$ ps after excitation).	70
6.4	Illustrations of the three characteristic processes in pump-probe measurements. (1) Excitation and thermalization of the electrons to a hot Fermi distribution. (2) Transfer of electronic energy to the lattice via electron-phonon coupling. (3) Lattice relaxation (typically several nanoseconds).	71
6.5	(a) Sketch of the electron and lattice temperatures during the electron-phonon coupling process. (b) Measurement of transient electronic signals for two different pump fluences.	72
6.6	Calculated change in the reflectance (a) and transmittance (b) as a function of the assumed values of the real and imaginary parts of the effective dielectric function. These matrices apply to a probe light wavelength of 543 nm.	74
6.7	Transient real (a)–(c) and imaginary (d)–(f) parts of the dielectric function determined from simultaneous measurements of the reflectance and transmittance. Again, three temporal and spectral cuts from the 2D contour plots are presented.	75
6.8	(a) Measured trajectories of the complex dielectric function as a function of time. (b) Spectral dependence of coefficients that correlate the measured quantities ΔR and ΔT to $\Delta\epsilon_r^{eff}$ and $\Delta\epsilon_i^{eff}$.	76
6.9	Absolute real (a) and (b) and imaginary (c) and (d) parts of the dielectric function. The left side shows spectra during the thermalization process shortly after excitation. The spectra on the right illustrate the relaxation back to the steady-state dielectric function (black line).	77
6.10	(a) 2D color-coded transient reflectance ($\Delta R/R_0$) for probe energies ranging from 1.78 eV to 2.21 eV for three oscillation periods. (b) Transient reflectance for four different energies. The investigated sample comprises four gold-nanoparticle layers.	78
6.11	Simultaneously measured transient reflectance (a) and transient transmittance (b) of the vibrational mode of 20-nm gold nanoparticles in a polyelectrolyte matrix. The investigated sample comprises four nanoparticle layers.	79

-
- 6.12 Absolute reflectance spectra during vibrational motion of 10-nm gold nanoparticles. (a) Spectra measured at 7.1 ps and 7.6 ps after excitation, visualizing the shift to the red. (b) Blue-shifted spectra recorded one half period later. The dashed line in both panels represents the static reflectance spectrum. 80
- 6.13 (a) Transient absorption of 20 nm gold nanoparticles embedded in polyelectrolytes. (b) Real and imaginary part of the dielectric function of 10 nm gold particles measured at 659 nm. 81
- 6.14 Measured transient reflectance $\Delta R/R_0$ showing oscillations with probe-energy-dependent periods. The investigated sample exhibits four stratified nanoparticle layers and particles with a diameter of 10 nm. 83
- 6.15 (a) Illustration of a dipolar strain pulse. (b) The detected reflectance results from an interference of the sample layer reflectance and the travelling strain pulse in the substrate. 84
- 6.16 (a) Fourier analysis of the detected oscillations in the reflectance transients. (b) Oscillation frequency plotted versus the probe wavelength. The slope is a measure of the sound velocity in the glass substrate. . 85

Veröffentlichungen

Veröffentlichungen im Zusammenhang mit dieser Arbeit:

- M. Kiel, M. Klötzer, S. Mitzscherling, M. Bargheer. Measuring the Range of Plasmonic Interaction. *Langmuir* **28**, 4800 (2012).
- M. Kiel, H. Möhwald, M. Bargheer. Broadband measurements of the transient optical complex dielectric function of a nanoparticle/polymer composite upon ultrafast excitation. *Physical Review B* **84**, 165121 (2011).
- M. Kiel, S. Mitzscherling, W. Leitenberger, S. Santer, B. Tiersch, T. K. Sievers, H. Möhwald, M. Bargheer. Structural Characterization of a Spin-Assisted Colloid-Polyelectrolyte Assembly: Stratified Multilayer Thin Films. *Langmuir* **26**, 18499 (2010).

Weitere Veröffentlichungen:

- D. Schick, C. von Korff Schmising, A. Bojahr, M. Kiel, P. Gaal, M. Bargheer. Time-resolved x-ray scattering. *Ultrafast Phenomena in Semiconductors and Nanostructure Materials XV* **7937**, 793715 (2011).
- M. Braun, C. von Korff Schmising, M. Kiel, N. Zhavoronkov, J. Dreyer, M. Bargheer, T. Elsaesser, C. Root, T. E. Schrader, P. Gilch, W. Zinth, M. Woerner. Ultrafast Changes of Molecular Crystal Structure Induced by Dipole Solvation. *Physical Review Letters* **98**, 248301 (2007).
- C. von Korff Schmising, M. Bargheer, M. Kiel, N. Zhavoronkov, M. Woerner, T. Elsaesser, I. Vrejoiu, D. Hesse, M. Alexe. Accurate time delay determination for femtosecond X-ray diffraction experiments. *Appl. Phys. B* **88**, 1 (2007).
- C. von Korff Schmising, M. Bargheer, M. Kiel, N. Zhavoronkov, M. Woerner, T. Elsaesser, I. Vrejoiu, D. Hesse, M. Alexe. Coupled Ultrafast Lattice and Polarization Dynamics in Ferroelectric Nanolayers. *Physical Review Letters* **98**, 257601 (2007).
- C. von Korff Schmising, M. Bargheer, M. Kiel, N. Zhavoronkov, M. Woerner, T. Elsaesser, I. Vrejoiu, D. Hesse, M. Alexe. Ultrafast structure and po-

larization dynamics in nanolayered perovskites studied by femtosecond X-ray diffraction. *Journal of Physics: Conference Series* **92**, 012177 (4pp) (2007).

- C. von Korff Schmising, M. Bargheer, M. Kiel, N. Zhavoronkov, M. Woerner, T. Elsaesser, I. Vrejoiu, D. Hesse, M. Alexe. Strain propagation in nanolayered perovskites probed by ultrafast x-ray diffraction. *Physical Review B (Condensed Matter and Materials Physics)* **73**, 212202 (2006).

Danksagung

Mein besonderer Dank gilt Professor Matias Bargheer, der es mir ermöglichte zu dem interessanten Thema Ultraschnelle Spektroskopie in seiner Arbeitsgruppe, der UDKM, zu promovieren. In zahllosen Diskussionen über meine Ergebnisse und über unsere Publikationen habe ich immer von seiner Begeisterungsfähigkeit profitiert und daraus einen Ansporn gefunden.

Ich danke den Gutachtern, die sich kurzfristig bereit erklärt haben, diese Arbeit zu begutachten.

Darüber hinaus möchte ich die langjährige Unterstützung, die ich von Prof. Möhwald erfahren habe, hervorheben. Der reiche Erfahrungsschatz seiner Arbeitsgruppe kam mir bei der Herstellung und Untersuchung von Polyelektrolyt-Multilayerschichten sehr zugute. Dabei möchte ich mich vor allem bei Dr. Torsten Sievers für die informativen Diskussionen und den zahlreichen praktischen Anregungen bedanken.

Herzlich bedanken möchte ich mich außerdem bei Wolfram Leitenberger und Peter Gaál, die maßgeblich die Röntgenreflektometrie-Messungen am BESSY II durchgeführt haben.

Ich danke Madlen Klötzer und Steffen Mitzscherling, die im Rahmen ihrer Diplomarbeiten wichtige Aufgaben für die Probenherstellung und Charakterisierung gelöst haben.

Die Arbeitsgruppe von Professor Neher hat mir stets ermöglicht, die Spektrometer und das AFM für die Charakterisierung meiner Proben zu nutzen und stand mir dabei mit Rat und Tat zur Seite. Vielen Dank für die kooperative und freundschaftliche Zusammenarbeit.

In der Arbeitsgruppe von Professorin Santer konnten weitere AFM-Messungen durchgeführt werden, wofür ich mich ebenfalls herzlich bedanke.

Weiterer Dank gilt Dr. Brigitte Tiersch, die meine Proben aufwändig präpariert und anschließend in ihrem TEM untersucht hat.

Zu guter Letzt möchte ich mich bei den Mitgliedern der UDKM-Gruppe für das freundschaftliche Arbeitsklima und die ständige Hilfsbereitschaft bedanken: Marc Herzog, Steffen Mitzscherling, André Bojahr, Peter Gaál, Yevgen Goldshteyn, Wolfram Leitenberger, Lena Merten, Hengameh Navirian, Daniel Schick und Roman Shayduk. Vielen Dank.

Selbständigkeitserklärung

Hiermit erkläre ich, dass ich die vorliegende Arbeit selbständig und nur unter Verwendung der angegebenen Literatur und Hilfsmittel angefertigt habe. Ich erkläre weiterhin, dass diese Arbeit keiner anderen Fakultät vorgelegt und von keiner anderen Fakultät abgelehnt wurde.

Berlin, den 02.05.2012

Mareike Kiel